Improving the Environmental Stability of Methylammonium-Based Perovskite Solar Cells

by

Noor Titan Putri Hartono

B.S. Mechanical Engineering, Massachusetts Institute of Technology (2016)
S.M. Mechanical Engineering, Massachusetts Institute of Technology (2018)

Submitted to the Department of Mechanical Engineering
in partial fulfillment of the requirements for the degree of

Doctor of Philosophy in Mechanical Engineering

at the

MASSACHUSETTS INSTITUTE OF TECHNOLOGY

June 2021

Author .....
Department of Mechanical Engineering
May 7, 2021

Certified by .....
Tonio Buonassisi
Associate Professor of Mechanical Engineering
Thesis Supervisor

Accepted by .....
Nicolas Hadjiconstantinou
Professor of Mechanical Engineering, Chairman, Committee on Graduate Students

Improving the Environmental Stability of Methylammonium-Based Perovskite Solar Cells

by

Noor Titan Putri Hartono

Submitted to the Department of Mechanical Engineering
on May 7, 2021, in partial fulfillment of the
requirements for the degree of
Doctor of Philosophy in Mechanical Engineering

Abstract

Perovskite solar cells (PSCs), as an emerging type of photovoltaics, have reached beyond 20% efficiency within a decade. Technoeconomic analysis suggests that PSCs are promising alternatives to the market-dominant silicon, because PSC manufacturing processes are more cost effective due to their solution processing methods. However, the prototypical perovskite material, methylammonium lead iodide ($MAPbI_3$), is environmentally unstable and degrades in the presence of oxygen, light, and moisture. Thus, despite its high initial performance, the degrading performance over time means that the levelized cost of electricity (LCOE) of perovskites is prohibitively high. An improved stability (targeting $<0.25\%$ degradation per year or less) could help improve the LCOE of perovskites to surpass silicon.

Researchers have been incorporating low-dimensional (LD), such as 0D, 1D, or 2D perovskites, to improve PSCs stability. We can obtain LD perovskites by changing any A, B, or X ions in the ABX_3 structures of high-performing 3D perovskites. The A-site cations can be organic or inorganic, which give us a vast number of possible perovskite compounds. Some common examples of 3D perovskite A-site cation are methylammonium (MA) and formamidinium (FA). When the A-site is larger than FA, it forms LD perovskite structures.

This thesis focuses on investigating how to incorporate the LD perovskites as a capping layer to improve the stability of MA-based perovskites, including how to screen and select the A-site cations of LD perovskite capping layers that can improve the $MAPbI_3$ absorber stability, how to improve the stability of $MAPb(I_xBr_{1-x})_3$ mixed-halide, a wide-bandgap absorber for tandem cells and indoor PV applications, and how to incorporate capping layers in inverted p–i–n PSCs device architectures. These 3 questions are answered by combining high-throughput experiments with machine learning analysis. The optoelectronic, structural, and chemical composition properties of the LD capping-3D perovskite absorber materials are probed to identify the degradation mechanisms using advanced characterization methods. This deeper understanding of perovskite degradation and the strategies to solve the instability issue are critical to push PSCs closer toward commercialization.

Keywords: perovskite solar cell, low-dimensional perovskite, capping layer, 2D-3D heterostructures, high-throughput experiment, machine learning

Thesis Supervisor: Tonio Buonassisi
Title: Associate Professor of Mechanical Engineering

Acknowledgments

This thesis would not have been possible without the people in my personal and professional life who have helped me along the way. They have my endless gratitude.

I want to thank my family and friends from different countries, especially the ones in Indonesia. Their encouragement, support, and love are my greatest source of motivation to keep going and reach this point.

I am particularly in debt to the research scientists and postdocs of MIT PV Lab: Dr. Seong-Sik Shin, Dr. Juan-Pablo Correa-Baena, Dr. Shijing Sun, Dr. Ian Marius Peters, Dr. Sarah Wieghold, Dr. Liu Zhe, Dr. Ian Matthews, and Dr. Armi Tiihonen, for their mentorship and guidance throughout my S.M. and Ph.D. journey. Their immense help has shaped me to become a more mature researcher.

I would also like to thank the past and present members of MIT PV Lab: Alex Polizzotti, Jeremy Poindexter, Rachel Kurchin, Sarah Sofia, Amanda Youssef, Mallory Jensen, Felipe Oviedo, Erin Looney, Danny Zekun Ren, Siyu Tian (Isaac), Max Stocker, Sai Nithin Kantareddy, Aleks Siemenn, Richa Naik, Harry Liang, Mariela Castillo, Luke Meyer, Sara Bonner, Michael Kelly, Janak Thapa, and Jim Serdy, for their help, support, and friendship throughout the years. I would also like to thank the MIT PV Lab UROP students: Mariya Layurova, De Xin Chen, Tofunmi Ogunfunmi, Antonio Buscemi, Alex Encinas, Clio Batali, and Isaac Metcalf, for dedicating their time to learn about perovskites and help the experimental and measurement parts of the projects.

Finally, I would like to thank my advisor, Professor Tonio Buonassisi, for his guidance over the past five years, who has mentored and given me advice on research directions. His support in building a global research network has enabled me to do impactful research. I would also like to thank my thesis committee, Professor Betar Gallant (Department of Mechanical Engineering) and Professor Rafael Gomez-Bombarelli (Department of Materials Science and Engineering), for their guidance and resources.

Contents

List of Figures

List of Tables

Chapter 1

Introduction

1.1 Photovoltaics (PV) for climate change mitigation

The earth has experienced global cooling–warming cycles throughout centuries and the evidence from the past 740,000 years can be observed from ice-sheet cores [16, 103]. Previously, the oscillations of 100,000-year and 20,000–40,000-year cycles are attributed to natural causes; however, several studies have confirmed that the current warming period is much more intense than previously observed warming periods [30, 103, 16]. Anthropogenic carbon emission, as shown in Figure 1-1 [37], has increased significantly since 1760, the period when the industrial revolution began. Carbon emission has been predicted to affect climate change significantly [28], even though researchers still disagree on the exact number due to high uncertainty and complicated feedback loops within the models. The global mean sea level has risen 8-9 inches since 1880, and in the United States, it translates to high-tide flooding that is 300-900% more frequent than 50 years ago [77].

The effects of climate change are massive, such as more severe weather and rising sea level [77]. Between 2016-2020, the average global economic losses from weather catastrophes is around 285.60 billion US dollars, as shown in Figure 1-2 [106]. Looking at the trend, this is likely going to keep increasing in the future. They could lead to

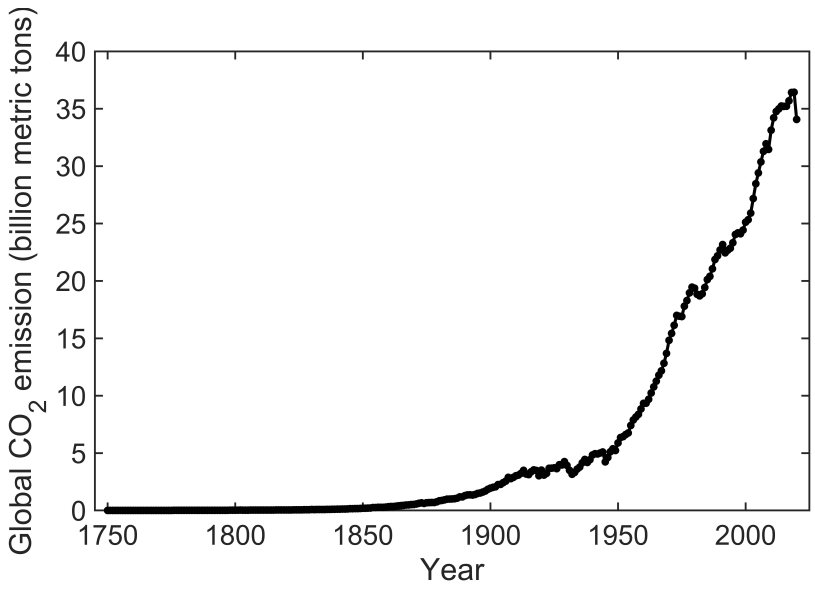

Figure 1-1: The 1758-2020 carbon dioxide emissions from global fossil fuel combustion and industrial processes [37].

displacement and a climate refugee crisis [8]; hence, it is important to address and mitigate the climate change issue early on. To solve this problem, during COP 21 2015 in Paris, more than 150 country representatives agreed to adopt a legally binding international treaty on climate change to limit global warming below 2, preferably 1.5 degrees Celsius, compared to pre-industrial levels [139]. The Paris Agreement is evaluated every 5 years, and each country is expected to take increasingly ambitious climate action in subsequent meetings.

One significant contribution of anthropogenic carbon emission that has become the center of climate change policy is from the energy sector. Energy is necessary for almost every aspect of human life, and access to energy is synonymous with access to civilization. Satisfying future energy demand that keeps growing while decarbonizing the energy generation process presents an unprecedented challenge to society. Transitioning to renewable energy is one strategy to mitigate climate change effect. Therefore, Scientists and engineers globally have taken up the challenge to assist in the development of lower-carbon energy technologies.

Between 2007-2019, the share of renewable power in energy generation has increased from 5.2% to 13.4%, translating to 6.19 petawatts in 2017 [21]. The share

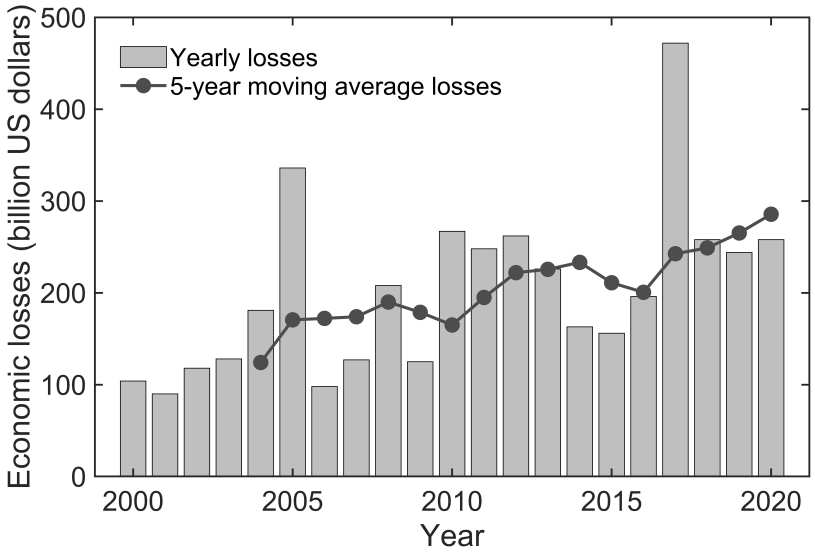

Figure 1-2: The global economic losses due to weather catastrophe in 2000-2020 [106].

of renewable energy in the energy mix continues to grow, despite the setbacks experienced by other energy types due to the COVID-19 pandemic in the past year [1]. However, it is still insufficient to achieve the target of net zero by 2050. It will require 300 GW/year addition of solar photovoltaics (PV) and about 170 GW/year addition of wind power [1]. To achieve such an ambitious goal, a larger renewable energy adoption is necessary. However, an increase in renewable energy share has been slow due to its high installation and system cost, even after the government's subsidy [90], which prohibits getting closer to the zero-carbon emission goal. The Paris Agreement has introduced a framework to achieve the carbon emission level target, and one of them is fully realizing technology development and transfer [139]. Hence, technological advancement in renewable energy is critical to reduce its cost and bring the zero-carbon solution into reality.

1.2 Background on perovskite solar cells (PSCs)

Achieving a high percentage of solar photovoltaics (PV) adoption in the energy market is needed to minimize climate change globally [29, 1]. Silicon is currently the dominant photovoltaic technology, with >90% market share. However, the cost of

silicon manufacturing (and associated factories) presents a barrier for PV adoption. Any technology that can reduce either the cost or initial capital expense investment of solar manufacturing could help advance our climate goals.

Based on that, researchers are exploring less expensive alternative photovoltaic materials, which need to cost less than the current market dominating silicon solar panels. In the past decade, a newly emerging solar cell material called perovskite, has reached beyond 20% efficiency [68], which is comparable to silicon performance. Perovskite solar cells (PSCs) can be fabricated via solution processing methods, that is more cost-effective and more versatile than silicon solar cells, and hence, very promising [100]. Perovskite modules are predicted to cost less than crystalline silicon modules and more mature thin-film technologies such as CdTe, as shown in Figure 1-3 [123]. c-Si, CdTe cost \$0.60 and \$0.64-0.76/W_P, while inverted and perovskite modules are predicted to cost around \$0.41 and \$0.57/W_P, respectively [123, 23], assuming comparable manufacturing scales can be achieved. The difference in cost is mainly attributed to the solution processing of the perovskite deposition process, enabled by the material's defect-tolerant nature [12], which allows it to tolerate a higher concentrations of contaminants, in comparison to silicon solar cells [107].

Despite the promising characteristics of perovskite solar cells, researchers still need to understand and improve perovskite solar cell environmental stability. Current perovskite alloys degrade within days, weeks, or months, depending on the compositions and degradation conditions, and cannot compete with the ≥25-year lifetime of silicon solar cells.

1.2.1 Perovskite structure and dimensionality

"Perovskite" originally refers to the mineral $CaTiO_3$. More recently, its use has expanded to include other crystals with identical cubic structure and shared ABX_3 composition, where A and B refer to +1 and +2 cations, respectively, and X refers to an anion in the -1 charge state. The recently-discovered type of material that is utilized for solar cells is methylammonium lead iodide ($MAPbI_3$), which contains the polar molecule on the A site. Since then, some have broadened the usage of the term

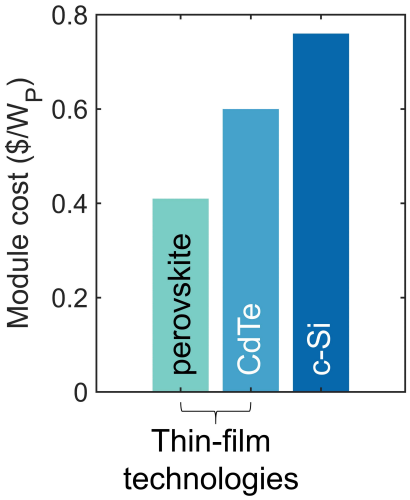

Figure 1-3: The predicted module cost for inverted perovskite in comparison to other PV technologies, assuming comparable manufacturing scale. [123].

"perovskite" to include other tin- and lead-halide materials with perovskite structure, as shown in Figure 1-4; the A-site cation can be either be organic or inorganic. Additionally, "perovskite" has been used to refer to other materials inspired by $MAPbI_3$ that do not assume the ABX_3 composition and/or crystal structure; others call these "perovskite-inspired materials." In this thesis, we use the term "perovskite" to refer to the traditional $MAPbI_3$, as well as perovskite-inspired materials that do not assume the traditional ABX_3 composition.

The traditional perovskite structure (shared by MAPI and $CaTiO_3$) forms an octahedron network with A-site cations as the 'spacer' in the center, making the typical perovskites get their cubic structure.

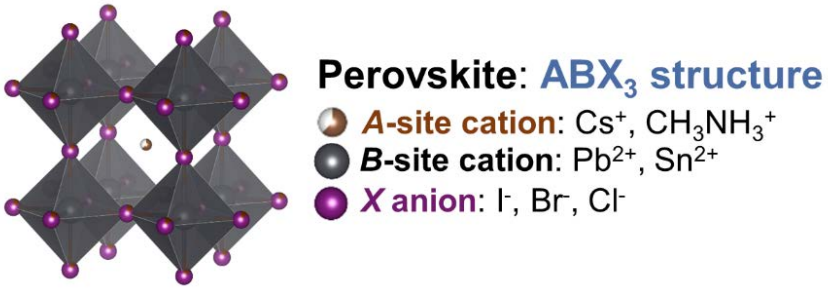

Figure 1-4: The typical ABX_3 structure of perovskites.

The high-performing perovskite solar cells have organic A-site cations, Pb (lead) as

B-site cation, and a mix of I, Br, and Cl as X-anion [113]. However, high-performing perovskite cells degrade readily in the presence of moisture, light, and oxygen [143, 93, 44, 43], and researchers are working on solving this problem. Addressing the stability issue is the core topic of this thesis.

Goldschmidt's tolerance factor

One way to improve these cells' intrinsic stability is by introducing lower-dimensional (LD) perovskite—0D, 1D, or 2D, by mixing and breaking up the 3D octahedron network within the structures [25, 127]. To split the 3D octahedron network systematically, a large A-site cation can be introduced. To quantify the relations between ionic radii of A, B, and X ions, we can use Goldschmidt's tolerance factor [5], as shown in Equation 1.1. Large A-site cations, which form LD perovskite, have large ionic radii and Goldschmidt's tolerance factor larger than 1.00.

$$t = \frac{r_A + r_X}{\sqrt{2}(r_B + r_X)} \tag{1.1}$$

Methylammonium (MA)-based perovskites

Methylammonium (MA, $CH_3NH_3^+$)-based perovskite is one of the most common PSC materials. This specific material fuels the early record-breaking efficiency in PSCs. MA-based perovskite material, especially $MAPbI_3$, has several advantages compared to other halide perovskite materials. $MAPbI_3$ has a direct bandgap of 1.55 eV, which is close to the maximum solar conversion efficiency based on Shockley-Queisser limit: 1.34 eV, long charge-carrier diffusion lengths, defect tolerant nature, and high charge charge-carrier mobilities [40]. $MAPbI_3$ also has a tolerance factor of 0.91 [11], making it a 3D perovskite. The crystal structure of $MAPbI_3$ changes depending on the temperature. At low temperature, 170K, 330K, and 400K, $MAPbI_3$ has orthorhombic $Pnma$, tetragonal $I4/mcm$, cubic $Pm\bar{3}m$, and tetragonal $P4mm$ structures, respectively [95]. In addition, $MAPbI_3$ can be fabricated via solution-processing, which opens up a lot of possible manufacturing routes for the materials.

Despite all the advantages, it is well-known that methylammonium halides are

extremely hygroscopic, in comparison to other *A*-site cations, and readily dissolve in water [20]. This is problematic, because one of $MAPbI_3$ degradation routes is the formation of PbI_2 with CH_3NH_3I or MAI (Equation 1.2), which is hygroscopic. $MAPbI_3$ is therefore sensitive to humidity, and it is known to degrade readily in high-humidity conditions. This challenge needs to be solved either by improving its intrinsic stability, adding a barrier layer, or having a good device encapsulation.

1.2.2 Perovskite solar cells stability and degradation routes

One way to improve PSCs' stability is by mixing LD perovskite into 3D perovskite in the absorber, which improves the intrinsic material stability, as shown in Table 1.1. Different studies have explored various combinations of degradation conditions: low-high RH or relative humidity (low: ambient RH or $< 30\%$ RH, high: $> 50\%$ RH), low-high temperature (low: ambient temperature, high: > 50 °C), low-high illumination (low: no illumination, high: ≥ 1.0 sun), and gas (air, dry air, or inert gas, usually N_2). Various 3D-LD mixed perovskite absorbers have also been explored, some of them focus on mixing 1D Pb-free with 3D perovskite [55], mixing LD perovskite generated by changing the *A*-site cation of the perovskite [57, 73, 147, 151], and mixing organic-free 2D with 3D perovskites for further stability enhancement [76]. The aforementioned studies have shown improvement in environmental stability, although the efficiencies have not reached 20%. In recent years, however, as shown in Figure 1-5, few mixed 3D-2/1D perovskites have reached beyond 20%, however, they mostly contain a trace amount of LD perovskites, which act as dopants. They still perform below the NREL record efficiency cells, though.

The degradation mechanisms of $MAPbI_3$ ($CH_3NH_3PbI_3$), which is one of the most well-studied lead-halide organic-inorganic perovskites, under humid condition happens by two competing reactions: the desorption of MAI (CH_3NH_3I) and the generation of the hydrate phase of $MAPbI_3$ due to water incorporation, which are shown in Equation 1.2, 1.3, and 1.4 [116]. As $MAPbI_3$ degrades into PbI_2, CH_3NH_3I is formed in reaction 1.2. On the other hand, the reaction 1.3 is reversible, and under vacuum

	Composition mixtures	Temperature	Relative humidity, gas	Illumination	Time	Normalized PCE retained	Ref.
1	$(MA-Cs)PbI_3$ with PEA	50-60 °C	30-50% RH, air	1.0-sun	205 hours	∼0-0.5, depends on Cs amount	[57]
2	$FA_{0.79}MA_{0.16}Cs_{0.05}PbI_{2.5}Br_{0.5}$ with PA	20 °C	45% RH, air	-	2000 hours	∼0.5	[147]
3	$MA_3Bi_2I_9$ with $MAPbI_3$	ambient T	30% RH, air	-	1000 hours	0.72	[55]
4	$EDBEPbI_4$ with $MAPbI_3$	ambient T	ambient RH, air	-	3000 hours	∼0.9	[73]
		ambient T	65% RH, air	-	1000 hours	∼0.9	
5	$(Cs_{0.05}(MA_{0.17}FA_{0.83})_{0.95}Pb(I_{0.83}Br_{0.17})_3)_{0.85}(HAPbI_2Br)_{0.15}$	25 °C	30% RH, air	-	2500 hours	∼0.9	[151]
6	$Cs_2PbI_2Cl_2$ with $CsPbI_{2.5}Br_{0.5}$	80 °C	70% RH, air	-	48 hours	∼0.3	[76]
		80 °C	30% RH, air	-	96 hours	0.93	
		25 °C	ambient RH, N_2	-	60 days / 1440 hours	0.95	

Table 1.1: Review of mixed-composition PSCs tested for stability.
MA: methylammonium, FA: formamidinium, PEA: phenylethylammonium, PA: propylammonium, HA: hydrazinium, PCE: power conversion efficiency.

condition, the $MAPbI_3$ can be reformed from its hydrate by H_2O desorption [116].

$$CH_3NH_3PbI_3 \longrightarrow PbI_2 + CH_3NH_3I\,(\text{or}\,CH_3NH_2 + HI) \tag{1.2}$$

$$CH_3NH_3PbI_3 + H_2O \rightleftharpoons CH_3NH_3PbI_3 \cdot H_2O \tag{1.3}$$

$$4\,CH_3NH_3PbI_3 + 2\,H_2O \longrightarrow (CH_3NH_3)_4PbI_6 \cdot 2\,H_2O + 3\,PbI_2 \tag{1.4}$$

Unfortunately, despite the improvement in stability by mixing LD with 3D perovskite, mixing too much LD into 3D perovskites results in lower device performance, as shown in Figure 1-5. Finding the balance between PSCs' stability and performance through compositional exploration is important and needs to be investigated.

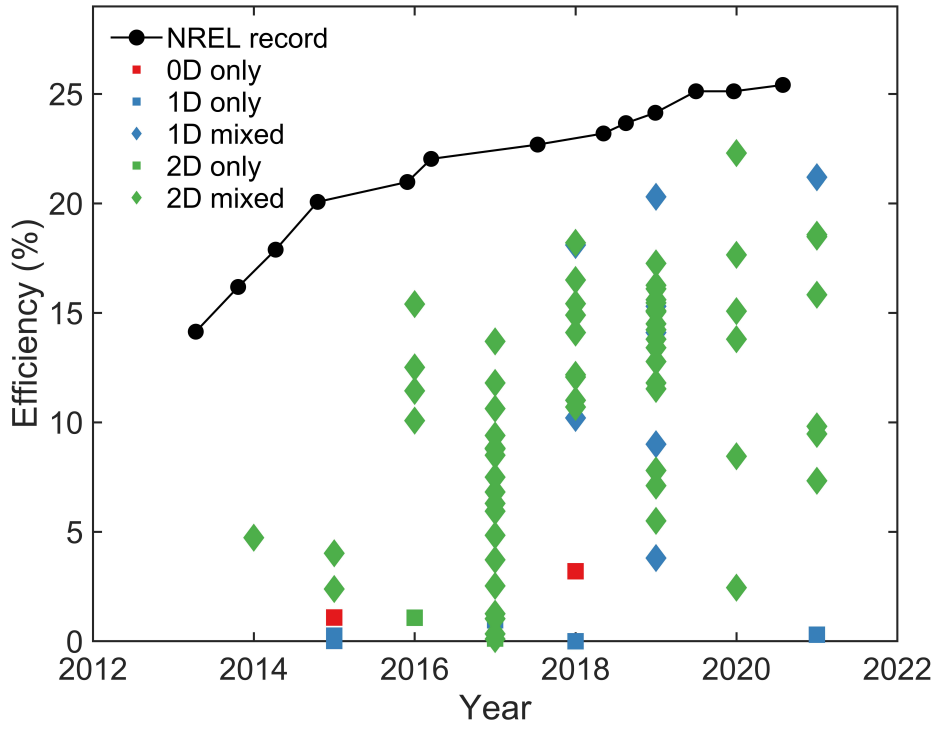

Figure 1-5: Research cell efficiencies for different perovskite dimensionality.

The comparison between best-research cell efficiencies of perovskites from National Renewable Energy Lab (NREL) and the published 3D-LD perovskites in the form of mixing from year to year [68, 41, 120].

1.2.3 PSCs device architecture and fabrication

Photovoltaic materials fall in the semiconductor materials category. When there is external source excitation, the material turns from insulator (non-conductive), into a conductive state. This is due to the relatively low energy gap between valence band maximum (VBM) and conduction band minimum (CBM), allowing charge carriers to jump from one energy level to another upon energy excitation. The insulator, on the other hand, has a high energy gap between the VBM and CBM, making it hard for the charge-carrier hard to jump from one to another band, in contrast, the conductor has its VBM and CBM overlapping with each other, allowing it to be conductive even without excitation. The schematic of these three different types of materials is shown in Figure 1-6.

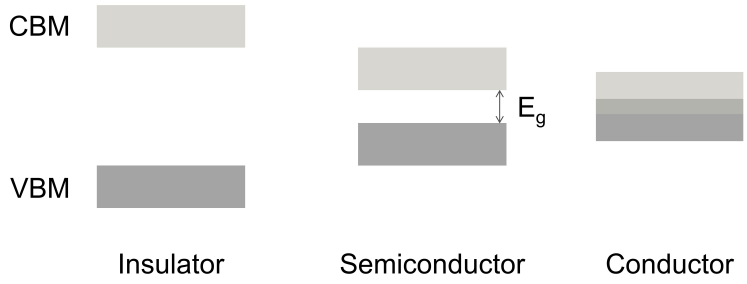

Figure 1-6: The VBM and CBM of different type of materials.

VBM is valence band maximum, and CBM is conduction band minimum. E_g represents the bandgap energy for the semiconductor materials, which is the difference between VBM and CBM.

Unlike silicon solar cells, the perovskite solar cells (PSCs) device structure closely resembles the organic photovoltaic device. The perovskite film only facilitates the light excitation that causes electrons' jump from VBM to CBM, leaving holes behind. To extract the charge carriers and create current, it requires other layers, called electron transport layer (ETL) and hole transport layer (HTL), in addition to conduction layers. The structure is shown in Figure 1-7.

Depending on where the ETL and HTL sandwich the perovskite, there are two different PSCs device architecture: *n–i–p* (which is more widely known as normal structure and is more investigated within the field), and *p–i–n* structure (which is called in-

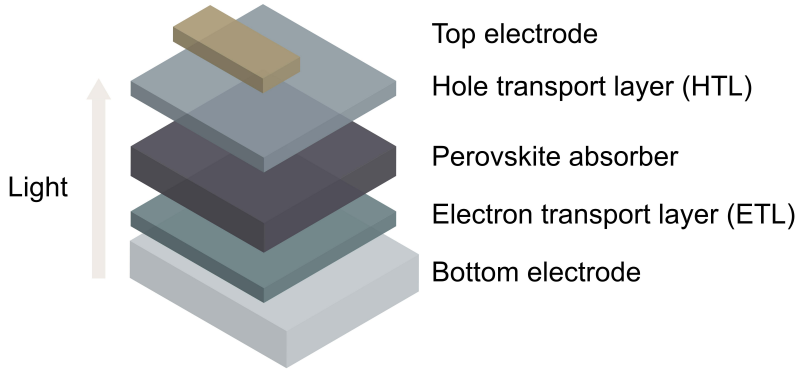

Figure 1-7: The *n–i–p* device architecture for PSC.

verted structure). For the *n–i–p* structure, the ETL and HTL are deposited before and after the perovskite film, while for *p–i–n* structure, it is the other way around. The ETL for *n–i–p* architecture is usually TiO_2 or SnO_2, while for *p–i–n* structure is usually PCBM ([6,6]-phenyl C_{61} butyric acid methyl ester), C_{60}, and their derivatives [84]. The HTL for *p–i–n* architecture is usually spiro-OMeTAD (2,2',7,7'-tetrakis(N,N-pdimethoxyphenylamino)-9,9'-spirobifluorene) or PTAA (poly [bis(4-phenyl) (2,4,6-trimethylphenyl) amine]), while for *p–i–n* structure is usually PEDOT:PSS (poly (3,4-ethylenedioxythiophene) polystyrene sulphonate) [84]. The wide range of possible materials combination for each layer also allows low-temperature conditions during the fabrication process, which is important for fabricating flexible perovskite solar cells [153].

Looking at the layer atop of the perovskite absorber, one key feature that this layer needs to have (HTL for *n–i–p* and ETL for *p–i–n*), if it is deposited via solution processing, is the solvent compatibility between the top layer and the absorber. The solution deposited at the top should not dissolve the perovskite absorber layer underneath. Once the solvent system is established, the available manufacturing process for the device expands. Solution processing allows the perovskite and other layers to be deposited via blade-coating, slot-die coating, screen-printing, spray-coating, and inkjet printing [109]. Due to the high variability of the film morphology in solution-based processing, researchers have also explored a vapor-based method that is solvent-free but limits scaling-up methods [109]. Few examples of vapor-based pro-

cesses are co-evaporation of organic and inorganic precursors (PVD) and alternating precursor deposition [109].

1.3 Background on data-driven perovskite research

The PSCs-related research initiative utilizing data-driven processes, advanced statistical methods, and machine learning emerge quite recently. The PSC research usually focuses on experimental-based research or theoretical-based computational research, such as density functional theory (DFT), to predict PSCs material properties and see the feasibility of new composition materials. The data-driven perovskite research initiative only started after PSCs reached more than 10% efficiency, indicating that this material class is promising for the future generation of photovoltaic materials.

Since the halide organic-inorganic perovskite material class only gained traction in the past decade, the exploration of wide compositional space and material properties prediction dominates the data-driven perovskite research. This exploration benefits the researchers in narrowing down the possible successful and synthesizable materials. The examples for this type of machine learning research are bandgap prediction [105, 79, 125, 53], device recovery cycle prediction [52], perovskite formability [104, 99, 58, 112] or thermodynamic stability [74] prediction of a given A, B, and X ions, classification of X-ray-diffraction (XRD) patterns [97, 130], and single crystal growth prediction [64].

At the end of another spectrum, machine-learning-based perovskite research uses active learning to drive the high-throughput experiment iteratively to achieve a target value, which could range from optimizing composition to processing condition to achieve a stable perovskite [131] or photoluminescence spectrum target [49].

1.3.1 Supervised learning for predicting material properties

Supervised learning is a method to find the relation between input (X) and output (y). A linear regression, for instance, is a common technique that falls within the supervised learning area. After a supervised learning model is trained, the model can

predict the output of certain input variables, which is useful for PSCs-related research where there is a wide, unexplored compositional space.

Supervised learning models are generally categorized as two: regression and classification. The main difference between the two methods is the type of output (y). Regression models are used for continuous output, while classification models are used for discrete output or categorical. Regression models have previously been used for predicting bandgap [105, 79, 125, 53]. On the other hand, classification models have previously been used for predicting single crystal growth (binary, yes/no) [64], or perovskite dimensionality through XRD patterns [97, 130].

There are different types of supervised learning algorithms. Some examples are as follows [31, 117].

1. Linear regression. This method fits a linear equation to relate the input with the output of the model.

2. Support vector machine (SVM) or support vector regression (SVR). This works by maximizing the distance between the classes.

3. Decision tree algorithm, such as random forest and gradient boosting tree. Tree-based algorithms predict the output by splitting the population into subsets of more homogeneous sub-population. The differentiator between subsets works like a branch in a tree. It is usually used for classification, even though it is now common to use it for regression by regressing each sub-population at the end of the branch.

4. K-nearest neighbor. This algorithm works by assigning an unlabeled sample point to the label of the nearest neighboring points. Choosing a good k is therefore important in training the model.

5. Artificial neural network. This algorithm is based on the neurons, which act as hidden layers between input and output. By tuning how many hidden layers there are, each neuron's weight, and the activation function, the neural network can be trained.

1.3.2 Unsupervised learning to find new insights

Unsupervised learning is a model training for labeled/unclassified data [154]. The unsupervised learning method has not been as widely used as supervised learning for PSCs. One example is using supervised learning to rationalize the key structural parameter governing nonadiabatic electron-phonon coupling and the bandgap, which is the I–I–I angle in methylammonium lead iodide ($MAPbI_3$) perovskite [157]. In other fields, unsupervised learning has been used to cluster the candidate materials for solid-state lithium-ion conductors and discover novel conductors [156]. Unsupervised learning has also been used to recommend materials for functional application based on research literature [137].

1.3.3 Active learning for autonomous experiment

Active learning is a machine learning type where the algorithm can give suggestions for the next round of experiments based on the data that it is already trained on. This helps reduce bias from the experimenters and helps get into an optimum point, which could be a minimum or maximum point(s) depending on the target, faster. One commonly used algorithm for this purpose is Bayesian optimization (BO), which utilizes Gaussian process regression to predict a new parameter based on the previously measured parameter [36]. BO has been applied to find the most stable lead halide perovskite [131], the optimal band structure and thermal transport coefficient for layered materials consisting of transition metal dichalcogenides [6], the successful region for coarse-grained simulation of biomolecules [61], and the amorphous and liquid hafnia (HfO_2) generation over a wide range of conditions [118].

Researchers have tried optimizing PSCs for a bounded, low-dimensional space using active learning [131]. However, this leads to finding local minima/maxima within the small space, although there is a high possibility that the global minima/maxima of the target metric exist somewhere else. Therefore, the current challenge for active learning in PSCs is its high-dimensional parameter space, considering multiple layers in the PSC device, possible compositions for each layer, and variation of pro-

cessing conditions for each layer and each composition. The current computational power does not allow us to do grid search and full factorial sampling for the high-dimensional space. Hence, knowing how to sample such high-dimensional space is important to ensure that the researchers do not end up with local minima/maxima, instead of global minima/maxima of the target metric in active learning methods.

1.4 Thesis outline

There are two ways of incorporating lower-dimensional (LD) perovskites in the photoabsorber layer to improve $MAPbI_3$ stability: mixing it in perovskite absorber (mixing method), or depositing it on top of the absorber as a capping layer, or widely known as buffer layer in photovoltaics research (capping method). The former method has been explored widely, as shown in Table 1.1. However, a large addition of LD perovskites in the mixing method leads to low efficiency, as shown in Figure 1-5, one of the reasons is due to a reduction in charge-carrier mobility [46, 47]. In the capping method, the LD perovskite capping layer itself is expected not to interfere with the bulk charge transport of the 3D perovskite, unlike the mixing method, but still protect the material from the environment. Since this method only recently emerges, much work still needs to be done in understanding how we pick the materials that give the best performance in terms of stability and efficiency, and how we deposit it for an inverted device. Therefore, this thesis focuses on the capping method for improving PSCs, specifically the prototypical MA-based perovskites stability.

The primary areas in this thesis are shown in Table 1.2, where it covers the capping layer material screening for improving the stability of $MAPbI_3$ absorber (Chapter 3), the capping-mixed-halide pair screening for optimum stability (Chapter 4), the capping layer exploration for $MAPbI_3$ absorber in inverted PSCs (Chapter 5), and implementing capping layer for improving the stability of absorbers beyond $MAPbI_3$.

Chapter	Absorber	Sample type		Goals
		Film	Device	
3	$MAPbI_3$	Yes	-	Capping materials screening
4	$MAPb(I_xBr_{1-x})_3$	Yes	Yes (n–i–p)	Capping-absorber materials screening
5	$MAPbI_3$	Yes	-	Deposition method development
6	$Cs_{0.17}FA_{0.83}PbI_3$	Yes	Yes (p–i–n)	Degradation mechanism understanding

Table 1.2: Thesis chapters overview.
MA: methylammonium, FA: formamidinium.

1.4.1 Data-driven stability analysis for capped-$MAPbI_3$ absorber

The first part of the thesis focuses on picking the capping layer material to extend the stability of $MAPbI_3$. Due to the large compositional space for the organic A-site cation, as shown in Figure 1-8, a method to screen the materials under elevated temperature and elevated humidity conditions is required to understand the design guidelines for choosing the stable capping layer material. Once we have the design guidelines for this capping layer, we need to optimize the deposition processing condition.

A data-driven method is chosen to screen the capping layer materials and fabrication processing conditions simultaneously. The database's molecular properties coupled with the processing conditions, which are referred to as features, are trained using supervised machine learning methods to predict the degradation onset on the capped perovskite absorber films. The trained models are then used to analyze the feature importance rank. This rank can investigate which features contribute significantly to the degradation onset, shedding a light on which type of A-site cation will improve the stability significantly.

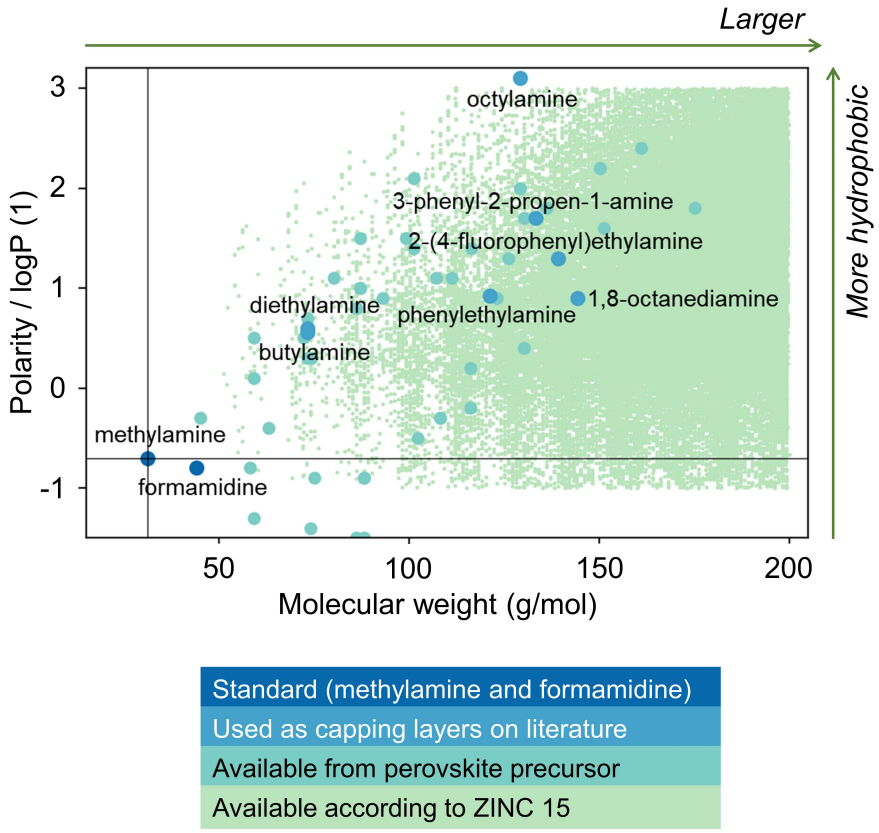

Figure 1-8: Amine organics available according to ZINC 15 database [126].

This figure only includes the substances with molecular weight up to 200 g/mol, and $logP$ from -1 to 3, totaling more than 200,000 possible amine organics.

1.4.2 Capping layer screening for mixed-halide, MA-based absorber

After getting the design guidelines for choosing a capping layer material, the second part of the thesis focuses on finding the optimum capping layer material for absorbers with various bandgaps, especially considering that the perovskite bandgap is tunable to fit various purposes, including perovskite-perovskite tandem cells, and indoor application [85]. For those applications, we need different types of PSCs: narrow and wide bandgap (NBG and WBG, correspondingly), which will capture the energy at a specific light spectrum range.

One common way to increase the bandgap in PSCs is by mixing the halide in X-anions of the perovskite absorber [3]. For NBG, the halide is usually iodine, while for WBG, it is usually bromine or even chlorine, which has a smaller atomic mass [3, 146]. This increase of bandgap is due to the change in Pb–I bond after Br or Cl addition, making the structure distorted [87].

This thesis chapter focuses on screening the suitable capping layer for MA-based wide bandgap perovskites. The optimum capping layer from previous chapter, along with new 1D capping layers are introduced and tested. Advanced characterizations are then used to investigate why certain capping-absorber pairs are better than the others.

1.4.3 Improving the stability of $MAPbI_3$ in inverted device architecture

In the first two parts of the thesis, the capping layer is geared towards *n–i–p* device, where the electron and hole transport layers (ETL and HTL) are located at the bottom and top of the absorber, respectively. For this type of device, the capping layer is deposited between the absorber and the HTL. However, in the inverted device, i.e. *p–i–n*, the ETL and HTL are switched, so they are at the absorber's top and bottom.

Even though many PSCs research focuses on *n–i–p* device architecture, the *p–i–*

n device also needs to be improved. Based on recent technoeconomic analysis, an inverted perovskite solar module is expected to be cheaper ($\$0.41/W_P$) [123], while a normal (n–i–p) module is expected to cost $\$0.57/W_P$ [23]. Thus, it is important to push the boundary of p–i–n device stability to increase the probability of pushing PSCs into the commercial market.

However, the inverted device architecture poses an extra challenge: where to deposit the capping layer best. Several studies have shown that there is currently no consensus on where to best put the capping layer to improve both stability and performance [67, 83, 45], as shown in Figure 1-9. When the capping layer is deposited between the absorber and ETL, environmental stability is improved, which is expected. However, the device performance is similar to bare absorber with no capping layer [83]. On the other hand, when the capping layer is deposited between both interfaces with ETL and HTL, the stability is improved, but the device performance is reduced [67]. The last option, which is inserting the capping layer between the absorber and HTL, seems to work well to improve stability and help with the surface passivation, which leads to a reduction in trap-assisted nonradiative recombination and improved efficiency (c) [45]. The last option warrants a further investigation, to understand the underlying mechanism behind the stability and performance improvement due to that particular capping layer configuration. In addition to that, since the absorber and capping layer deposition relies on solution-based processing, solvent compatibility becomes extremely essential. During each layer deposition, the subsequent layer's solvent choice should not dissolve the layers underneath.

This thesis focuses not only on finding the capping layer that works well in improving stability but also soluble in the solvent that will be compatible with both prior and subsequent layers.

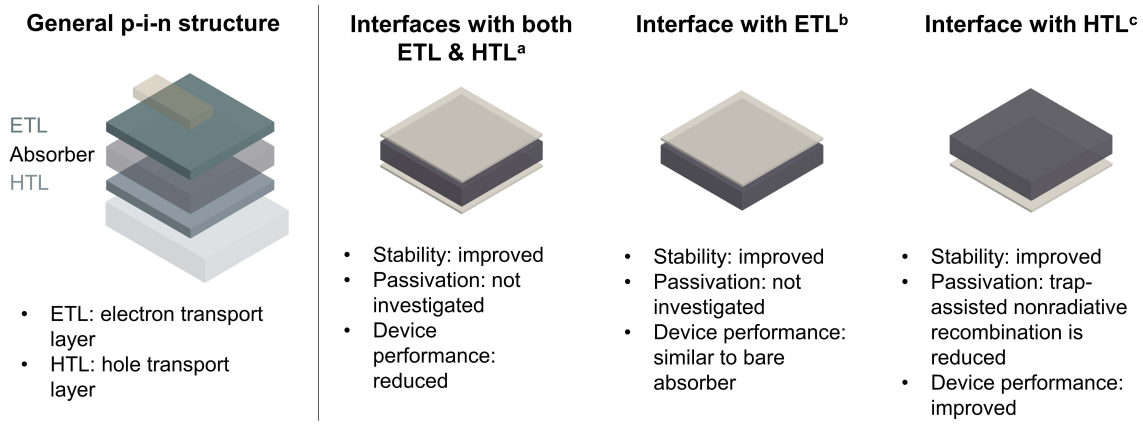

Figure 1-9: Possible locations for capping layer in a p–i–n PSCs device.

The 3 possible locations for the capping layer in p–i–n device are: in the interfaces with both ETL and HTL (a) [67], in the interface with ETL (b) [83], and in the interface with HTL (c) [45].

1.4.4 Departing from $MAPbI_3$: the case of cesium-formamidinium-based PSCs

After optimizing LD perovskites in the capping layer for specific MA-based absorbers, and exploring the possible methods to deposit the capping layer for the inverted devices, it is now time to bring the film-level optimization to the device level, even the encapsulated device level. This is important to ensure that PSCs technology indeed will be commercialized and present more alternatives in the solar panels market for a smooth energy transition.

While $MAPbI_3$ is a promising material for future solar panels, its challenging stability issue has also shifted researchers' interests to discover alternative perovskite materials. Some of the promising candidates are $CsPbI_3$ and $FAPbI_3$, and they are sometimes also doped with $MAPbBr_3$ and $MAPbCl_3$, which also have high efficiency [59]. A study by Sun, et al. also shows that there is an optimum composition mixture between $MAPbI_3$, $FAPbI_3$, and $CsPbI_3$ for better stability, which is $Cs_{0.17}MA_{0.03}FA_{0.80}PbI_3$ [131]. This will also need to be optimized alongside other layers within the device.

This thesis chapter focuses on the initial exploration of how Cs-FA-based PSCs'

stability is different at the film and device level, especially in the inverted device architecture that is predicted to cost lower in manufacturing. Different degradation conditions are explored, such as high temperature but low humidity and high temperature and humidity. We also observe how the degradation mechanisms in these compositions are different from $MAPbI_3$. In the case of $FAPbI_3$ and $CsFAPbI_3$, their intrinsic phase stability determines the reliability of their PSCs. Both α-$FAPbI_3$ and α-$CsPbI_3$ phase are dark and good solar cell materials at above 160 °C and room temperature, respectively [148]. However, the δ-$FAPbI_3$ and δ-$CsPbI_3$ are yellow and photovoltaically inactive below those temperatures [148]. Therefore, this intrinsically unstable material poses a different set of challenges than the MA-based perovskite, where the main culprit is humidity.

In the future, co-optimizing these absorbers and capping layers and other layers, such as ETL, HTL, electrodes, and encapsulation, will be essential in finding the most stable and high-performing PSCs. This thesis explores this direction, starting by optimizing the capping layer for MA-based perovskite.

Chapter 2

Fabrication, characterization, and machine learning methods

2.1 Film and device fabrication methods

The film and device fabrication methods here represent the general fabrication protocols followed in this thesis. However, each project/thesis chapter might require a slightly different set of samples. In some cases, samples are also sourced from collaborators, which are also fabricated in slightly different techniques.

2.1.1 Absorber film fabrication

The simplest perovskite absorber film is methylammonium lead iodide ($MAPbI_3$). This material can be deposited on either fluorine-doped tin oxide (FTO) glass or microscope glass slides. The substrates are previously cut in 1-inch by 1-inch size and cleaned in a sonicator with the following solutions, each for 15 minutes: 2% Hellmanex in deionized (DI) water, DI water, and isopropyl alcohol. After that, the samples are dried for 10 minutes before cleaned using UV-ozone cleaner for 15 minutes.

While the substrates are undergoing cleaning process, we prepare the perovskite precursor solution. First, we prepare the PbI_2 solution by mixing 1 gram of PbI_2 (TCI, 99.99% trace metals basis) with 145 µL of dimethylsulfoxide or DMSO (Sigma-Aldrich,

anhydrous $\geq 99.9\%$) and 1301 µL of *N,N*-dimethylformamide or DMF (Sigma-Aldrich, anhydrous 99.8%); the DMF: DMSO is in 9:1 ratio. Second, on a separate vial, for every gram of methylammonium iodide (MAI $> 99.99\%$, GreatCell Solar), add 505 µL of the PbI_2 solution, and 6 µL of 9:1 DMF: DMSO solution. As a result, we obtain a PbI_2-excess solution (1:1.09 MAI: PbI_2).

65 µL of this solution is then deposited on the substrate and spin-coated using a 2-step deposition. 10 seconds after the second step of the spincoating, 150 µL of chlorobenzene is dropped as an anti-solvent.

2.1.2 Device fabrication

For the *n–i–p* device, the layers from the bottom to the top are FTO electrode, TiO_2 compact and mesoporous or SnO_2 layer for electron transport layer (ETL), perovskite absorber, capping layer, spiro-OMeTAD layer for hole transport layer (HTL), and gold electrode.

The FTO substrate is first etched using 1:1 HCl (Sigma-Aldrich): DI water solution. Spread some of the zinc powder (Sigma-Aldrich) onto the part that will be etched evenly. Drop roughly 1 mL of the DI water-HCl mix onto it. Brush off the zinc powder. Clean with DI water, and repeat the etching process for the second time. After that, clean using 3 different solutions in the sonicator: Hellmanex 2% with DI water, DI water, and isopropyl alcohol.

The compact TiO_2 layer is done by doing spray pyrolysis. The etched-FTO glass substrate is annealed on the hotplate at 500°C. Titanium diisopropoxide bis (acetylacetonate) (Sigma-Aldrich) is mixed with ethanol in a 1:10 ratio, with a total of 1 mL. Using a spray gun, the solution is sprayed to the substrate evenly. The substrate is then annealed for another 30 minutes before being taken out. The stock solution is made for the mesoporous solution by mixing 1:5 w/w of TiO_2 paste: solvent mix (3.5:1 terpineol: 2-methoxy ethanol, v/v). The mixed solution is then filtered to obtain a homogeneous solution, and 60 µL of the solution is deposited on the substrate. The substrate is then spincoated and annealed at 150 °C for 5 minutes.

The perovskite absorber is then deposited based on the protocol on Subsection

2.1.1

The precursor solution for spiro-OMeTAD is prepared by mixing 0.05 g of spiro-OMeTAD (Sigma-Aldrich) with 11.33 µL of 1.8 M LiTFSI salt (Sigma-Aldrich) in acetonitrile , 19.72 µL of tert-butylpyridine (Sigma-Aldrich), 4.90 µL of 0.25 M FK209 Co salt (Dyenamo) in acetonitrile, and 546.9 µL of chlorobenzene. 60 µL of the solution is then deposited on the substrate and spincoated.

For the gold electrode part, 100 nm of Au pellet is deposited using a thermal evaporator. A mask is put over the substrate to define the active area for the solar cells.

2.2 Materials characterization

To investigate the material, including structural, optoelectronic, and morphological properties, various laboratory-based and synchrotron-based characterizations are conducted at both film and device levels.

2.2.1 Laboratory-based characterization

UV-Vis spectrophotometer

The film's transmission and reflection are measured using UV-Vis (PerkinElmer), between 350-1000 nm. The absorptance can therefore be calculated by subtracting the transmission and reflection from 100%. The bandgap can therefore be obtained using the Tauc plot method [133]. The perovskite film is deposited on a glass substrate for this measurement.

Fourier-transformed infrared (FTIR) spectroscopy

FTIR is a tool to measure the absorption or emission in the infrared spectrum. This helps to identify certain compounds, especially in organics, within a sample of solid, liquid, or gas. We can observe the signal from bond stretching, bending, and twisting in the organics compound and use them as a molecular fingerprint to identify

compounds' presence. In this thesis, because we mostly focus on a thin-film surface, we use ATR (attenuated total reflection) mode using ZnSe crystal, which probes the chemical bonds on the surface. The perovskite film is deposited on a glass substrate for this measurement.

X-ray diffraction (XRD)

X-ray diffraction can be used to measure the crystal structure. We use a powder X-ray diffraction (PXRD) tool (SmartLab) to investigate what phases are present in the sample. The optic setting is on general medium PB/PSA, using Cu K-α source, and the XRD is usually measured between $2\theta = 5°$-$60°$. The perovskite film is deposited on a glass substrate for this measurement. The tool used is part of shared experimental facilities, MIT Materials Research Laboratory.

Scanning electron microscopy (SEM)

The field-emission scanning electron microscope (FESEM, Zeiss Ultra 55, or Zeiss Supra 55 VP) is used to observe the surface morphology, including the grain boundaries and the cross-section in the device. A low electron beam ($\leq$3 keV) is used to avoid damaging the samples. The perovskite films are deposited on FTO glass substrates to avoid charge-buildup on the surface and are subsequently placed on an SEM stub. FESEM tools used are part of shared experimental facilities, Harvard University Center for Nanoscale System.

X-ray photoelectron spectroscopy (XPS)

XPS (Thermo Scientific K-Alpha+) is used to measure the elemental composition and their chemical states on a sample's surface using an X-ray source (Al K-α). The field gun is on, and the high-vacuum environment is maintained during the measurement. Depending on the samples, we usually investigate the high-resolution signal of C 1s, N 1s, O 1s, Pb 4f, I 3d, Br 3d, and the XPS survey. The films are specifically deposited on FTO glass. XPS tool used is a part of shared experimental facilities, Harvard University Center for Nanoscale System.

Device J-V characterization

Devices are measured using a J-V characterization tool that measures the current density (J) and the voltage (V) using a source meter (Keithley 2420) as the devices are illuminated using a solar simulator (Newport, Oriel Class AAA, 91195A, AM 1.5 G) at $100\,\mathrm{Wcm}^{-2}$. Before the measurement is done, the tool is calibrated with a Si-reference cell certified by NREL.

Degradation test

The degradation test is done in a chamber that is built at MIT PV Lab. The degradation chamber consists of 4 important parts.

1. **The hot plate**. This hot plate can fit 4×7 samples with the size of 1×0.5 inches. This will maintain the temperature of the substrate at a certain level throughout the test. There is a control system that helps to maintain the same temperature at all times.

2. **The relative humidity control system**. Since the relative humidity (RH) fluctuates depending not only on the system but also on the humidity outside the chamber, having an RH control system is important to maintain the RH throughout the degradation test. In this case, we use a simple Arduino program connected with the Adafruit Si7021 humidity sensor, which drives the fan on top of the water reservoir when the RH reaches a certain level.

3. **The light source**. The light source is important for capturing the images clearly. Having a 1-sun light source, for instance, can be an option to introduce light-induced degradation into the system. However, in this case, we minimize such degradation and only use the 0.15-sun light source for the clarity of the captured images.

4. **The camera**. The camera is a USB CMOS camera, without IR cut filter (Thorlabs DCC1645C-SP3), which can be programmed using LabView to capture images every few minutes, for instance, throughout the degradation process.

To ensure that the color of the captured images is the same as the actual color, at the beginning of each run, an image of the X-Rite ColorChecker Passport Photo is taken. A small ColorChecker Passport is also placed next to the samples as a color reference point. The colors are also calibrated using 3D thin-plate spline color warping method in L*a*b color space, and the resulting data were transformed back to red, green, blue (RGB) color space [86].

The images collected are in JPEG, PNG, and BMP formats. They are then processed and calibrated. Finally, the average red, green, blue (RGB) values for each time point for each data is extracted as a CSV file, based on the image analysis protocols established in SPProC GitHub [136]. The time and RGB values for each sample can then further be analyzed for different purposes.

2.2.2 Synchrotron-based characterization

We investigate the surface and the bulk crystal structure using a high-throughput grazing-incidence wide-angle X-ray scattering (GIWAXS) at beamline 11-BM (CMS) Complex Materials Scattering, NSLS-II, Brookhaven National Laboratory. The data is processed using SciAnalysis to convert the WAXS images into the data in q-space. The perovskite film is deposited on a 0.25-inch by 0.5-inch glass substrate (microscope glass slides) for this measurement.

2.3 Machine learning methods

In some thesis chapters, machine learning-based analysis is used, specifically supervised learning using regression (continuous output) and Shapley value analysis. To do these analyses, we need first to construct the dataset, either collecting from an existing database, using the experimental data result, or obtaining from simulated values.

2.3.1 Dataset

Depending on the thesis chapters, the dataset comes from 3 different aforementioned sources, (1) existing database (such as PubChem, ZINC15), (2) experimental result, and (3) simulated values. Using the database is important in initial screening and defining the compositional space. The experimental result is often used as the target output for prediction in machine learning. Lastly, simulated values are important for the novel materials which do not exist in the database yet, but are still important for training the machine learning algorithm. In this case, we use ChemDraw and ChemOffice software package (PerkinElmer) to find the approximate values of some key properties, such as topological polar surface area and partition coefficient.

2.3.2 Regression model training

Scikit-learn package in Python is used to do regression model training [101]. Several regression models are trained, including linear regression (LR), K-nearest neighbors (KNN) regression [2], random forest (RF) regression [50], gradient boosting (GB) regression with decision trees [38], support vector machine regression (SVR) [22], and multilayer perceptron neural network (NN) with three hidden layers (each has 128, 256, and 64 units) using Adam solver [63]. Before training the models, the data is pre-processed, such as normalization (calibrating the mean to zero and scaling to unit variance). However, note that some models do not require normalization in their data, such as tree-based models (random forest, gradient boosting). The next step is tuning the hyperparameters for different models using the GridSearchCV function in scikit-learn, which performs an exhaustive search for the best parameters with the lowest 5-fold cross-validated root mean squared error (RMSE). The observation versus prediction plot is generated to help to investigate if the model is overfitting.

2.3.3 Shapley value analysis

After training the regression models with the dataset and obtain the best model with optimized hyperparameters, we can use another toolset to interpret the model and

derive an insight from it. SHAP, which stands for Shapley Additive exPlanations [80], serves as a feature importance rank that shows how each feature/input variable affects the model's output. SHAP is the state-of-the-art method of extracting feature importance rank because it utilizes game-theory-based Shapley values to calculate each feature/input variable's contribution to the model's output, resulting in a fairer and more robust rank across various models.

Chapter 3

Capping layer design for $MAPbI_3$

3.1 Capping layer method and its large compositional space

The capping layer method refers to the deposition of a thin layer of LD perovskite atop of the perovskite absorber for improving stability or surface passivation. This method emerges after researchers find that even though mixing LD perovskite into 3D perovskite absorber improves PSCs' stability, the reduction in performance hinders the further development of this mixing method. The added benefit of surface passivation and band energy engineering for the capping method pushes the research more towards this direction [149].

Incorporating LD perovskite as a capping layer has been shown to improve stability [94]. For example, depositing 2D phenylethylammonium (PEA) perovskite on top of 3D formamidinium lead iodide ($FAPbI_3$) perovskite improves the device stability for up to 60 days under ambient conditions (dark, 30-40% humidity, and 25 °C) [94]. Additionally, the surface passivation is also improved. For instance, the same PEA-based 2D perovskite capping layer has been shown to improve the surface passivation for methylammonium lead iodide ($MAPbI_3$) film based on longer emission lifetime of capped film observed using the time-correlated single-photon counting (TCSPC) method [19]. Comparing the same material deposited as absorber mixture

as supposed to capping layer, the capping device's efficiency reaches 21.3% [94], in contrast, the mixed perovskite only reaches 4.7% [121]. Using the mixing method, the PEA/MA perovskite mixture results in mixed 2D/3D perovskite structure, namely Ruddlesden-Popper structure (such as $(PEA)_2(MA)_2[Pb_3I_{10}]$) [121]. Even though this method improves the stability for over 46 days with air exposure at 52% relative humidity (RH), it only achieves sub-5% efficiency [121], unlike the device improvement in the capping layer method that also benefits from surface passivation due to reduced defects and trap states [19].

There are two categories of capping layer deposited: the LD perovskite layer and the barrier layer. The LD perovskite layer is formed by reacting the AX ammonium halide salts with the excess PbI_2, forming a thin LD perovskite layer on the surface [94, 19]. However, the barrier layer only forms a sacrificial layer at the top of the absorber to reduce interaction between the perovskite with the layer on top, for instance, fullerene end-capped polyethylene glycol (C60-PEG) [39], C_{12}-silane [152], trioctylphosphine oxide (TOPO) [7], and tetrafluoroterephthalic acid (TFTPA) [160]. This thesis chapter explores the LD perovskite capping layer instead of the large molecules as a barrier layer.

The deposition of the LD perovskite capping layer is utilizing solution-based processing, similar to the perovskite absorber. The difference between capping layer deposition and absorber deposition is highlighted in Table 3.1. The notable difference is in the thickness; the capping layer is much thinner than the absorber layer due to low capping layer precursor solution concentration and high spincoating speed for the deposition.

As previously mentioned, one way to create LD perovskite is by introducing large A-site cations, which is the same in the capping layer case. The capping layer comes from AX salt, where A is the large cation, and X is the halide, which reacts with the excess PbI_2 from the perovskite absorber layer underneath and forms LD perovskite. Several capping layer materials have been explored, such as n-hexyltrimethylammonium bromide [60], $(CF_3)_3CO(CH_2)_3NH_3I$ [26], Eu-porphyrin complex [35], 1,8-octanediammonium iodide [81], diethylammonium iodide [56], 3-

	Absorber layer	Capping layer
Solvent	DMF and DMSO mixture	Isopropyl alcohol (IPA)
Concentration	Usually 1-1.5 M	5-20 mM range
Deposition step	2-step, with chlorobenzene as anti-solvent	1-step, high speed
Annealing temperature	100 °C	100 °C
Annealing time length	10 minutes	10 minutes

Table 3.1: The difference between capping and absorber layer deposition process.

phenyl-2-propen-1-amine [32], and many other organic halide salts encompass different functional groups. Considering all the possible organic compositional space for *A*-site cations is really large, as shown in Figure 1-8, and researchers currently use the trial-and-error method to explore this space. It is also harder to compare each result side-by-side due to differences in degradation conditions, e.g., illumination level, humidity level, gas within the chamber, heating temperature, and variability during the deposition process. To move forward and ultimately find the best capping layer material, screening various materials under the same degradation condition with uniform processing conditions deposition, and find the design guideline for the AX salts are important and the main focus of this thesis part [48].

3.2 Project workflow

To find the best AX halide salts for the capping layer, understanding the design guideline in selecting the material is important. The following research questions are investigated to find the design guideline.

1. What kind of AX halide salt and processing condition extend the environmental stability under elevated temperature and humidity of the perovskite absorber the most?

2. What is the mechanism behind the stability improvement of the capping layer?

To answer those research questions, a specific project workflow is introduced, which is shown in Figure 3-1.

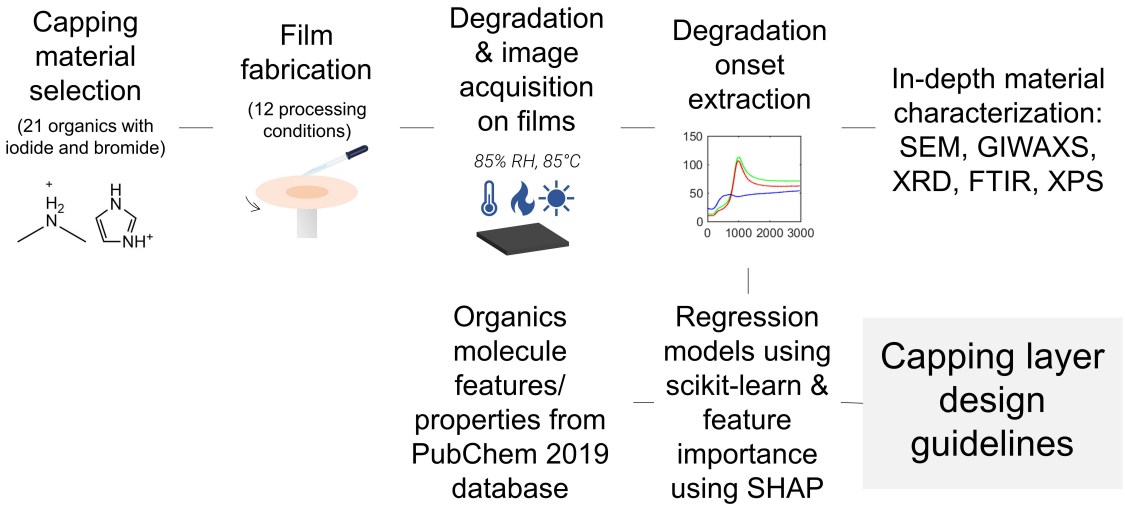

Figure 3-1: The workflow for obtaining capping layers design guidelines.

We start by choosing the halide salts that cover the varieties explored in the literature. Since this part of the thesis focuses on the capping layer material screening, the absorber material is kept the same throughout the project: methylammonium lead iodide ($MAPbI_3$). After the film is fabricated under 4 different annealing temperatures (50, 75, 100, and 125 °C) and 3 different concentrations (5, 10, and 15 mM), totaling 12 different processing conditions.

The next part is data acquisition, and time efficiency is important in this case. During the initial capping layer material screening, it is important to allocate the experimental time strategically because we want to start with the measurement that will give us more data at the beginning and less data but a deeper understanding at the end. Therefore, since the highest amount of data generation per time comes from the environmental degradation chamber, where we degrade films, this data acquisition is the first screening step. We also utilize advanced analysis and train machine learning models to find how the processing condition and material properties affect material stability. The material properties can be obtained easily from the PubChem 2019 database [62], and the machine learning models are available on the scikit-learn pack-

age for Python [101]. SHAP analysis is conducted on the trained machine learning models to understand further the interaction between the input (processing conditions and molecular properties) and the output (the stability result) [80], showing the feature importance ranking. This will help get the design guideline and inform us what kind of molecular properties and processing conditions are important.

After finding the most stable capping layer material, we do various advanced characterizations to understand the mechanism behind the capping layer's stability improvement. To understand the films' crystal structure, we do X-ray diffraction (XRD), as well as grazing incidence wide-angle X-ray scattering (GIWAXS), to see how the bulk crystal structure changes in comparison to the surface. Besides the crystal structure, we also look at the change within the organic *A*-site cations using Fourier-transform infrared spectroscopy. The morphology of the films is also investigated using scanning electron microscopy (SEM). Lastly, the general chemical composition before and after degradation is checked using X-ray photoelectron spectroscopy (XPS).

3.3 Capping layer materials screening

3.3.1 The materials and solvent choice

This thesis focuses on slightly larger *A*-site cations, with maximum carbon atoms of 16, and various functional groups such as phenyl, branched, and long alkyl chain. The total number of *A*-site cations investigated is 15, as shown in Figure 3-2, but we explore both iodine and bromine as the *X*-anions, totaling 21 different capping layer materials. The 15 *A*-site cations are chosen due to their availability from the perovskite precursor manufacturers, which provide large *A*-site cations to ensure Goldschmidt's tolerance factor larger than 1.00 and form LD perovskite.

As previously mentioned, the absorber is uniform across the project, which is methylammonium lead iodide ($MAPbI_3$, $CH_3NH_3PbI_3$). This specific absorber is chosen because despite its high efficiency, it is well-known to be environmentally unstable

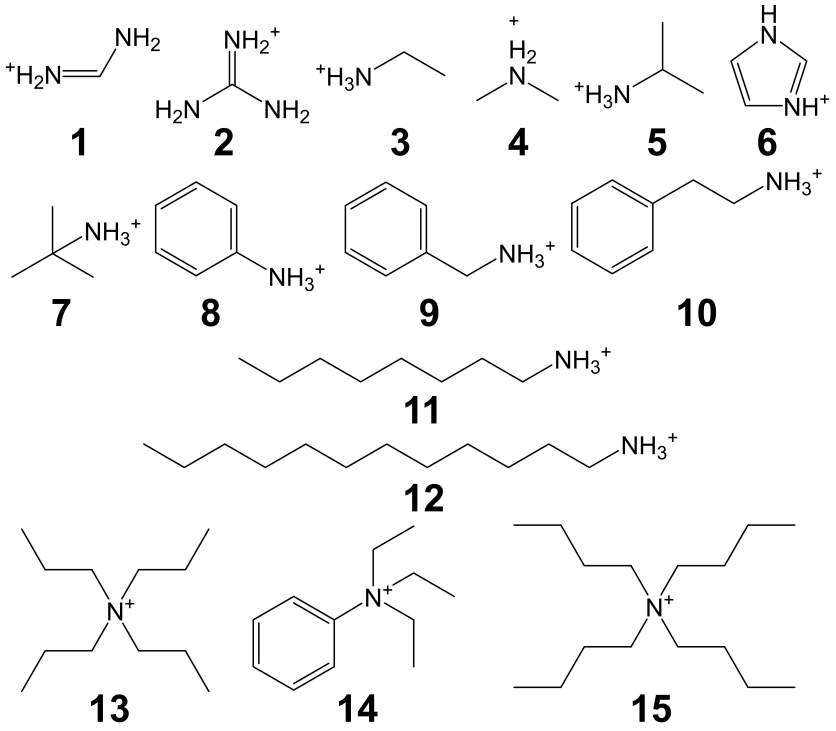

Figure 3-2: The *A*-site cations explored for capping layer material.

The 15 *A*-site cations are 1. formamidinium (FA), 2. guanidinium (GA), 3. ethylammonium (EA), 4. dimethylammonium (DMA), 5. *iso*-propylammonium (iPA), 6. imidazolium (ID), 7. *t*-butylammonium (tBA), 8. phenylammonium (PhA), 9. benzylammonium (BzA), 10. phenethylammonium (PEA), 11. *n*-octylammonium (OA), 12. dodcylammonium (DA), 13. tetrapropylammonium (TPA), 14. phenyltriethylammonium (PTEA), and 15. tetrabutylammonium (TBA).

in the presence of water, oxygen, and air [17, 88]. Improving its stability is therefore essential. In addition, the fast degradation of $MAPbI_3$ also allows us to collect more data per time for each capping layer materials and each processing condition.

The solvent used for the capping layer is isopropyl alcohol (IPA) / 2-propanol because it is commonly used for this layer [42]. Other solvents have also been explored, such as chloroform, especially because IPA dissolves formamidinium iodide (FAI) readily [149]. The solvent used for the absorber, on the other hand, uses a mixture of N,N-dimethylformamide (DMF) with dimethyl sulfoxide (DMSO) in a 9:1 ratio. This specific ratio is used after careful optimization with the absorber material to ensure superior morphology and best uniformity.

2 key things need to be satisfied for this absorber-capping layer system.

1. The absorber needs to have an excess of PbI_2, as a source of BX_2 molecules for the AX ammonium halide capping layer salts, which allows LD perovskite to be formed at the surface. Therefore, there is no need to make the complete LD perovskite precursor solution; it is sufficient to only dissolve the AX salt as the precursor for the capping layer.

2. The solvent for the capping layer needs to be only slightly soluble on the surface of the perovskite absorber to allow the reaction between excess PbI_2 coming from the absorber, with the AX salts from the capping layer material. Too much absorber solubility in the capping layer solvent will dissolve the absorber layer, while the opposite will not allow the LD perovskite to form. We are looking for the solvent 'in the middle', and IPA can act as one.

The capping layer precursor solution's common density ranges from 1-10 milligram/milliliter (mg/mL) [42, 24], finding the right concentration is critical. Researchers have also previously annealed the capped films at different temperatures, varying between 75-150 °C [134, 42, 24]. For that reason, we purposely incorporate the processing condition variables into the design of the experiment, which simultaneously increases the data points generated from the measurement. The films are therefore fabricated under 4 different annealing temperatures (50, 75, 100, and 125

°C) and 3 different concentrations (5, 10, and 15 mM), totaling to 12 different processing conditions, as previously mentioned.

3.3.2 Degradation data acquisition

After the films are deposited, the first screening step tests the materials against the elevated temperature and humidity conditions. The rationale behind this decision, as opposed to doing other types of characterizations first, is that the degradation test gives us more insight and data per unit time. The goal is to find the top material from this degradation test, which will be characterized further to understand why it exhibits such outstanding property in subsequent steps.

According to the aforementioned Equation 1.4, $MAPbI_3$ or $CH_3NH_3PbI_3$, in the presence of water, degrades into two products, including PbI_2. While $MAPbI_3$ has a dark color, PbI_2 has a visible bright yellow color. The same degradation pathway is expected in this thesis part due to the high humidity present in the chamber. The degradation of $MAPbI_3$ under high-humidity and room-temperature conditions can be seen in Figure 3-3.

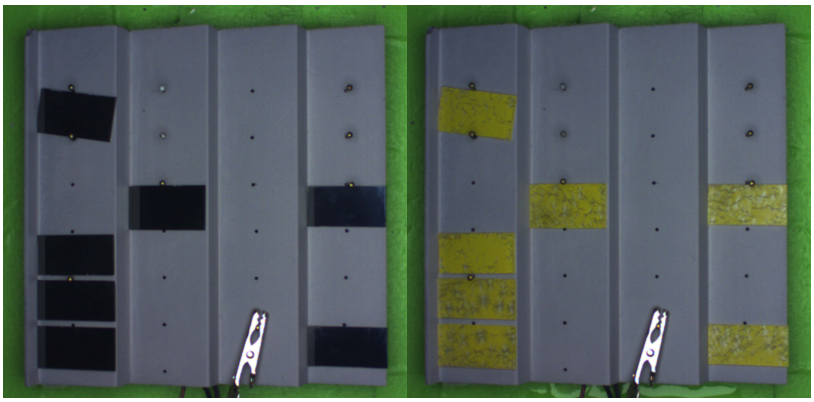

Figure 3-3: $MAPbI_3$ degradation comparison at 0 and 125 minutes, under high humidity and room temperature.

Left, right: 0 and 125 minute-degraded $MAPbI_3$ samples.

During the degradation test, film images are captured every 3 minutes for around 1,000 minutes (16+ hours). Such fast degradation is attributed to the unstable nature of $MAPbI_3$, in comparison to other lead-halide perovskites, such as $FAPbI_3$ [119].

This degradation duration in 85%RH, 85 °C, and 0.16-sun conditions is sufficient to capture the change in films color. The USB CMOS camera is sufficient to capture degradation of the samples because the PbI_2-based films degrade into specific products with different colors, which is visible to the naked eye. After all the film images are collected in JPEG format, the calibration process to transform the images into average red, green, blue (RGB) colors at each time point for specific film is done using Python. The output file is in CSV, which is ready for being used in training the machine learning models. The average color change for various capping layers is shown in Figure 3-4. Most of the capped films extend the stability of bare $MAPbI_3$ films, however, PTEAI capping layer extended the stability the most (4 ± 2 and 1.3 ± 0.3 times over bare film and state-of-the-art OABr [149], respectively).

3.3.3 Machine learning training on a dataset

Generally, the machine learning (ML) model training can simply be described as finding the model that relates the input (X) with the output (y). The input consists of the data that we already have, or the 'knowns', and the output is the outcome that we would like to predict for the future dataset, or the 'unknowns'. Training the models involves tweaking the model parameters until it reaches reasonably low RMSE (root mean squared error) without overfitting. Overfitting will cause a model to fail in predicting other sets of input, and several precautionary steps in avoiding overfitting are taken in this project. Various machine learning algorithms have been described in Section 1.3.

Input for ML models

In this project, the input will be the known variables: processing conditions and capping layer material properties from the PubChem 2019 database [62]. 12 different processing conditions for the capping layer deposition are introduced: 4 annealing temperatures and 3 precursor solution concentrations. 12 material properties are included for training the models from the database: molecular weight, x log P (or

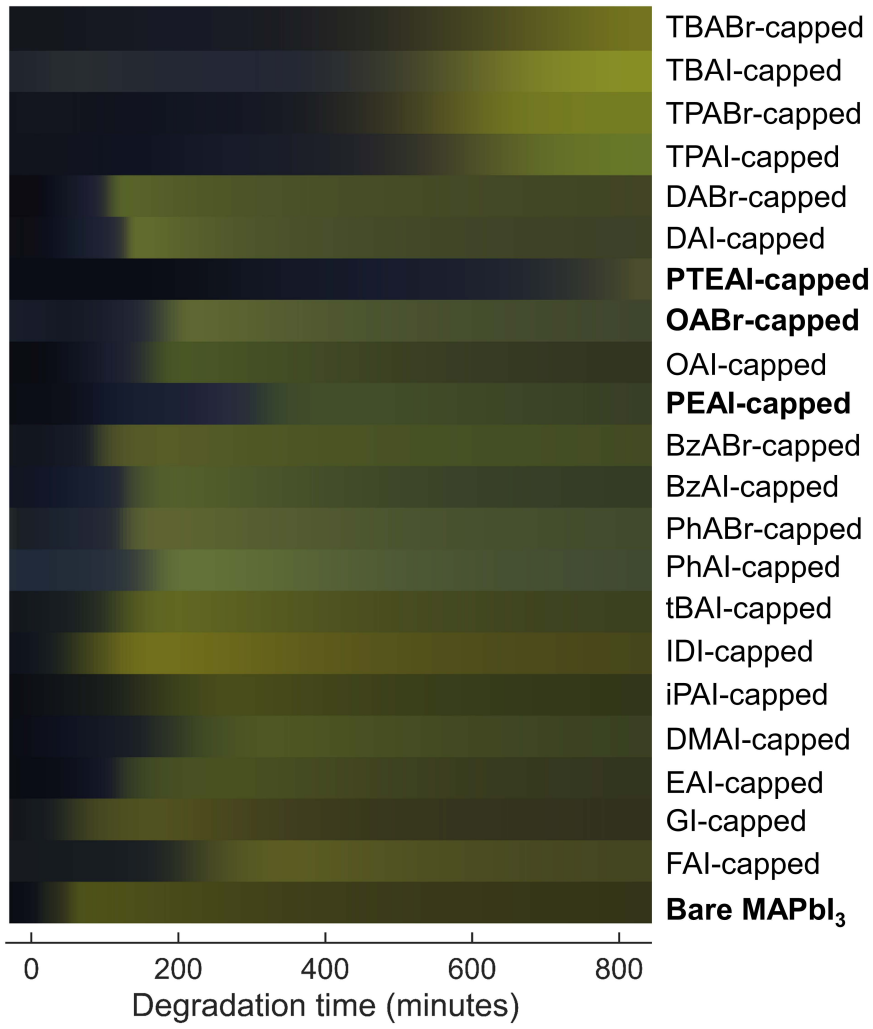

Figure 3-4: The average color change for bare and capped films.

The color change is extracted from averaging the RGB values for each of the films fabricated at optimum condition that gives maximum onset: formamidinium iodide (FAI), guanidinium iodide (GI), ethylammonium iodide (EAI), dimethylammonium iodide (DMAI), iso-propylammonium iodide (iPAI), imidazolium iodide (IDI), tert-butylammonium iodide (tBAI), phenylammonium iodide (PhAI), phenylammonium bromide (PhABr), benzylammonium iodide (BzAI), benzylammonium bromide (BzABr), phenylethylammonium iodide (PEAI), *n*-octylammonium iodide (OAI), n-octylammonium bromide (OABr), phenyltriethylammonium iodide (PTEAI), dodecylammonium iodide (DAI), dodecylammonium bromide (DABr), tetrapropylammonium iodide (TPAI), tetrapropylammonium bromide (TPABr), tetrabutylammonium iodide (TBAI), and tetrabutylammonium bromide (TBABr). The figure is adapted from Hartono, et al., "How machine learning can help select capping layers to suppress perovskite degradation", Nature Communications, 2020 [48] under CC-BY 4.0.

partition coefficient, indicating hydrophobicity or hydrophilicity of the molecules), topological polar surface area (TPSA), complexity, the number of rotatable bonds, the number of heavy atoms, the number of hydrogen-bond donors, and the number of each element (carbon, hydrogen, bromine, nitrogen, and iodine).

Output for ML models

The output of ML models is how fast each material degrades under elevated temperature and humidity conditions. Hence, the average RGB values can be used as a parameter to describe how fast the degradation happens. Since the films degrade to yellow color, the red and green (RG) values increase over time, while the blue values stay relatively the same. Because red and green value change over time overlaps, either one is sufficient to describe the film's degradation, as shown in Figure 3-5a.

For this project, we use red color as the degradation parameter. We observe that the film color stays dark until turning yellow abruptly, which is indicated by a sudden increase in red color. To characterize such abrupt change, we can either look at the red onset or the red slope, as shown in Figure 3-5b. The red onset is the time-intercept of the fitted line of the most significant change in red color, while the red slope is the slope of the same fitted line. The equation describing the degradation onset is shown on Equation 3.1, where A is the red slope, t is the time, and R is the calibrated red channel curve. The red onset is, therefore, the time-intercept of the equation, or $-\frac{B}{A}$. However, since the time point where the film starts to yellow is more appropriate for comparing the films, this project focuses on the onset instead of the slope. Henceforth, the ML models' output is the red onset, which will be called degradation onset interchangeably, of each sample.

$$y = At + B, A = \left(\frac{\mathrm{d}R}{\mathrm{d}t}\right)_{max} \tag{3.1}$$

The red onset distribution for five different capping layer material groups: carbon atom < 5, carbon atom ≥ 5 and long-chain, phenyl-based, branched, and no capping/bare films, is shown in Figure 3-6. Generally, the phenyl-based and branched

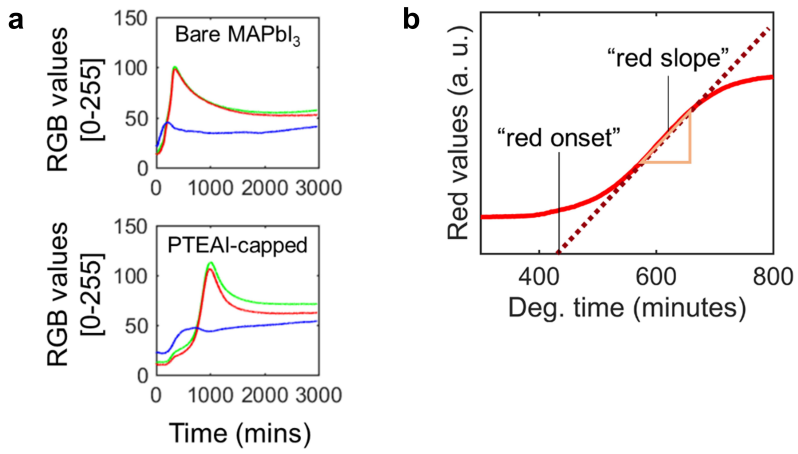

Figure 3-5: Example of RGB values for capped and bare films, and their red onset extraction.

The RGB values for bare and PTEAI-capped $MAPbI_3$ films (a) and the red onset and the red onset example for TBAI-capped film (b). The figure is adapted from Hartono, et al., "How machine learning can help select capping layers to suppress perovskite degradation", Nature Communications, 2020 [48] under CC-BY 4.0.

groups are promising and show better stability than the bare films.

Training ML models

After collecting the data for both input (X) and output (y) of the machine learning models, the next part is selecting the model that works with the data. Since the goal predicts the future set of capping layer materials, the output, i.e., the degradation onset, is continuous and not discrete. Therefore, the supervised machine learning algorithm, specifically the regression model, is the most appropriate model for training. The classification models are not suitable for the current dataset because the output is not discrete.

Using scikit-learn package in Python [101], several regression models are trained: linear regression (LR), K-nearest neighbors (KNN) regression [2], random forest (RF) regression [50], gradient boosting (GB) regression with decision trees [38], support vector machine regression (SVR) [22], and multilayer perceptron neural network (NN) with three hidden layers (each has 128, 256, and 64 units) using Adam solver [63]. The data is pre-processed, the hyperparameters are tuned using GridSearchCV in

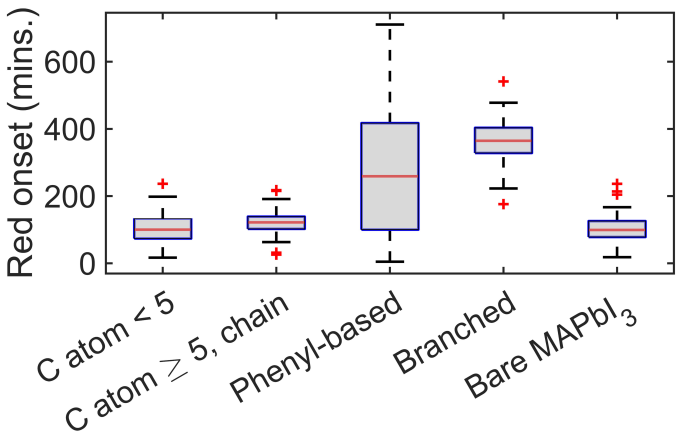

Figure 3-6: The red onset distribution for different capping layer groups.

There are five different capping layer material groups based on their *A*-site cations: carbon atom < 5, carbon atom ≥ 5 and long-chain, phenyl-based, branched, and no capping/bare films. The figure is adapted from Hartono, et al., "How machine learning can help select capping layers to suppress perovskite degradation", Nature Communications, 2020 [48] under CC-BY 4.0.

scikit-learn, and the model training is 5-fold cross-validated. The results are shown in Table 3.2. The lowest cross-validated RMSE for non-normalized input is random forest regression (104.8 minutes).

The graphs showing the comparison between non-normalized and normalized input are shown in Figure 3-7. Generally, the tree-based algorithms perform better than other models: 104 and 112 minutes for random forest regression and gradient boosting algorithms. It is still considerably high, especially when comparing it with the degradation onset range of 0-700 minutes. One of the reasons for high RMSE is that the high variability of general $MAPbI_3$ films [135]. In this study, the standard deviation of the degradation onset of bare $MAPbI_3$ films is around 45 minutes.

The comparison between degradation onset observation and prediction results of linear regression and random forest regression is shown in Figure 3-8, which shows the 80%:20% train: test split and the minimum overfitting. This figure also shows how the random forest regression prediction is better than the linear regression one.

However, this project uses the capping layer materials, which are commonly used and relatively small, using the random forest regression model to extrapolate and predict the degradation onset of much larger or entirely different *A*-site cation molecules

Regression algorithms	Hyperparameters in scikit-learn	Train RMSE (minutes)	Test RMSE (minutes)	Cross-validated RMSE (minutes)
Linear		61.8	84.0	164.3
K-nearest neighbor	algorithm: ball tree, neighbors: 3, weights: uniform	46.4	91.2	148.3
Random forest	maximum depth: 4, estimators: 60	46.5	70.8	104.8
Gradient boosting	maximum depth: 4, estimators: 30	41.7	78.5	112.3
Neural network (multilayer perceptron)	hidden layer sizes: 128, 256, 64, maximum iteration: 10000, learning rate: constant, solver: adam, alpha: 0.1, activation: relu	44.5	89.2	132.4
Support vector machine	C: 1000.0	41.3	142	169.0

Table 3.2: The machine learning algorithms, their optimized hyperparameters, and cross-validated RMSE for non-normalized input.

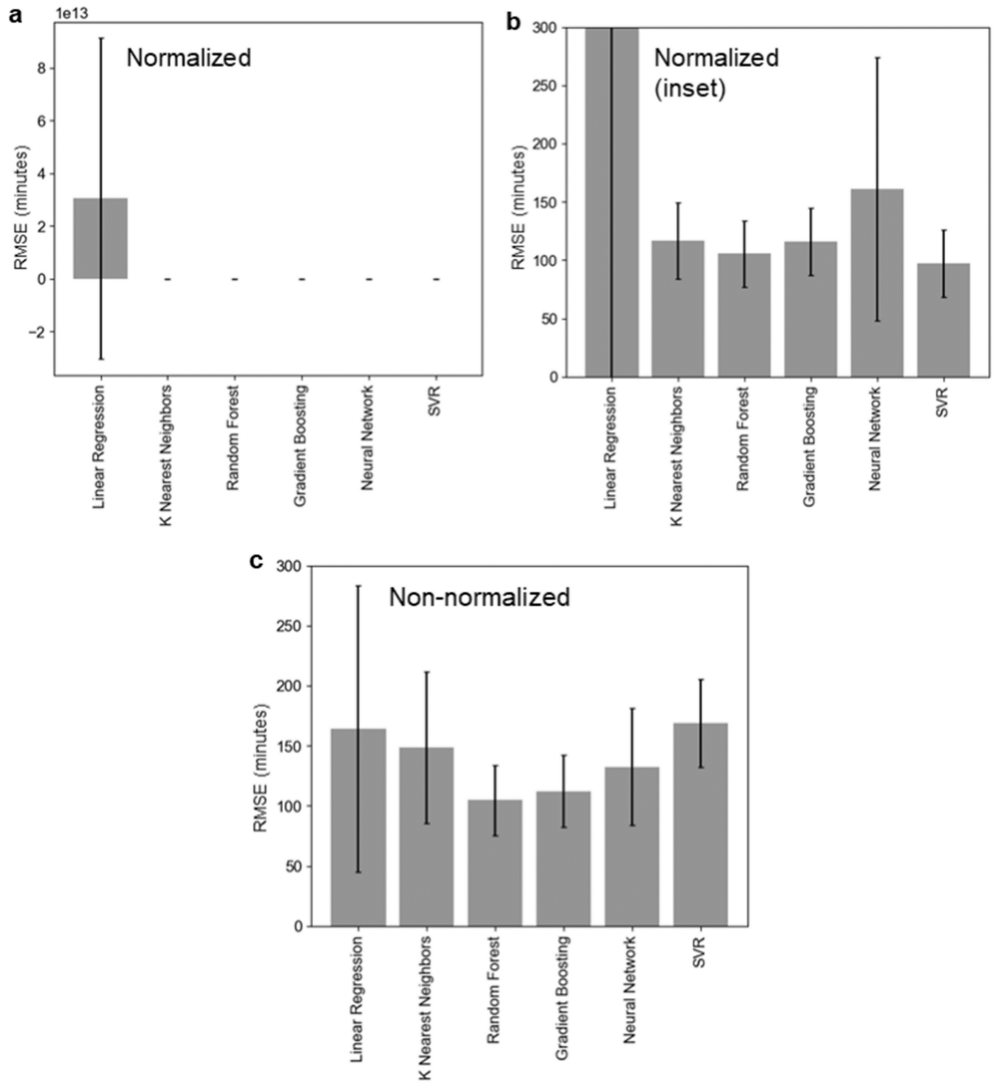

Figure 3-7: Cross-validated RMSE across different models for normalized and non-normalized input.

The figure is adapted from Hartono, et al., "How machine learning can help select capping layers to suppress perovskite degradation", Nature Communications, 2020 [48] under CC-BY 4.0.

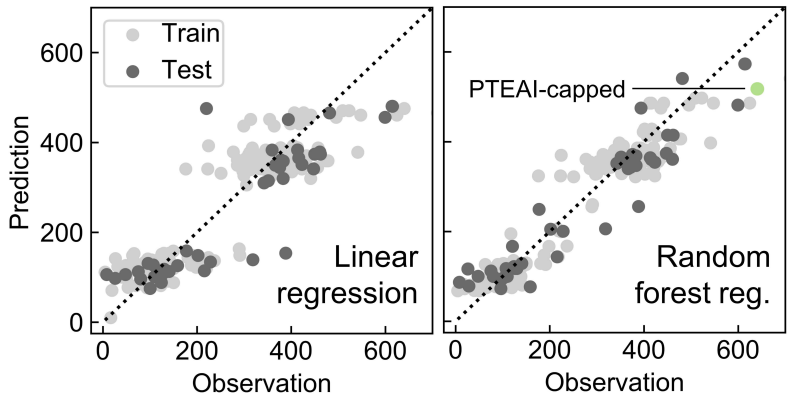

Figure 3-8: The comparison between observation and prediction of linear regression and random forest regression.

The figure is adapted from Hartono, et al., "How machine learning can help select capping layers to suppress perovskite degradation", Nature Communications, 2020 [48] under CC-BY 4.0.

should be done cautiously.

3.3.4 Interpreting trained model using Shapley value

After training the regression models with the dataset and obtaining the best model with optimized hyperparameters, we can use another toolset to interpret the model and derive an insight from it, SHAP (Shapley Additive exPlanations) [80]. We can see the feature importance rank that shows how each feature/input variable affects the model's output.

The SHAP analysis for the random forest model that predicts red onset is shown in Figure 3-9. Each point on the SHAP analysis figure comes from the observed dataset. The x-axis shows the SHAP value, which corresponds to the degradation onset. A positive SHAP value indicates higher degradation onset/more stable film and vice versa. The yellow and purple data points indicate high and low feature values, respectively. The total of 14 different input variables/features are ranked, on the left side, with the most important one at the top. Based on this result, the topological polar surface area (TPSA) comes out as the top, followed by the number of hydrogen-bond donors and molecular weight. The first two actually give

a clear result: to improve the stability, we need to pick the capping layers with the smallest TPSA and lowest number of hydrogen-bond donors. TPSA and hydrogen-bond donors are correlated (Pearson correlation coefficient of these two features is 0.81, as shown in Figure 3-10). The hydrogen-bond donor presents in a bond between hydrogen and electronegative atoms (such as nitrogen), creating a more polar surface area on the molecule. This evidence might support the previous findings on how hydrogen bonding plays an important role in PSC degradation [124, 102, 159, 89, 92], especially under high-humidity testing conditions such as the one in this study. The next features in the rank are molecular weight, which indicates that capping layer materials with higher molecular weights could also improve the stability to a certain extent. The top rank of SHAP results is robust against different models, such as GB with non-normalized dataset and SVR with the normalized dataset (Figure 3-11).

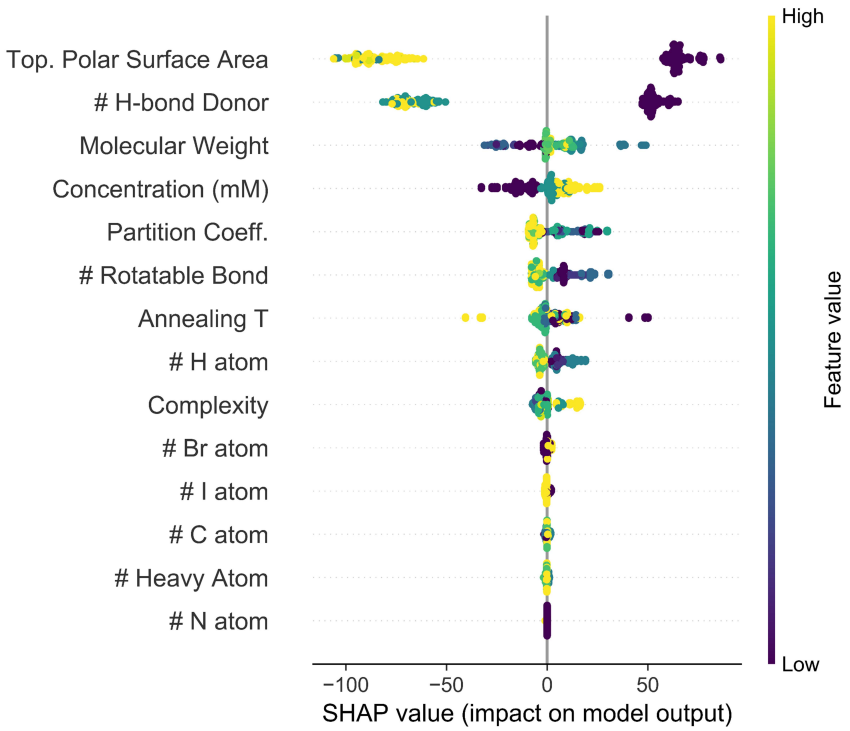

Figure 3-9: The SHAP analysis for non-normalized random forest regression model. The figure is adapted from Hartono, et al., "How machine learning can help select capping layers to suppress perovskite degradation", Nature Communications, 2020 [48] under CC-BY 4.0.

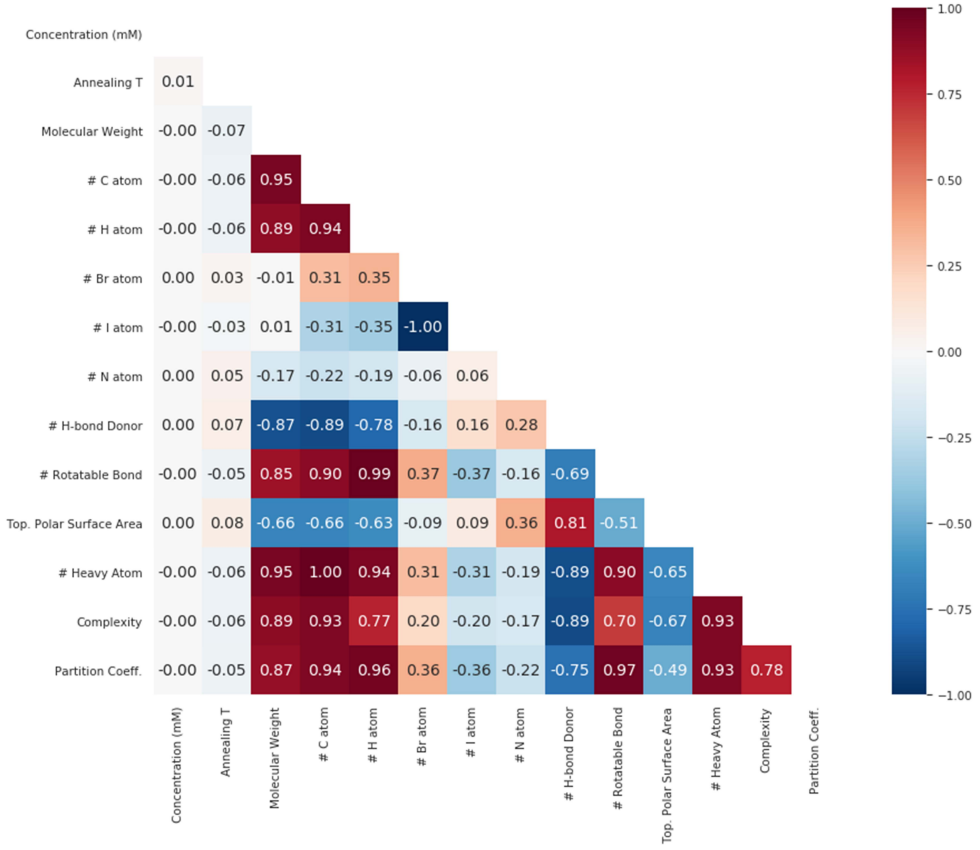

Figure 3-10: The Pearson correlation coefficients across different features.

The figure is adapted from Hartono, et al., "How machine learning can help select capping layers to suppress perovskite degradation", Nature Communications, 2020 [48] under CC-BY 4.0.

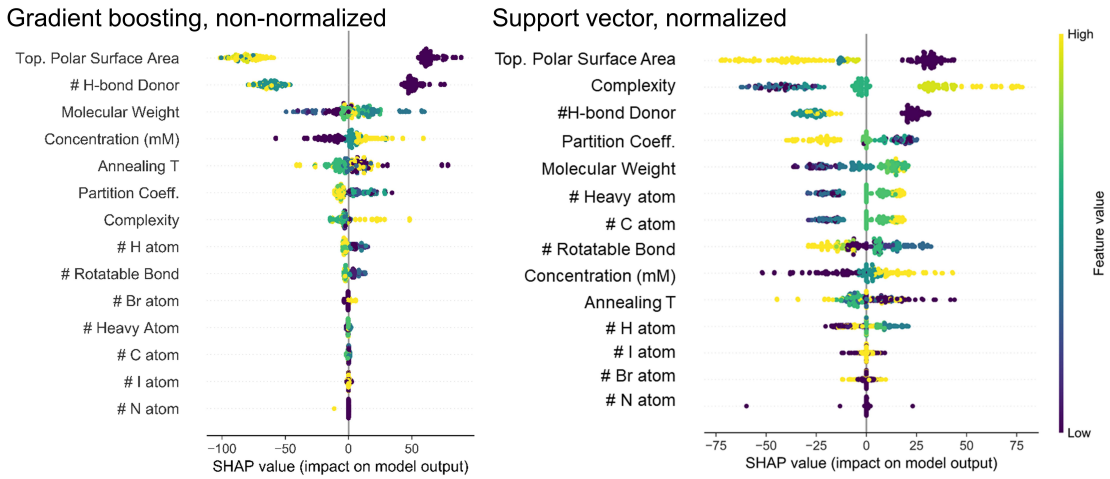

Figure 3-11: The SHAP analysis for non-normalized gradient boosting with decision trees (GB, left) and normalized support vector machine regression (SVR, right).

The figure is adapted from Hartono, et al., "How machine learning can help select capping layers to suppress perovskite degradation", Nature Communications, 2020 [48] under CC-BY 4.0.

The capping layer material that improves stability the most, PTEAI, has zero hydrogen-bond donors and has 0 $Å^2$ TPSA. Indeed, this combination is predicted to improve the stability the most, based on the SHAP analysis. Comparing to the published capping layer materials such as theophylline, caffeine, and theobromine [141], if they were fabricated and degraded in the same manner as the materials in this study, the onsets are predicted to happen at 103.2, 264.2, and 121.5, respectively, lower than the PTEAI onset at (462±115) minutes. Based on the finding in this study where quaternary ammonium group (NR_4^+, R is an alkyl or an aryl group) leads to improved stability, in future studies, it is worth exploring more complex, higher molecular weight capping layer materials with such group.

3.4 Stable capping material characterization

To probe why certain capping layer materials perform better than the other, several characterizations are conducted to observe the change in the crystal structure, morphology, organic *A*-site cation, and surface chemical composition. The measurement

is done to confirm that the findings in degradation data and see why PTEAI performs the best as a capping layer in this study. For this part of the study, in general, three different samples are being measured: bare, TPAI-capped, and PTEAI-capped $MAPbI_3$ films. The bare film serves as a control and benchmark during the measurement, in contrast the TPAI-capped and PTEAI-capped films represent the fairly good and the best stability performance across different materials. Both TPAI and PTEAI also have the same number of carbons, 12, which warrants further investigation because their sizes and molecular weights are similar.

3.4.1 Surface versus bulk crystal structure

First, we check the crystal structures of the three samples using powder X-ray diffraction (PXRD). We use Rigaku SmartLab tool for the measurement, with Cu-Kα sources. The 2θ-scan results for bare, TPAI-capped, and PTEAI-capped $MAPbI_3$ films at 0, 460, and 640 minutes of degradation is shown in Figure 3-12. The purple shade on the figure indicates the (110) phase of $MAPbI_3$ based on the PXRD pattern with ICSD collection code 250735 [128], and the yellow shade indicates the PbI_2 phase based on ICSD collection code 68819 [98].

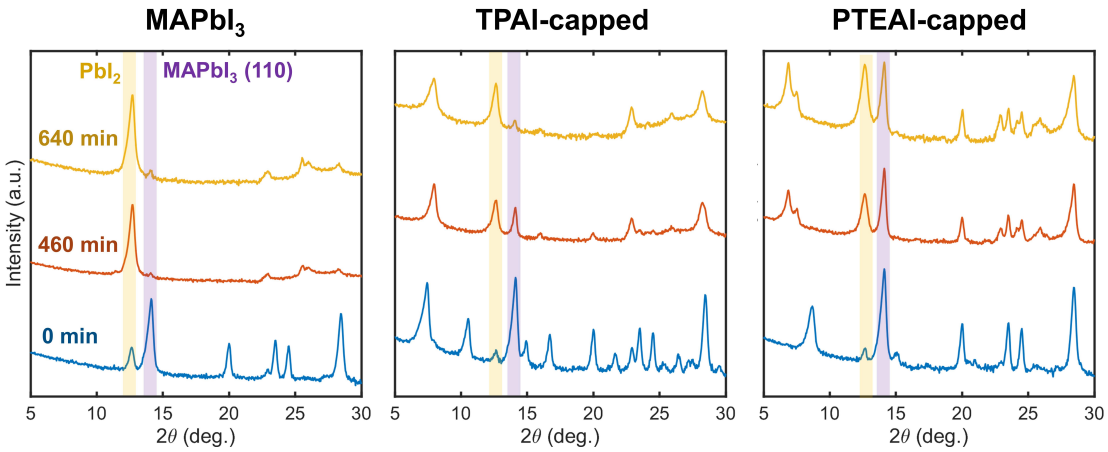

Figure 3-12: The XRD comparison between bare, TPAI-capped, and PTEAI capped $MAPbI_3$ films at different time points of degradation.

The figure is adapted from Hartono, et al., "How machine learning can help select capping layers to suppress perovskite degradation", Nature Communications, 2020 [48] under CC-BY 4.0.

In bare $MAPbI_3$ film, the $MAPbI_3$ (110) phase has become PbI_2 phase after 460 minutes of high-humidity and high-temperature degradation. On the other hand, both TPAI-capped and PTEAI-capped films still preserve the $MAPbI_3$ (110) peak after 460 minutes. In the case of PTEAI-capped film, it even retains the (110) phase after 640 minutes, even though the TPAI-capped already degraded. This serves as evidence that PTEAI indeed improves stability the most. Additionally, looking at the low angle peaks ($< 10°$), both TPAI-capped and PTEAI-capped films show extra peaks that do not present at bare $MAPbI_3$ film, indicating the LD perovskite peaks presence, which helps to improve the stability of the films.

Looking at the low-angle peaks in PTEAI-capped films specifically, one interesting thing happens. The 2θ angle for the LD perovskite peaks for fresh sample (0 minutes) and during degradation (460 and 640 minutes), the peaks location shift, which might indicate that as PTEAI-capped $MAPbI_3$ film degrades, one type of LD perovskite that is initially formed changes, and becomes another LD perovskite phase.

However, PXRD data does not show whether certain phase dominates the bulk versus the surface, which is important to investigate in the capping layer. We, therefore, measure the grazing incidence wide-angle X-ray scattering (GIWAXS) in 11-BM beamline at NSLS-II, Brookhaven National Laboratory. At a different θ angle, GIWAXS probes different thicknesses of the films as shown in Figure 3-13. We use 13.5 keV X-ray beam energy. The scattering spectra are collected with an exposure time of 30 seconds by an area detector, DECTRIS Pilatus 8008, located 257 mm away from the sample. The result is shown in q-space, where q_r and q_z indicate horizontal and vertical axes. In this case, when $\theta = 0.12°$, it probes the surface, while at $\theta = 0.2°$, it mostly probes a deeper thickness of the film and shows the bulk profile. The green arrow indicates the $MAPbI_3$ phase, while the white arrow shows the LD perovskite phase. Looking at specifically the TPAI-capped and PTEAI-capped results, the signal of $MAPbI_3$ is stronger at the bulk, in comparison, the LD perovskite signal is stronger at the surface, confirming that the stratification of absorber and capping layers are as expected.

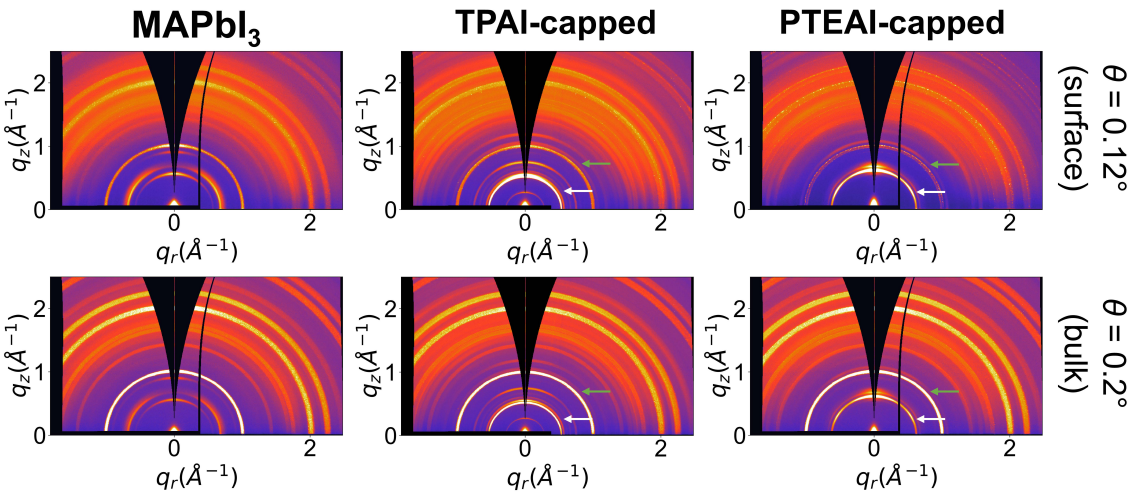

Figure 3-13: The GIWAXS comparison between bare, TPAI-capped, and PTEAI capped $MAPbI_3$ films at surface and bulk.

The green arrow indicates the $MAPbI_3$ (110) phase, while the white arrow indicates the PbI_2 phase. The figure is adapted from Hartono, et al., "How machine learning can help select capping layers to suppress perovskite degradation", Nature Communications, 2020 [48] under CC-BY 4.0.

3.4.2 Surface morphology change

After looking at how the crystal structure changes within the film, it is also important to observe how the surface morphology changes using a ZEISS Ultra-55 field-emission scanning electron microscope (FESEM). Various bare, TPAI-capped, and PTEAI-capped films at different degradation time points: 0, 460, and 640 minutes, are measured using the FESEM. The result is shown in Figure 3-14, and the scale bar is 200 nm. In the fresh samples, the large grain boundaries, which can be clearly observed in bare $MAPbI_3$ are no longer visible in TPAI-capped and PTEAI-capped films, indicating that the surface of the films is coated with LD perovskites based on the previous crystal structure investigation. However, there is no clear trend with the surface morphology of films degraded at 460 and 640 minutes, though it is clear that pinholes start to form when films are degrading.

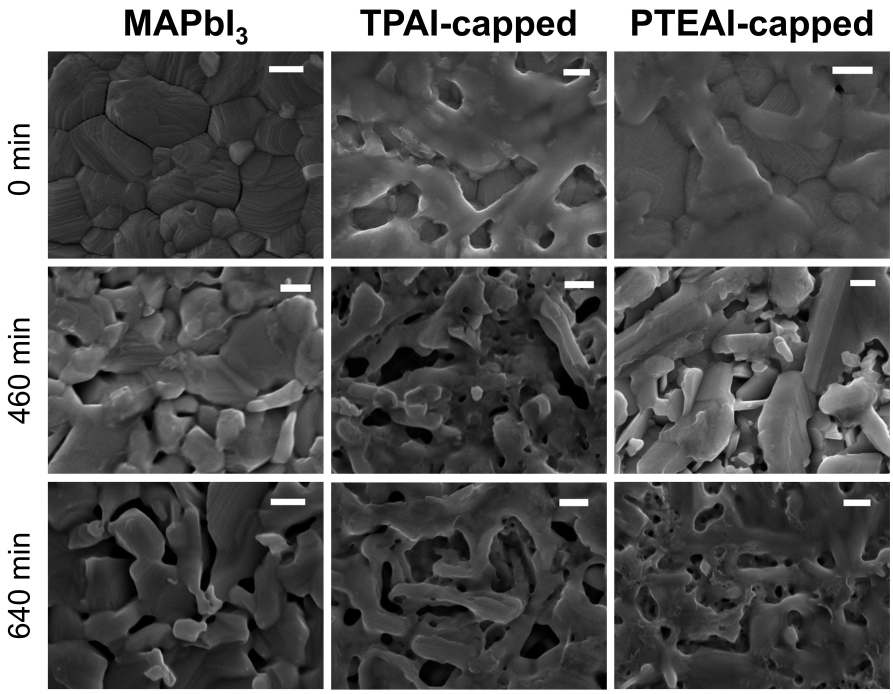

Figure 3-14: The SEM comparison between bare, TPAI-capped, and PTEAI capped $MAPbI_3$ films at different degradation time points.

The scale bar is 200 nm. The figure is adapted from Hartono, et al., "How machine learning can help select capping layers to suppress perovskite degradation", Nature Communications, 2020 [48] under CC-BY 4.0.

3.4.3 Organic *A*-site cation change

To probe how the organic *A*-site cations of capping layers at the surface change over time, Fourier-transform infrared spectroscopy (FTIR) is conducted using Perkin-Elmer Spectrum 400 tool. The comparison of FTIR spectroscopy results in attenuated total reflection (ATR) geometry with ZnSe crystal for bare, TPAI-capped, and PTEAI-capped $MAPbI_3$ films at different degradation time points: 0, 460, and 640 minutes, are shown in Figure 3-15.

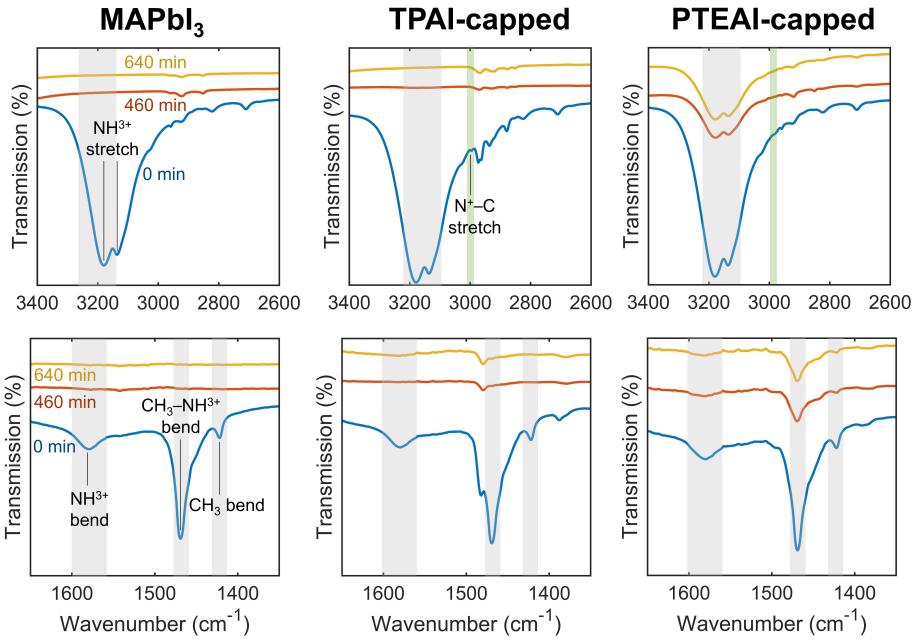

Figure 3-15: The FTIR comparison between bare, TPAI-capped, and PTEAI capped $MAPbI_3$ films at different degradation time points.

The figure is adapted from Hartono, et al., "How machine learning can help select capping layers to suppress perovskite degradation", Nature Communications, 2020 [48] under CC-BY 4.0.

The NH_3^+ stretch signal at 3176 cm^{-1} coming only from methylammonium (MA) because it does not exist in tetrapropylammonium (TPA) or phenyltriethylammonium (PTEA), therefore serves as the MA indicator from the absorber. In this case, it is clear that even at 460 minutes, the NH_3^+ stretch has disappeared in bare and TPAI-capped $MAPbI_3$ films on the surface. However, we know that based on GIWAXS and XRD results, at 460 minutes, the TPAI-capped film still has $MAPbI_3$ left within

the bulk. This indicates that at this time point (460 minutes), the $MAPbI_3$ at the surface of TPAI-capped has degraded, even though some of it is left within the bulk. On the other hand, the MA in PTEAI-capped $MAPbI_3$ film still presents even after 640 minutes, indicated by the presence of NH_3^+ stretch. Besides NH_3^+ stretch, the other bonds that can be the sign of MA presence are NH_3^+ bend and $CH_3 — NH_3^+$ bend. Both of them also show similar results as the NH_3^+ stretch.

3.4.4 Surface chemical composition change

To measure how the chemical composition changes before and during the degradation, such as how water might attach to the surface of the capping layer, X-ray photoelectron spectroscopy (XPS), specifically using Thermo Scientific K-Alpha+ XPS with Al-Kα excitation source, can help to investigate this. The XPS result is fit to C 1s, I 3d, N 1s, O 1s, and Pb 4f peaks, which allow the atomic percentages for each element to be calculated. Figure 3-16a shows the comparison of the oxygen channel (O 1s for bare and PTEAI-capped films across different degradation time points, and Figure 3-16b shows their atomic percentage.

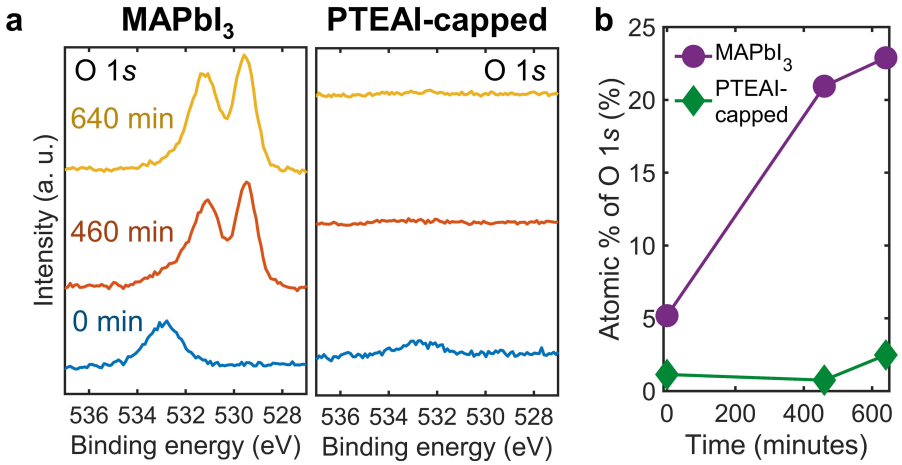

Figure 3-16: The O 1s XPS comparison between bare and PTEAI capped $MAPbI_3$ films at different degradation time points.

The figure is adapted from Hartono, et al., "How machine learning can help select capping layers to suppress perovskite degradation", Nature Communications, 2020 [48] under CC-BY 4.0.

The oxygen presence, which might come from water (H_2O), air (O_2), or PbO_x [132, 129], increases as the bare $MAPbI_3$ film degrades. However, this oxygen presence is suppressed in our most stable film, PTEAI-capped $MAPbI_3$. The atomic percentage of O $1s$ increases to around 24% at 640 minutes of degradation in the bare film, while the PTEAI-capped film stays below 1%.

3.5 Conclusion

This study presents a framework to utilize both high-throughput and more traditional approaches to investigate which capping layer material could improve stability the most for a perovskite absorber and derive the design guidelines for future study. 21 capping layer materials with $MAPbI_3$ absorber are tested under 5%RH, 85 °C, and 0.16-sun conditions. Regression models are trained to relate the capping layer molecular properties and processing conditions with the degradation onsets. SHAP analysis is then conducted on the trained models to extract the feature importance rank and see which features contribute to the improvement in stability the most: the small topological polar surface area of the organic capping layer molecule and the small number of hydrogen-bond donors. Phenyltriethylammonium iodide (PTEAI) improves the bare $MAPbI_3$ film stability by more than 4 ± 2. The crystal structure advanced characterization shows that low-dimensional perovskite is formed at the top of the capped film's surface, while SEM, FTIR, and XPS show that PTEAI capping layer modifies the surface of the film that causes the suppression in oxygen-containing compounds at the surface. The improvement in stability using the capping layer method is therefore important in pushing PSCs closer towards commercialization.

Chapter 4

Stable capping layer for mixed-halide, MA-based absorber

4.1 Motivation for tuning perovskite bandgap by changing absorber composition

Currently, the record efficiency of single-junction PSCs has gone beyond 25%, comparable to the efficiency of silicon solar cells [68]. A trend of using perovskite as a tandem cell also emerges due to its bandgap tunability [70], making it a suitable candidate material for both narrow- and wide-bandgap solar cells. The wide-bandgap PSCs have also been used for indoor PV applications, specifically for the internet of things (IoT) devices [85]. The bandgap tuning characteristic is possible by mixing different X-anions/halides within the perovskite film, as shown in Table 4.1. As we shift from iodine-based to bromine-based or even chlorine-based halide perovskites, the bandgap also gradually increases. Therefore, both high-efficiency perovskite single-junction and tandem cells benefit from mixing the perovskite absorber to improve efficiency or induce bandgap change.

However, it is known that introducing halide mixture into the perovskite absorber also causes phase segregation, creating iodine-rich and bromine-rich areas under illumination [150]. These areas will be the initiation sites for the degradation cascading

Composition	Bandgap (eV)
$MAPbI_3$	1.58
$MAPbI_{2.8}Br_{0.2}$	1.62
$MAPbI_{2.6}Br_{0.4}$	1.65
$MAPbI_{2.4}Br_{0.6}$	1.68
$MAPbI_{2.2}Br_{0.8}$	1.71
$MAPbBr_3$	2.27

Table 4.1: The bandgap of $MAPb(I_xBr_{1-x})_3$.
The bandgap is based on the photoluminescence peak at 25 °C [3].

process. The phase separation occurs with a rate constant of 0.1-0.3 s^{-1}, and the dark recovery occurs at a longer timeline, in order of minutes to an hour [150]. The fast phase separation but slow recovery process highlights the importance of considering stability while designing the perovskite absorber materials for photovoltaic applications.

In this thesis chapter, we hypothesize that the optimal capping layer material for stability changes as the film composition changes within the iodine-bromine series. We also interrogate the underlying root causes. There is no systematic study investigating how the change in bandgap due to changing halide composition affects the optimum capping layer for stability. Answering these questions will help researchers better design capping-absorber pairs for single-junction and tandem solar cells, as well as other applications including indoor and IoT devices.

4.2 Project workflow

To find the stable, high-performing capping-absorber pairs for PSCs, we design a workflow for this thesis chapter, shown in Figure 4-1. We start by fabricating films consisting of $MAPb(I_xBr_{1-x})_3$ mixed-halide absorber with 10 1D perovskite capping layer materials and PTEAI as the capping material benchmark from the previous chapter. After the samples are degraded, the data is processed and analyzed using 2 methods: dissimilarity matrix for faster analysis of high-dimensional data and SHAP analysis to extract the feature importance rank. The degradation mechanism is also

further discussed based on the results presented in this chapter.

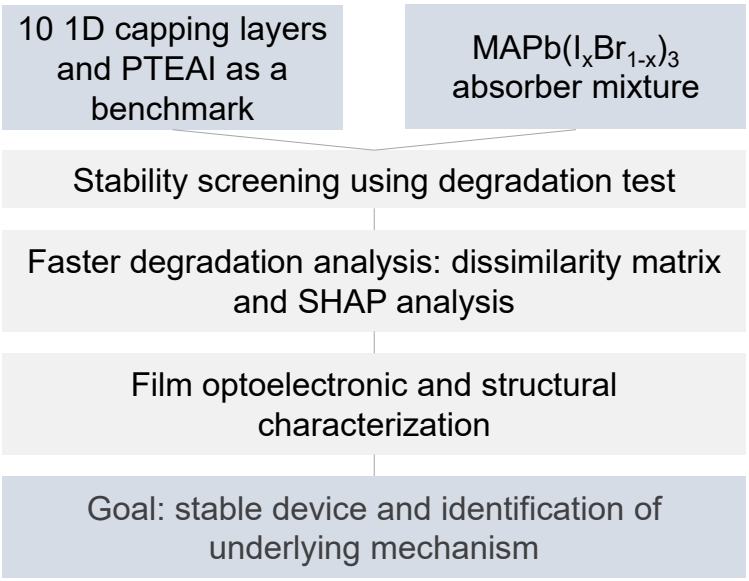

Figure 4-1: The project workflow for this thesis chapter.

4.3 Capping-absorber pair screening

4.3.1 The materials choice

We source our 1D perovskite materials from our collaborator, Marie-Hélène Tremblay (Marder Group, Georgia Institute of Technology) in powder form, making it easier to dissolve the material in solvents for deposition. There are 10 different capping layer materials, as shown in Figure 4-2, and the complete list is shown in Table 4.2. They form 1D perovskites, and they are either phenyl-, cyclohexane- or naphthyl-based *A*-site cations. PTEAI, the most stable capping layer from the previous chapter, is also included in the screening as the benchmark. Various functional groups are present in addition to amines, such as nitrile ($R-C\equiv N$), ester ($R-CO_2-R'$), methoxy ($R-O-CH_3$), nitro ($R-NO_2$), and alcohol ($R-OH$). Compared to the capping layers investigated in the previous chapter, the capping layer materials in this chapter are similar in size and have similar functional groups. Some of them, such as 3-I and

6-I, as well as 4-I and 5-Cl, actually have the same functional groups in their *A*-site cations. The only difference is one of them is ortho- (the functional groups are adjacent to each other, in positions 1 and 2), and the other is meta- (the functional groups are in positions 1 and 3). These differences could lead to an interaction change between the *A*-site cations with the $[PbX_6]^{4-}$ octahedra, and a change in material density to a difference in how closely-packed the unit cell is.

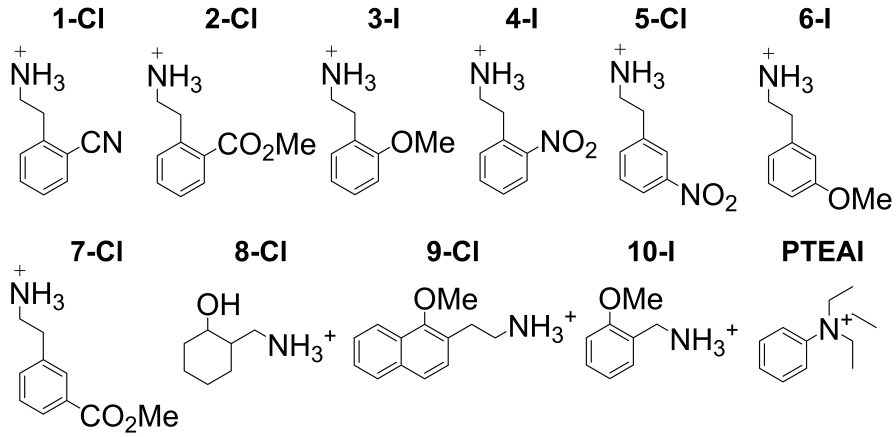

Figure 4-2: The different *A*-site cations of the capping layer materials explored in this chapter.

#	Composition name	Functional groups
1-Cl	2 CN – PEA – Cl	Phenyl, ammonium, nitrile
2-Cl	2 CO_2Me – PEA – Cl	Phenyl, ammonium, ester
3-I	2 MeO – PEA – I	Phenyl, ammonium, methoxy
4-I	2 NO_2 – PEA – I	Phenyl, ammonium, nitro
5-Cl	3 NO_2 – PEA – Cl	Phenyl, ammonium, nitro
6-I	3 MeO – PEA – I	Phenyl, ammonium, methoxy
7-Cl	3 CO_2Me – PEA – Cl	Phenyl, ammonium, ester
8-Cl	2 HO – CycMA – Cl	Cyclohexane, ammonium, alcohol
9-Cl	2 MeO – NEA – Cl	Naphthyl, ammonium, methoxy
10-I	2 MeO – PMA – I	Phenyl, ammonium, ester
PTEAI	PTEA – I	Phenyl, ammonium

Table 4.2: The functional groups making up the *A*-site cations.

4.3.2 Fast image data screening

After the capping layers are deposited atop of 25%-increment $MAPbI_3$-$MAPbBr_3$-mixed absorber at two different concentrations, 5 and 10 mM (mmol/L), and annealed at two different temperatures, 75 and 100 °C for 10 minutes, the films are aged in degradation chamber under 80%RH, 85 °C, and 0.15-sun. The images of the films are taken every 3 minutes. The same data acquisition protocol and image data analysis for extracting the average red, green, blue (RGB) values at every time point as the previous chapter are then conducted. The only difference is the image files being analyzed are BMP instead of JPEG because they have higher resolution. A total number of 420 samples is then further analyzed.

The averaged RGB color change result across different capping layer materials and absorbers is shown in 4-3. It shows two different examples of bare and PTEAI-capped films, showing the variation in degradation color change. The starting color of films also varies based on their absorber composition due to the change in the bandgap. Interestingly, in $MAPb(I_{0.75}Br_{0.25})_3$-based films, the stability is generally lower than other films, even $MAPbI_3$, regardless of capping layer type deposited.

The 9-Cl and PTEAI capping layer materials are selected to be further investigated because they outperform the other capping layer materials, especially in I-rich absorber materials. For example, in the case of $MAPbI_3$ samples, PTEAI capping can improve the bare film stability by (4 ± 2) times, while 9-Cl can improve by > 6 times. However, in the case of $MAPb(I_{0.75}Br_{0.25})_3$-based films, PTEAI capping can improve the bare film stability by > 2 times, while the 9-Cl capping can only improve it by > 1.2 times.

Unlike in the previous chapter, where the degradation from $MAPbI_3$ to PbI_2 is clear, in this alloy series, many of the films do not degrade from black to yellow, because both the bandgap of the initial film is different, and the degradation pathways and products may also be different. The fact that the data is 4-dimensional, consisting of RGB and time for each sample, also adds another layer of complication.

To look at all the data faster simultaneously, a dissimilarity matrix is suitable

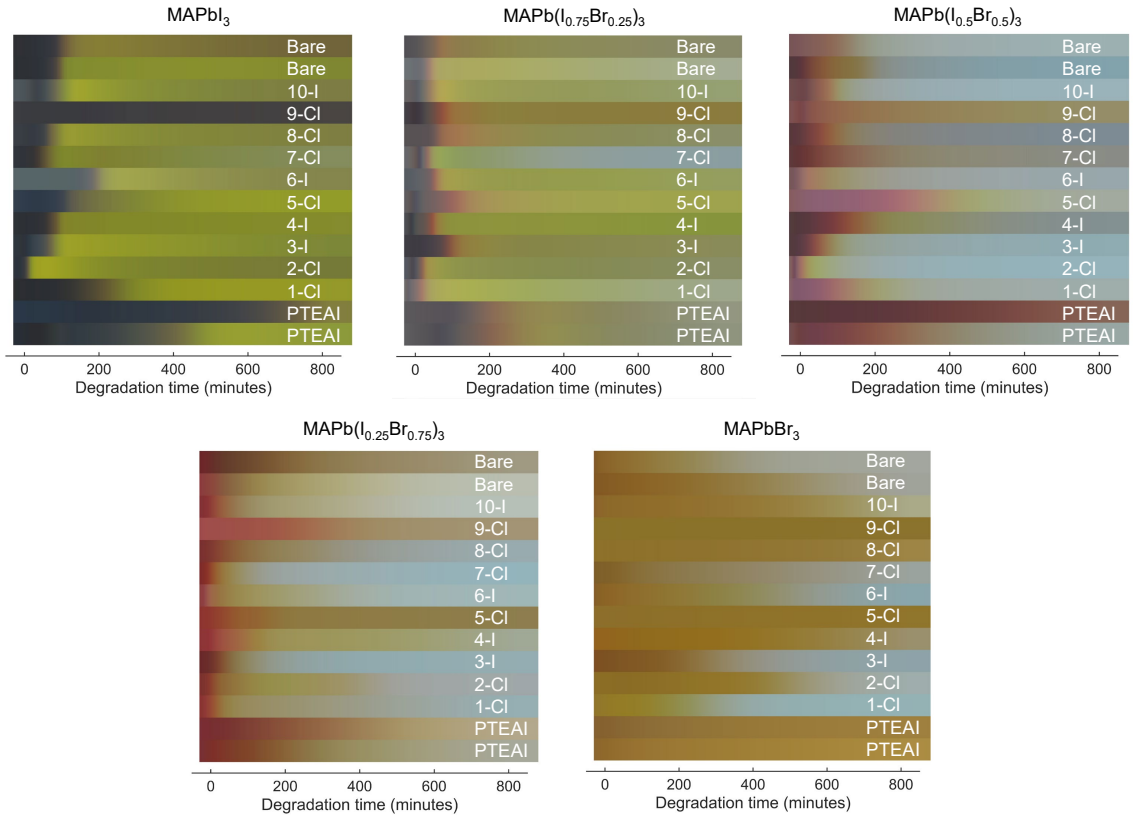

Figure 4-3: The degradation result across different capping layers and absorber compositions based on averaged RGB values.

for looking at the overview of a large, multi-dimensional dataset. The m by m matrix shows how dissimilar/ similar one sample with another. Each (a, b) matrix cell contains a value, representing how dissimilar/ similar sample a and sample b is, by calculating the distance between the 2 vectors of a and b.

Commonly used distance measures for similarity analysis are Minkowski (such as Manhattan, Euclidean), L1, inner product (such as Jaccard, cosine), squared chord, and squared L2 [108]. One of the distance measures, cosine similarity, has been widely used for various purposes, including face verification [145, 91], text classification [71], and automated essay scoring [69]. The robustness of the cosine distance measure is proven from its cross-disciplinary use for evaluating the similarity between datasets.

In this chapter, a dissimilarity matrix is used to evaluate the aforementioned 4-dimensional degradation data consisting of RGB values and time, to compare one sample from the others. The 4-dimensional data is first pre-processed and collapsed into a 1-dimensional vector before its dissimilarity value with another vector calculated by taking the distance between the two vectors. This helps to look at the pattern in the data faster. The dissimilarity matrix is constructed using a pairwise distance algorithm from scikit-learn [101], that computes the distance matrix between two vectors for each sample pair for the entire dataset. Cosine similarity is used as a metric due to its robustness and wide implementation. It calculates the L2-normalized dot product of the two vectors. The larger the distance between the two vectors is, the higher the dissimilarity matrix value is, and vice versa.

A hypothetical example of a dissimilarity matrix is shown in Figure 4-4. If we have two types of compositions, X and Y, where each of them has 2 samples, we get the 4×4 dissimilarity matrix. When the dissimilarity value is high, the color is yellow, and when it is low, the color is purple, as shown in the color bar. Two things can be compared in the dissimilarity matrix: comparison among the repeated compositions (X and X, or Y and Y) and across different compositions (X and Y). The advantage of using a dissimilarity matrix can be seen directly; regardless of the dataset size for each sample, the distance between the two vectors can be observed in one value.

This chapter focuses on the RGB values between 0 and 999 minutes for the dis-

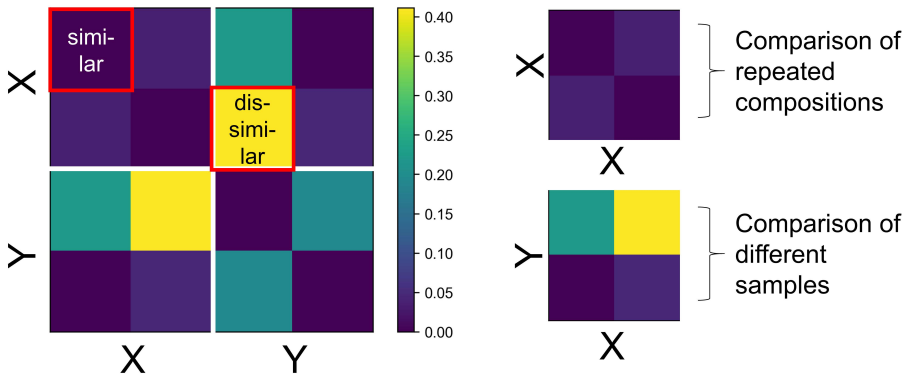

Figure 4-4: A hypotethical example of dissimilarity matrix.

similarity matrix analysis. At 999 minutes, the films with poor stability have fully degraded, while the ones with good stability can still maintain their colors. Each sample has an RGB color for each time point, and this data can be appended into one vector. The distance measure between this sample with other samples is then calculated to form the dissimilarity matrix, which shows the film color change comparison during the first 999 minutes of degradation. The dissimilarity matrix of these data using cosine distance measure is shown in Figure 4-5a.

A couple of observations can be made based on the dissimilarity matrix result, as follows.

1. The $MAPbI_3$-based films qualitatively have higher variations than the Br-containing films.

2. The difference between 9-Cl and PTEAI capping layer are the most distinct in the case of $MAPb(I_{0.75}Br_{0.25})_3$ absorber, in contrast, the two capping layer materials are indifferent in improving the stability (up to 999 minutes) for Br-rich absorbers, but especially for $MAPbBr_3$.

3. Note that the dissimilarity matrix can only tell if one sample is different from the other, but it cannot tell if one is better than the other. Therefore, it is still important to check back the color changes in the degradation results in Figure 4-3 to to verify if the change is indeed an improvement.

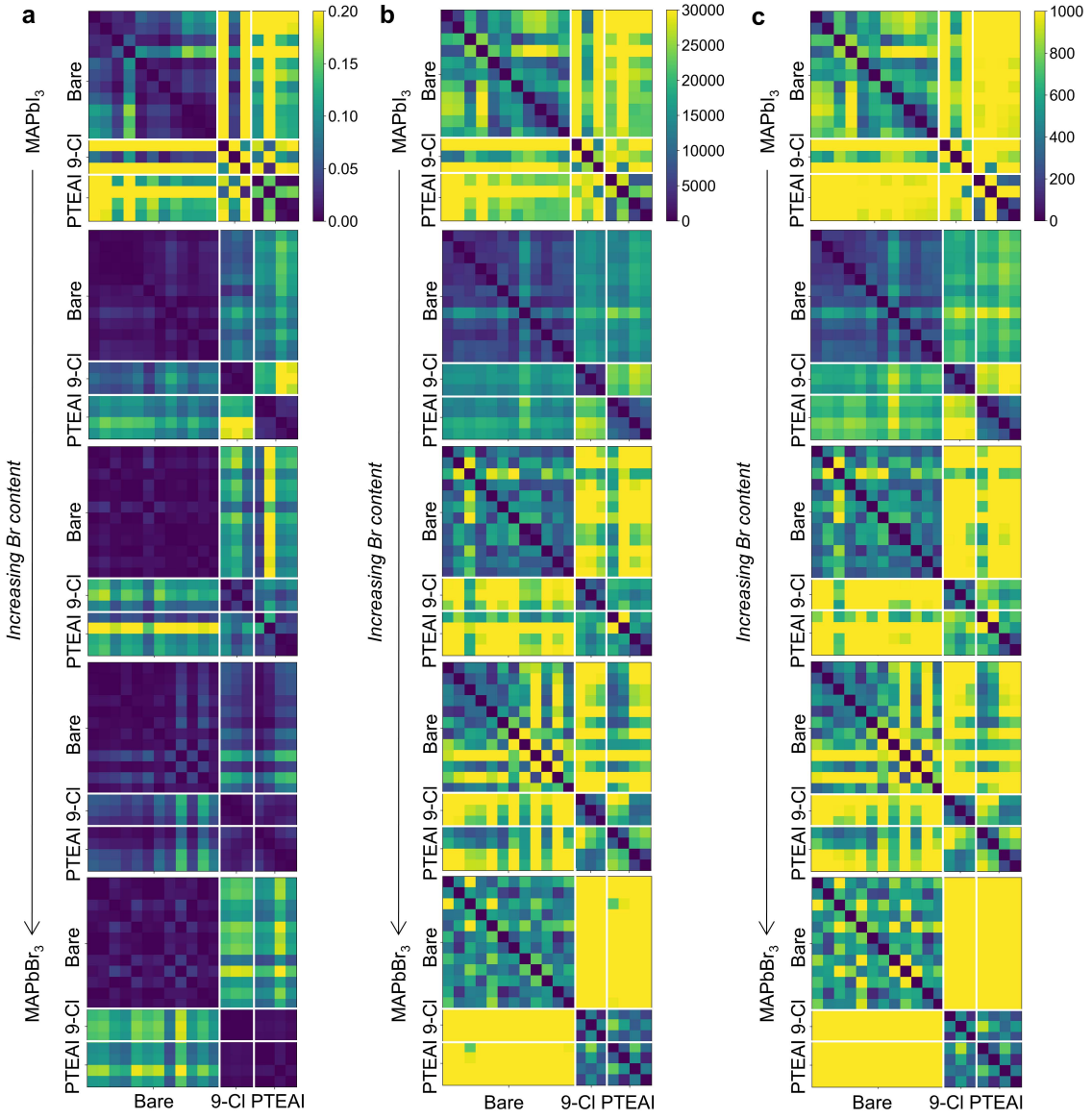

Figure 4-5: The dissimilarity matrix constructed using various distance measure of bare, 9-Cl-, and PTEAI-capped films across the $MAPbI_3$-$MAPbBr_3$ series.

The distance measures used are cosine (a), Manhattan (b), and Euclidean (c).

The result in the Figure 4-5 shows the dissimilarity matrix using a cosine distance measure. However, it is also important to check the consistency in results using other distance measures, such as Manhattan and Euclidean distance, as shown in Figure 4-5b, c. The main insights still hold across different distance measures calculated.

4.3.3 Shapley value analysis reveals the main degradation drivers

Shapley value analysis for extracting feature importance rank

Like the one conducted in the previous chapter, SHAP analysis is then performed to understand the most important capping layer features for this data set. However, we first need to train the dataset. We include 21 features as the input, including the absorber amount, processing conditions, capping layer molecular properties, and functional groups: the amount of $MAPbBr_3$, number of chlorine and iodine atoms, number of rotatable bonds, number of hydrogen-bond donors, topological index (that measures complexity), topological polar surface area, molecular weight, partition coefficient, annealing temperature, concentration, and if certain functional groups are present in the *A*-site cations, such as nitro, nitrile, benzene, naphthalene, ester, methoxy, alcohol, primary or quaternary amine. Since the capping layer materials are novel and are mostly not available in the PubChem database, the capping layer material properties are extracted from ChemDraw and ChemOffice applications (PerkinElmer), including the topological polar surface area, topological index, partition coefficient, number of rotatable bond, and number of hydrogen-bond donor. The functional groups are included in the feature list, as opposed to the number of certain atoms (carbon, hydrogen, nitrogen, oxygen, heavy atoms) because these capping layer materials have similar functional groups among each other, which could affect their stability more significantly than the presence of certain atoms.

The output to the algorithm will be a metric indicating how fast, or slow, the samples degrade. Unfortunately, the degradation onset metric that was introduced in the previous chapter can no longer be used. There are several reasons why we need to find a more suitable metric: we have different initial and final colors, the red and

green values are no longer changing simultaneously, and the blue value is not relatively constant throughout the degradation process. Instead, the differential area is used as the instability metric, which is the area difference under the RGB sum curve between the initial and final time point of interest. In this case, we are using 1,000 minutes as the cut-off time, close to the 999 minutes cut-off time for the dissimilarity matrix analysis, since most of the fast degrading films already change color, and the slow-degrading films are in the process of changing color or still retain their initial color. For this dataset, we observe the instability metric ranges between 5.6×10^3 - 3.0×10^5 minutes. The same instability metric has also been used in Bayesian optimization for finding the most stable mixed-composition between $CsPbI_3$, $MAPbI_3$, and $FAPbI_3$ [131], and using the same study's differential area extraction code [136].

After collecting both input and output for the dataset, the non-normalized dataset is then trained on different algorithms, such as linear regression, K-nearest neighbors regression, random forest regression, gradient boosting with decision trees regression, multi-layer perceptron (neural network) regression, and support vector regression (SVR). The root mean squared error (RMSE) of these algorithms are shown in Figure 4-6. For the highest instability metric, the random forest regression and gradient boosting with decision trees regression have an RMSE of 16.7% and 16.1%, respectively. Random forest regression shows one of the lowest RMSE, and the same algorithm is used for SHAP analysis to extract the feature importance rank, as shown in Figure 4-7. The positive SHAP values indicate that the instability metric is high and vice versa. Therefore, if we look at the top feature, $MAPbBr_3$ amount, as we shift from $MAPbI_3$ to $MAPbBr_3$, we start with moderate instability, go up, and end up with low instability for 100% $MAPbBr_3$.

Absorber's light-induced halide segregation as the primary degradation driver

As we previously observe in dissimilarity matrices, the amount of $MAPbBr_3$ in the absorber dominates the stability outcome. This feature comes out as the top feature in the SHAP feature importance rank. The addition of $MAPbBr_3$ into the $MAPbI_3$

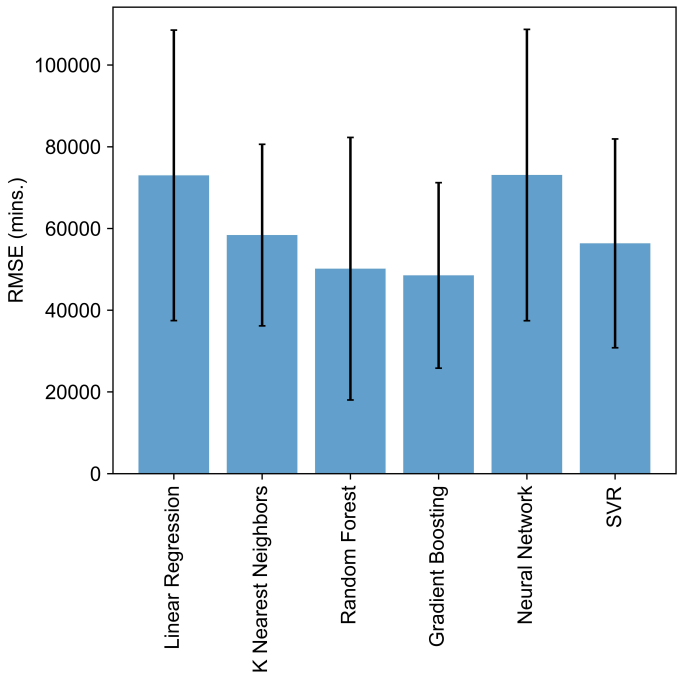

Figure 4-6: The RMSE for random forest algorithm, with non-normalized input.

absorber leads to unstable films, in comparison to the pure end-member films like $MAPbI_3$ or $MAPbBr_3$. This phenomenon has been previously investigated and is well-known within the research field. The $MAPb(I_xBr_{1-x})_3$ material system is intrinsically unstable due to light-induced halide phase segregation, where under illumination, the mixed-halide perovskite segregates into I-rich region and Br-rich region [13, 14]. Different models have been investigated by researchers to explain how this anion phase segregation in $MAPb(I_xBr_{1-x})_3$ alloys is initiated. There is a couple of reasons, for example, due to its intrinsically metastable mixed-halide alloys [15], polaron formation that leads to local strain [9, 10], positive free energies of mixing [33, 111, 142], electrons trapped by defect states and holes trapped in I-rich domains causing electric fields that drive demixing [65], trapped carrier concentration gradient leading to strain or thermalization energy [4], and surface defect carrier trapping leading to electric field-induced anion drift [51, 7].

These studies agree that light-induced anion phase segregation is reversible if the mixed-halide materials are subjected to a light-dark duty cycle. However, in this thesis chapter, all the films are subjected to prolonged illumination during the

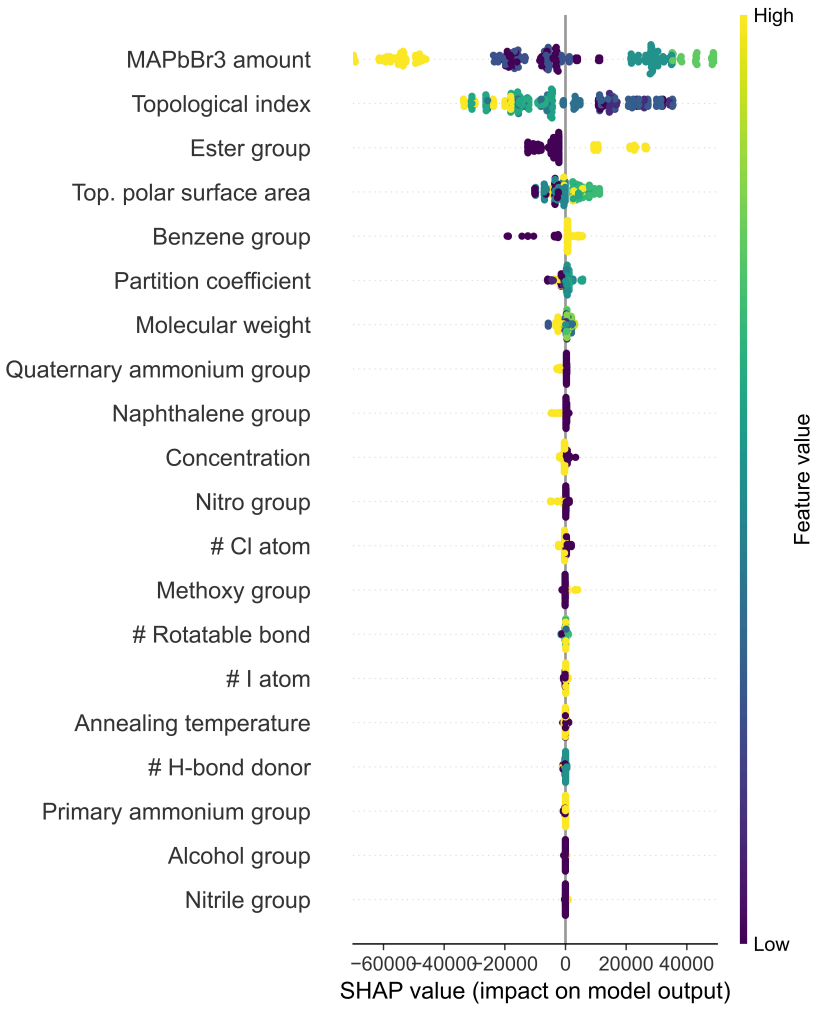

Figure 4-7: SHAP analysis result of the top 20 features based on a trained random forest algorithm.

degradation. They do not undergo the illumination duty cycle, making it one of the main degradation pathways within the films.

A study by Hoke [51] also reports how the phase segregation starts happening at $x = 0.8$ for $MAPb(I_xBr_{1-x})_3$ mixed-halide perovskite, while Draguta [33] reports that at $x = 0.88$, the mixing free energy profile starts to change under illumination. Regardless of the x-limit, this thesis chapter explores the $MAPb(I_xBr_{1-x})_3$ mixed-halide in 25%-increments, starting with $x = 0.75$, lower than the x-limit; hence, we can conclude that the mixed-halide absorber films that we investigate in this chapter indeed undergo light-induced anion phase segregation.

A clearer look at this phenomenon can also be seen in Figure 4-8, which shows the instability metric distribution comparison of various absorber compositions for bare, PTEAI-capped, and 9-Cl-capped films. While the capping layer can help in some absorbers, such as 9-Cl in $MAPbBr_3$ films, it only decreases the instability by a modest amount.

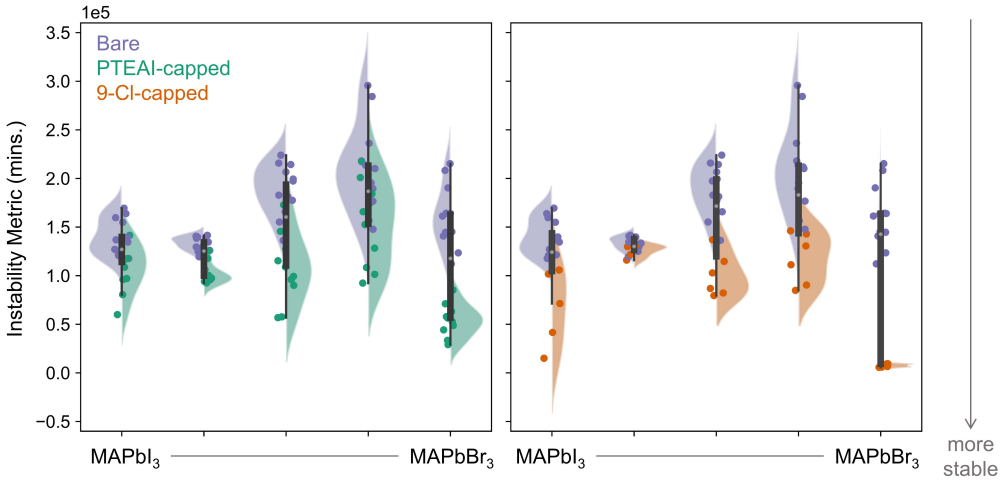

Figure 4-8: Instability metric distribution of various absorber compositions for bare, PTEAI-capped, and 9-Cl-capped films.

Note that the mixed-halide absorber has such a large distribution of instability metric, indicating the variance within the same sample set. This is actually common within the $MAPb(I_xBr_{1-x})_3$ series, where the film quality and microcrystallinity are sensitive from processing condition variations, which in return affect the photoseg-

regation kinetics and the resulting film stability [54]. Therefore, it is not surprising that we observe a high variation of film stability even for the same set of samples.

Capping layer material selection based on functional groups for improved stability

A study by Belisle and colleagues [7] suggests that the photoinduced halide segregation is caused by carrier trapping and surface defects, leading to electric field-induced anion drift. They suggest that passivating surfaces can suppress this degradation route to reduce electron traps. In their study, they introduce an electron-donating ligand, which is also a Lewis base, trioctylphosphine oxide (TOPO), to reduce non-radiative recombination. Note that TOPO would be a large molecule sitting on top of the absorber, as supposed to react with the excess-Pb to form LD perovskite, like the ones explored in this thesis. The main difference is the capping layer materials in this chapter have positive *A*-site cations, they are Lewis acid (electron-pair acceptor), even though the functional groups do have electron lone pairs. However, this still suggests that the capping layer could be one route in suppressing the light-induced halide segregation. Based on the result in the previous section, the capping layer is limited in reducing the instability of various absorbers.

Looking at the features affecting stability significantly, excluding the amount of $MAPbBr_3$, the next 3 most important features are the topological index that describes complexity, ester group, and topological polar surface area. Both topological index and topological polar surface area as top features agree with the findings in the previous Chapter 3. However, we see that the presence of ester group in the *A*-site cations, such as in 2-Cl ($2\,CO_2Me-PEA-Cl$) and 7-Cl ($3\,CO_2Me-PEA-Cl$), actually reduce the film stability. This is especially clear in the case of I-rich absorber, as shown in Figure 4-3. The requirements for ester groups to undergo hydrolysis are nucleophile availability, such as water and heat, present during the degradation process. The organic *A*-site cations in 2-Cl and 7-Cl can degrade this way.

Interestingly, based on the SHAP dependence analysis, the combination of the amount of $MAPbBr_3$ and the presence of the nitro group, such as in 4-I ($2\,NO_2-PEA-I$)

and 5-Cl ($3\,NO_2-PEA-Cl$), affects the stability differently, as shown in Figure 4-9. In an I-rich absorber, having a capping layer with a nitro group leads to an unstable film, while in a Br-rich absorber, having a nitro group leads to a stable film. The nitro functional group needs to be in the strong acid condition to undergo the hydrolysis process, which is unlikely to happen. On the other hand, the nitro group actually has the highest number of lone pairs, coming from the terminal oxygen atoms of $-NO_2$, among the functional groups explored in this study. Therefore, the capping layer material with a nitro group is a Brønsted-Lowry base capable of accepting more protons than other functional groups in this set of materials. However, the underlying mechanism for observing Br-dependent stability for the nitro-based-capped film still needs to be investigated further.

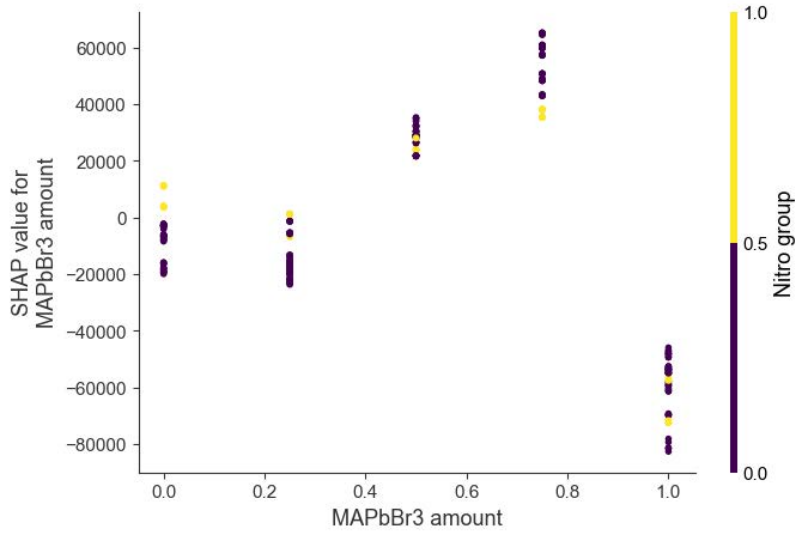

Figure 4-9: The SHAP dependence result for amount of $MAPbBr_3$ and the nitro group presence.

If we consider the degradation pathway of $MAPbI_3$ in Equation 1.2, where methylammonium iodide, as one of the products from $MAPbI_3$ degradation, is converted to methylamine and hydroiodic acid in the presence of water, light, and oxygen [92], it is also possible that the A-site cations of the capping layer are also deprotonated. Therefore, depending on how likely the LD perovskite degrade into its AX salt, and how easily the A-site cations get deprotonated, that will also determine how fast the

degradation proceeds.

A complete discussion on degradation mechanisms is further elaborated in Section 4.5.

4.4 Stable capping material characterization

After seeing how the 9-Cl generally outperforms the stability of other 1D perovskite capping layers, we need to investigate the reason behind this improvement carefully. Optical and structural properties are investigated, as well as the topography and surface photovoltage. Surface photovoltage result is especially needed to understand how the electrostatic properties on the surface change after introducing a new capping layer and the shift from I-rich to Br-rich absorber with higher anion electronegativity.

4.4.1 Optical and structural properties

The optical properties and the bandgaps need to be checked because these capping-absorber pairs will be used for tandem cells or indoor PV cells. The absorptance measurement for 9-Cl-capped and bare films is shown in Figure 4-10. The thicker color lines indicate the 9-Cl-capped film, while the thinner color lines indicate the bare films. Since the absorptance plots are quite similar for capped film and its corresponding bare film, there is no significant change of the bandgap between the capped and the bare films. As more Br is added to the $MAPbI_3$, the absorptance is blue-shifted, indicating the increase in the bandgap.

The crystal structure of 9-Cl-capped film for $MAPb(I_xBr_{1-x})_3$ can also be seen in Figure 4-11. Two things can be immediately observed as more bromine is added to the absorber, (1) the $MAPbI_3$ peak at 14.12° is shifted to 14.96° peak of $MAPbBr_3$, and (2) the PbI_2 peak at 12.56° is shifted to 13.4° peak of $MAPbBr_3$. Interestingly, the 9-Cl low-dimensional perovskite forms different phases, depending on the perovskite absorber composition. In the case of $MAPbI_3$, the low-dimensional perovskite phase appears at 6.08° and 6.52°, while in $MAPbBr_3$, the phase appears at 8.84°.

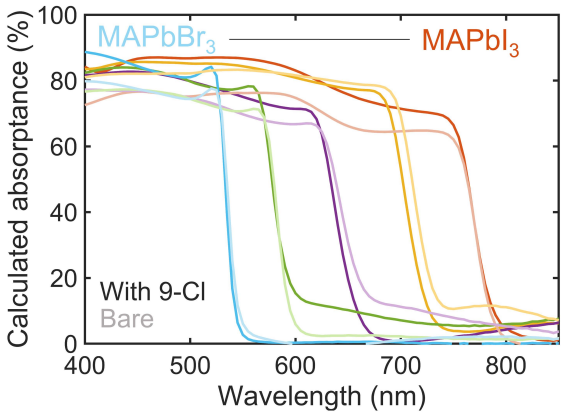

Figure 4-10: The absorptance of 9-Cl-capped film for $MAPb(I_xBr_{1-x})_3$ series.

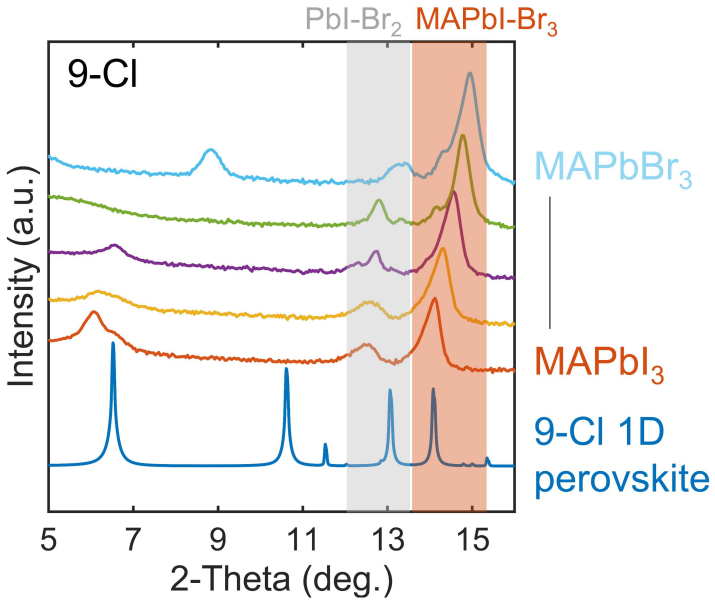

Figure 4-11: The crystal structure of the 9-Cl-capped $MAPb(I_xBr_{1-x})_3$ series.

4.4.2 Topography and surface photovoltage

We collaborate with a team led by Dr. Sarah Wieghold at Argonne National Laboratory to examine the topography and the surface photovoltage of capped- and bare films. The atomic force microscopy (AFM) result reveals the surface topography for the bare and 9-Cl-capped film of $MAPbI_3$ and $MAPb(I_{0.5}Br_{0.5})_3$ is shown in Figure 4-12. In the 9-Cl-capped film, the surface roughness is reduced by more than 50% than the bare film of $MAPbI_3$, showing the reduction in pinholes, and better film coverage, which will improve device performance. However, this is not always the case. In the case of $MAPb(I_{0.75}Br_{0.25})_3$, the deposition of the 9-Cl capping layer actually makes the film surface rough, possibly introducing pinholes that will hurt device efficiency.

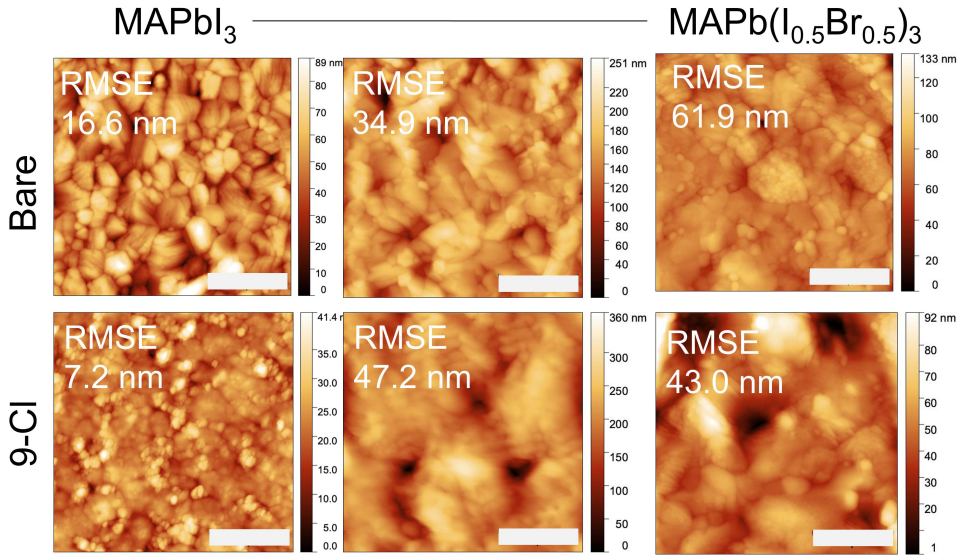

Figure 4-12: The AFM of bare and 9-Cl-capped films from $MAPbI_3$ to $MAPb(I_{0.5}Br_{0.5})_3$.

The scale bar is 1 µm.

To understand how the illumination-induced surface potential change as a capping layer is introduced, surface photovoltage (SPV) measurement is conducted. Figure 4-13 shows the summary of SPV results showing the absolute potential change between dark and white light-illuminated measurements for bare, PTEAI-capped, and 9-Cl-capped $MAPb(I_xBr_{1-x})_3$ films. The I-rich absorber materials show negative potential change, indicating p-type material, while the Br-rich show positive potential change,

indicating n-type material. Compared to the bare films, introducing a 9-Cl capping layer alters the SPV more significantly and makes the absolute potential change effect more pronounced.

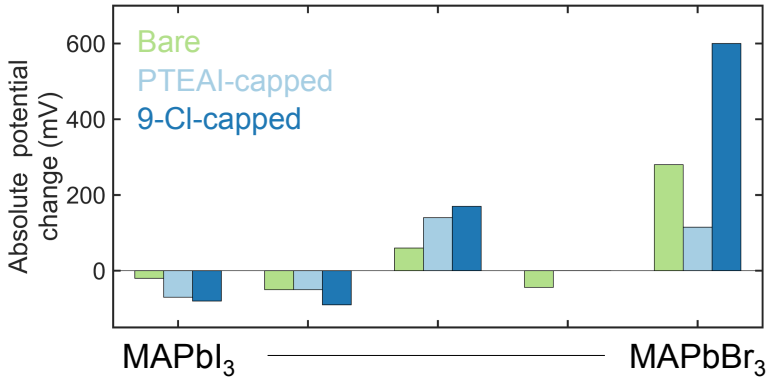

Figure 4-13: The surface photovoltage result of bare and 9-Cl-capped films from $MAPbI_3$ to $MAPbBr_3$.

4.5 Discussion on the degradation mechanism

Looking at the stressors present during degradation: illumination, humidity, oxygen, and heat, we foresee 4 possible routes of degradation: anion drift, the breakdown of organics (including deprotonation of A-site cations), crystal structure change, and oxygen adsorption. The surface photovoltage result supports the aninon drift hypothesis, but the other 3 routes cannot be excluded.

We hypothesize that the anion the capping layer holds a certain net electrostatic charge, which causes anion drift observed previously [82]. This results in the accumulation of anions within the interface between the capping and absorber layers and induces the second phase formation. Based on the SPV data, the capping layer changes the net electrostatic charge on the surface.

It is also possible that the organics are breaking down, specifically the A-site cations of the 2D/1D perovskite undergoing deprotonation, where it loses H^+ and converts the ammonium cation into an amine, which is already investigated in the case

of phenethylammonium cation [114, 34]. Note that the deprotonation cannot happen in quaternary ammonium such as $PTEA^+$ in PTEAI, therefore, another degradation mechanism takes place for this particular compound. The rest of the capping layers explored have primary ammonium, and thus, can undergo deprotonation. The pK_a measures how likely a compound gives up a proton; therefore, low pK_a corresponds to a stronger acid, with a higher likelihood of giving up a proton. Based on the simulated pKa values for 1D organics A-site cations, 4-I ($2\,NO_2-PEA-I$) is more likely to give up its proton (p$K_a = 9.35$), while 9-Cl ($2\,MeO-NEA-Cl$) and 6-I ($3\,MeO-PEA-I$) are less likely to be deprotonated (p$K_a = 9.92$ and 9.99, respectively). On the other hand, the branches breaking down from relatively stable phenyl/naphthyl rings in the capping A-site cations is unlikely to happen because their reactions are kinetically not favorable. These reactions require higher energy, and sometimes, a very basic or acidic condition to proceed.

The crystal structures also possibly change, similar to the case of Ruddlesden-Popper perovskite that has its n number of layers reduced due to the presence of water [114, 144]. Depending on how thermodynamically stable these secondary phases are, these could accelerate or decelerate the degradation process [144]. For instance, in butylammonium iodide, the secondary phases are stoichiometrically more hydrophobic, improving material stability [144].

Another degradation pathway is driven by oxygen adsorption, which eventually turns into superoxide formation [96]. The generation of superoxide anions initiates the degradation under light, which oxidizes the perovskite surface and slowly hydrates the inner perovskite, despite the very low humidity condition. Investigating the likelihood of low-dimensional perovskites getting oxidized in future studies will be required in unraveling how capping layer materials might help to suppress the oxygen adsorption-based degradation.

It is challenging to pinpoint which degradation route among these 4 dominates when all the stressors are present during the aging test. The dominating degradation mechanism likely differs across these 1D capping layer materials and the mixed-halide absorbers.

4.6 Conclusion

In this chapter, we investigate the effect of mixed-halide absorber composition on the optimum capping layer material. 10 new 1D perovskite and PTEAI capping materials, which form 55 different combinations of capping-absorber pairs are explored. We discover a new capping layer, 2 MeO – NEA – Cl (9-Cl), that improves the stability of $MAPbI_3$ and $MAPbBr_3$ by about 25%, in comparison to the previous capping layer champion material: PTEAI.

We discover that the intrinsic absorber stability plays a more important role in film degradation than the capping layer type itself. There is a limitation in saving absorbers with intrinsically poor stability using the capping layer method. There are also 4 possible routes of degradation due to the presence of oxygen, heat, water, and illumination: anion drift, the breakdown of organics (including deprotonation of *A*-site cations), crystal structure change, and oxygen adsorption. While surface photovoltage measurements certainly support the anion drift hypothesis, at present, we cannot exclude any of these four mechanisms or their combinations.

We also use a new method to analyze a 4-dimensional dataset from degradation test images called distance measure, which helps to construct the dissimilarity matrix. This matrix is useful in looking at the whole dataset and pick which one stands out the most. We also use SHAP analysis, which is already introduced in the previous chapter, to look at how various functional groups in the capping layers affect the film stability to a certain degree.

Chapter 5

Improving stability of $MAPbI_3$ in inverted device architecture

5.1 A low-cost inverted structure needs a boost in stability

In previous chapters, we focused on the more common PSC architecture, the *n–i–p* device, and deposited capping layers on top of a bare perovskite absorber. However, based on a recent technoeconomic analysis, perovskite photovoltaic modules with an inverted architecture, *p–i–n*, is expected to be around 28% cheaper ($\$0.41/W_P$ for *p–i–n* versus $\$0.57/W_P$ for *n–i–p*) due to the differences in ETL, HTL, and electrode layer materials [123, 23]. However, limited studies incorporate capping layers for PSC devices in *p–i–n* configuration, as mentioned in Section 1.4.3.

There are 3 different ways capping layers can be inserted into the *p–i–n* device architecture, as shown in Figure 1-9: at the bottom (between HTL and absorber), at the top (between ETL and absorber), and both bottom and top of the perovskite absorber layer. When the capping layer is deposited at the top, the stability has improved, but the performance is similar to those without the capping layer [83]. When the capping layer is deposited at both top and bottom of the absorber, the performance is reduced even though the stability is improved [67]. Inserting the

capping/low-dimensional perovskite layer at the bottom can improve both stability and surface passivation, leading to decreased nonradiative recombination and improved efficiency, as shown in a paper by Hangoma and colleagues [45]. The stability is not due to the protection provided by the capping layer against humidity and ion diffusion in the case of top layer deposition, but it is mainly due to larger grains and a more compact film [45]. The paper suggests that the 2D perovskites serve as a template that helps the crystal growth of the 3D perovskite on top. The 2D phase, after the annealing step of the absorber deposition, also disappears, leaving a more crystalline 3D perovskite phase [45]. Therefore, this particular way is different from what we are aiming for.

In fact, the disappearance of the 2D phase after annealing might be due to capping layer solubility in the DMF: DMSO solution being used to deposit the absorber on top. Therefore, if we would like to continue using solution-processing-based deposition to achieve the stratified layers of capping layer at the bottom and absorber at the top, we need to investigate the solvent compatibility for both layers. A solvent chosen for a layer's deposition might or might not dissolve the layers underneath.

In this thesis chapter, we, therefore, shift our focus to explore a method to incorporate the capping layer in an inverted device, specifically inserting the capping layer at the bottom. This structure is chosen because we have so far observed that the capping layer in a *n–i–p* device architecture allows efficient electron-hole extraction, which leads to a better performance, due to a good band alignment with the HTL and absorber [155]. Hence, this suggests that depositing capping layer at the bottom could lead to an efficiency improvement and possibly a stability boost for *p–i–n* PSC devices.

The first step that we need to take is testing solubility to determine the solubility limit of our materials, and to identify compatible capping-absorber pairings. This is illustrated in Figure 5-1. We first need to deposit the capping material A^IX^I, that is deposited with solvent M. The absorber, $A^{II}BX_3^{II}$, is subsequently deposited with solvent N. We expect that there would be two outcomes, (1) the solvent N dissolves very little capping material (A^IX^I), and as a result, we get 2 stratified

layers, or (2) solvent N dissolves the capping material completely, and we end up with a mixed-3D/LD perovskite.

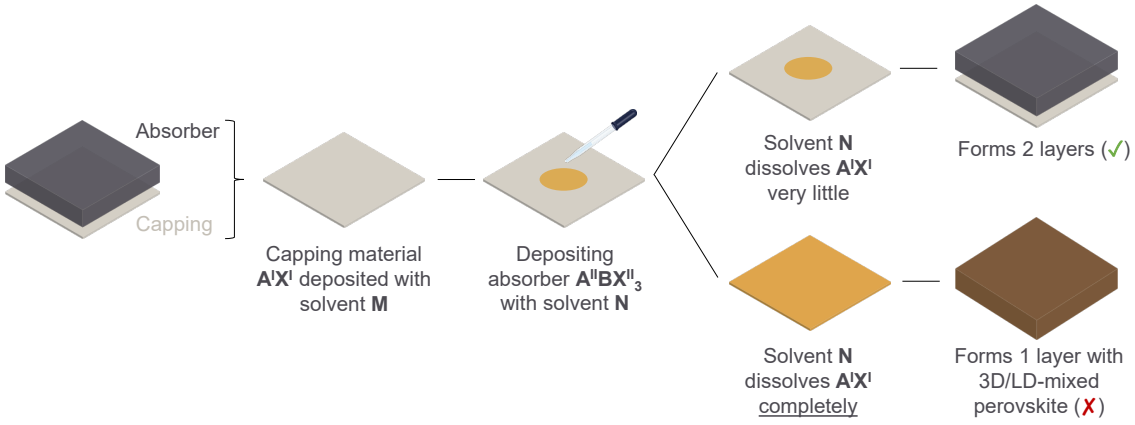

Figure 5-1: The possible outcomes of bottom capping layer deposition.

5.2 Solubility test for bottom capping layer

Since we stick with the solution-processing deposition method, we need to do a solubility test to find the solvent systems compatible with our materials. The following solubility tests were conducted.

1. The A^IX^I capping layer needs to be dissolved in solvent M in 10-20 mM concentration.

2. The $A^{II}BX_3^{II}$ absorber needs to be dissolved in solvent N in preferably 1.2 mol/L (M) concentration.

3. The absorber solvent, N, does not dissolve the capping layer already deposited and annealed (A^IX^I).

Based on these criteria, we test different solvents with different polarities. The capping layer material is the stable capping layer material from Chapter 3, phenyltriethylammonium iodide (PTEAI) in 10 mM (mmol/L) concentration. The absorber material is $MAPbI_3$, with ~1.2 M (mol/L) concentration. The solvents tested, from

less to more polar [18], are toluene, chlorobenzene, diethyl ether, isopropyl alcohol, acetone, acetonitrile, and dimethylformamide (DMF). The result of the solvent tests is shown in Table 5.1. We can only dissolve the $A^{II}BX_3^{II}$ powder in DMF, or more polar solvent with such high absorber concentration. However, this will immediately dissolve the capping layer underneath. Therefore, depositing the capping layer at the bottom with this method will not work. We need to find an alternative method to still deposit the capping layer at the bottom.

Solvents	10 mM capping layer solubility	~1.2 M absorber solubility
Toluene	No	No
Chlorobenzene	No	No
Diethyl ether	No	No
Isopropyl alcohol	Yes	No
Acetone	Yes	No
Acetonitrile	Yes	No
DMF	Yes	Yes

Table 5.1: The solubility test result for both capping layer and absorber materials. The polarity of the solvent increases as we go down the list.

5.3 A new strategy: switching capping and absorber layer for the bottom capping layer

One workaround to still deposit the capping layer at the bottom and absorber at the top is by switching the materials. We can treat the MAI, or methylammonium iodide, as a capping layer while mixing PTEAI with PbI_2 to form the bottom layer. With this new strategy, we might not obtain good film morphology right away, and this will thus need several rounds of optimization, especially if we bring the film to the device level. In this thesis chapter, we describe the development of a deposition method that can obtain a $MAPbI_3$ phase with a LD perovskite phase at the bottom of the film.

5.3.1 Deposition method

In DMF mixed with dimethylsulfoxide (DMSO) solvent, the PbI_2 in 1.34 M concentration can be dissolved easily. The addition of 10 mM PTEAI into this solution still produces a homogeneous solution. In this case, we are using 4: 1 DMF: DMSO solvent, which is commonly used in halide perovskite deposition. In the future, this DMF: DMSO ratio will need to be optimized because researchers have found that the change in the ratio of these two solvents controls the crystal growth during the deposition and annealing, which are responsible for the film morphology [75, 115]. To maintain the 1: 1.09 ratio of MAI: PbI_2, with an excess of lead (II) iodide, the film will need to have 1.34 M of PbI_2 and 1.22 M of MAI. However, due to the MAI solubility limit in IPA (isopropyl alcohol), the MAI concentration being dissolved is 0.62 M. Therefore, in this thesis chapter, the A^IX^I is PTEAI, the BX_2^{II} is PbI_2, and the $A^{II}X^{II}$ is MAI. The solvent M for both A^IX^I and BX_2^{II} is 4: 1 DMF: DMSO, and the solvent N for $A^{II}X^{II}$ is IPA (isopropyl alcohol).

The next step is to investigate which deposition method is suitable for our materials. Since the solubility test shows that the absorber's solvent will dissolve the capping layer, it is impossible to do the same deposition method as the previous chapters. Two alternative deposition methods are proposed, as shown in Figure 5-2. First, we can do a 2-step deposition (#2, capping method) by depositing the mix of A^IX^I capping layer with BX_2^{II} and annealing them, then depositing the $A^{II}X^{II}$ next and annealing them again for the second time. Second, we do a 1-step deposition (#3, anti-solvent method) by depositing both the A^IX^I capping layer with BX_2^{II}, then, instead of depositing chlorobenzene as anti-solvent, we deposit the $A^{II}X^{II}$ as anti-solvent and finally anneal them once. The table explaining these 2 different methods is shown in Table 5.2.

Using the proposed method #2, where we deposit MAI as a capping layer, we immediately see an encouraging result. As soon as the MAI gets deposited in the second layer, the film color changes from yellow to brown. After spincoating, the film is annealed at 100 °C for 10 minutes, and the film turns completely dark, as shown

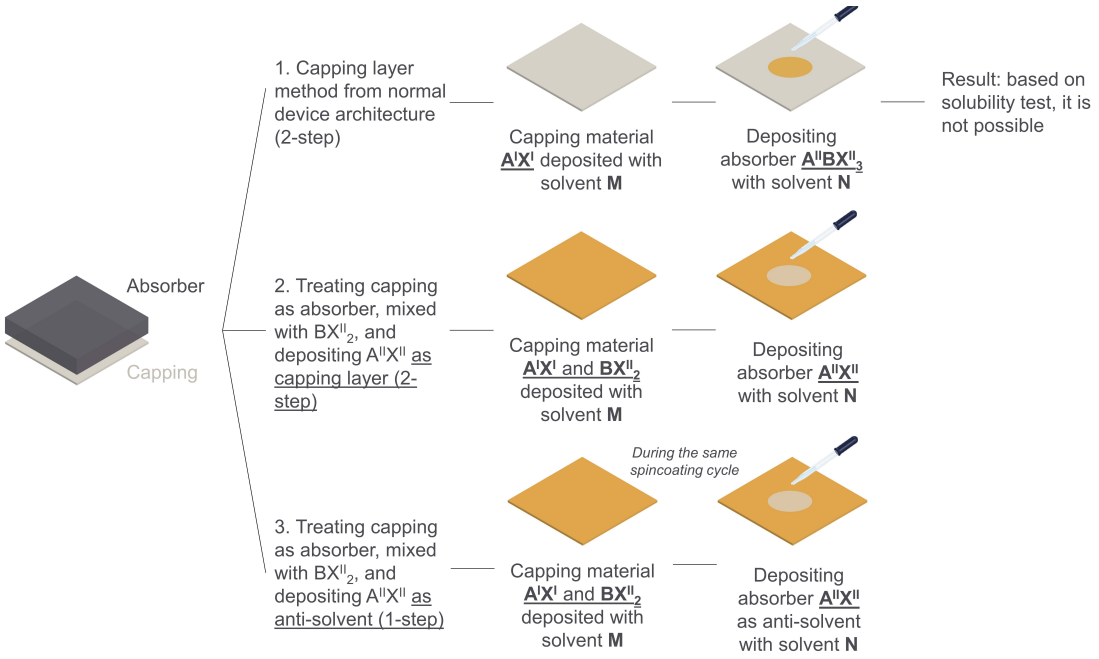

Figure 5-2: The different deposition methods explored for bottom capping layer.

Method	#2, capping method	#3, anti-solvent method
A^IX^I, BX_2^{II}, and solvent M	10 mM PTEAI, 0.673 M or 1.345 M PbI_2, in 4: 1 DMF: DMSO	10 mM PTEAI, 0.673 M or 1.345 M PbI_2, in 4: 1 DMF: DMSO
$A^{II}X^{II}$ and solvent N	0.617 M MAI in IPA	0.617 M MAI in IPA
Step 1 deposition	10 mM PTEAI mixed with 0.673 M or 1.345 M PbI_2, in 4: 1 DMF: DMSO is deposited, with 2-step deposition. Chlorobenzene is used as anti-solvent. The film is annealed at 100 °C for 10 minutes.	10 mM PTEAI mixed with 0.673 M or 1.345 M PbI_2, in 4: 1 DMF: DMSO is deposited, with 2-step deposition. 0.617M MAI in IPA. The film is annealed at 100 °C for 10 minutes.
Step 2 deposition	0.617M MAI in IPA is deposited on top of first layer, with no anti-solvent. The film is annealed at 100 °C for 10 minutes.	-

Table 5.2: The summary of proposed methods for depositing bottom capping layer.

in Figure 5-3. After fabricating the samples using both methods, we need to check how their surface morphology changes, whether we get a compact film, the polycrystalline structure within the films, their chemical compositions, their optoelectronic properties, and lastly, but more importantly, if we indeed get 2 stratified layers of LD PTEAI perovskite at the bottom layer, and $MAPbI_3$ perovskite absorber at the top layer.

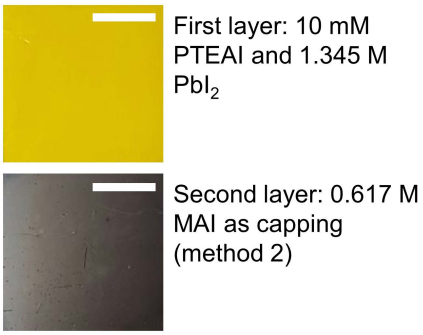

Figure 5-3: The film color change for method #2, using MAI as the capping layer. The scale bar is 1 cm.

5.3.2 Surface morphology

To see how the surface morphology changes after MAI deposition either as a capping layer or as an anti-solvent, we use scanning electron microscopy (SEM, ZEISS Ultra-55). The result is shown in Figure 5-4.

The 0.67 M PbI_2 with 10 mM PTEAI in the first layer introduces textured surfaces, in comparison to the 1.34 M PbI_2 with 10 mM PTEAI. However, note that the latter introduces a lot more excess of PbI_2, which could increase the intrinsic instability at the expense of more compact, pinhole-free film, for an efficiency boost [78]. The 0.67 M PbI_2 with 10 mM PTEAI film one is also likely to be thinner, as observed in the case of mixed-perovskite $FA_{0.83}MA_{0.17}Pb(I_{0.83}Br_{0.17})_3$ [27]. ~0.65 and ~1.25 M precursor solution correspond to roughly 100 and 380 nm films, respectively [27].

After depositing the 2nd layer, we can observe the difference between method #2, MAI as capping layer, and method #3, MAI as anti-solvent. Adding MAI as anti-

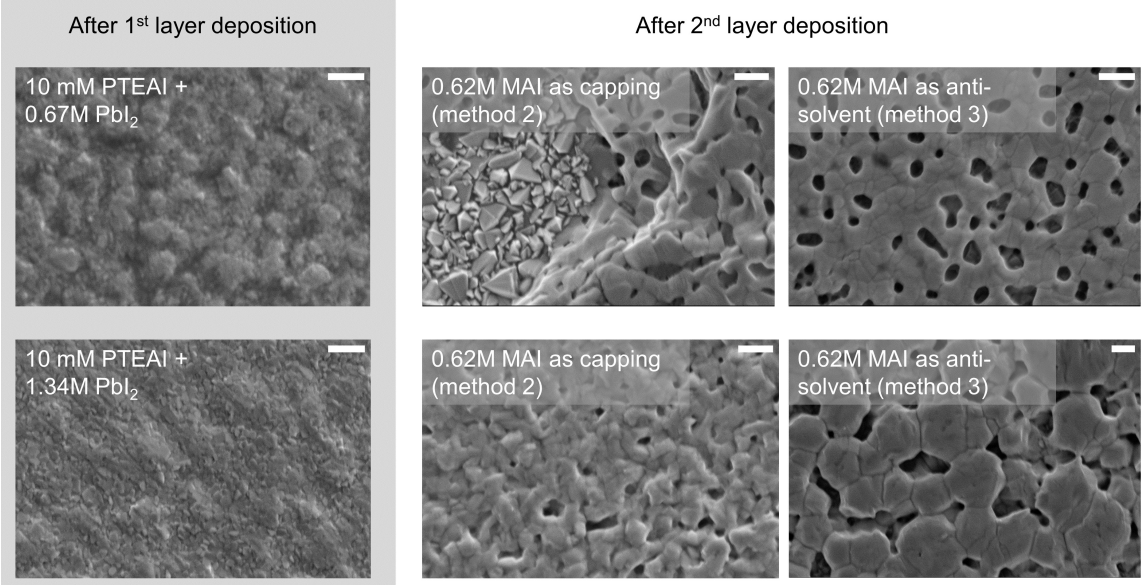

Figure 5-4: The surface morphology of bottom capping layer, for both capping and anti-solvent methods.

The scale bar is 500 nm.

solvent allows the MAI to react with the PbI_2 precursor underneath in intermediate step. This results in smoother film, as shown in Figure 5-4. The only difference between low versus high concentration of PbI_2 in the anti-solvent method is that high PbI_2 concentration leads to larger grains, while for low concentration, it leads to smaller grains.

On the other hand, method #2, where we add MAI as a capping layer and has an annealing step between the two depositions, results in a rougher surface with a large variety of grain sizes. Therefore, we conclude that it is best to use method #3, where we add MAI as anti-solvent, to have a film with large grains and small grain size variations.

5.3.3 Structural properties

Next, we characterize our films to determine whether or not we created the $MAPbI_3$ phase. We use an X-ray diffraction tool (Rigaku SmartLab), using Cu K-α radiation, to check the phases within the polycrystalline film. The result is shown in Figure 5-5.

We observe the $MAPbI_3$ phase at $2\theta = 14.08°$ on all the films being compared:

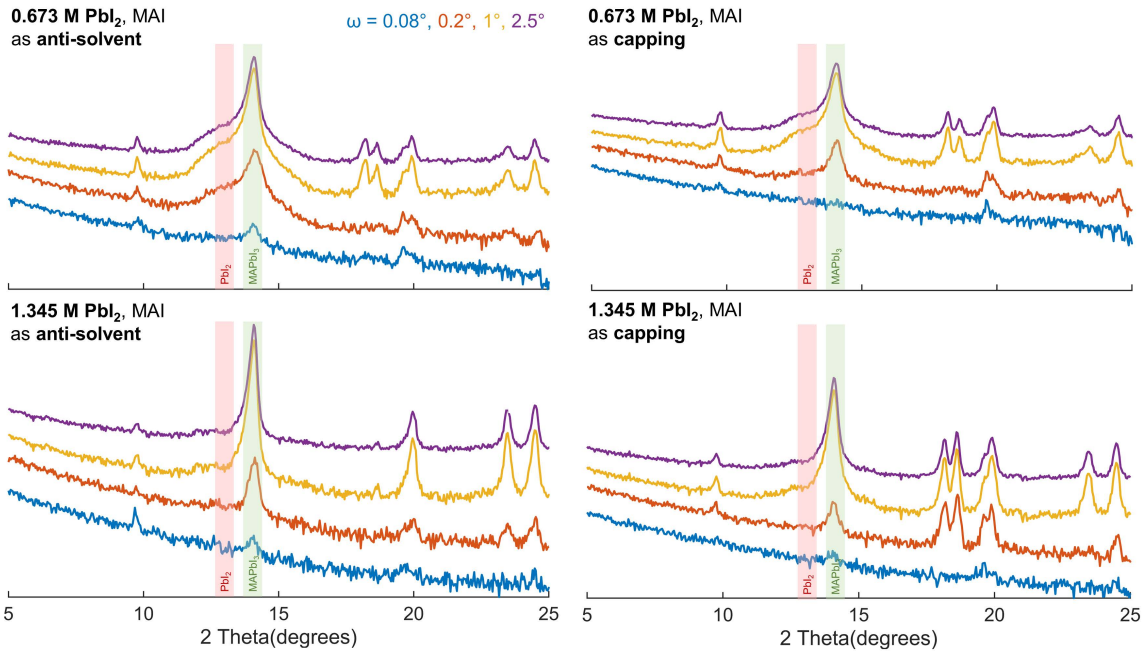

Figure 5-5: The XRD results for both 0.673 and 1.345 M PbI_2 with 10 mM PTEAI films with MAI as capping and as anti-solvent.

The red- and green-shaded area refers to PbI_2 and $MAPbI_3$ phase peaks.

0.673 and 1.345 M of PbI_2 mixed with 10 mM PTEAI, with 0.617 M of MAI as anti-solvent or as capping layer. The low-angle peak at 9.76° might be coming from low-dimensional perovskite formed. We also observe that a higher concentration of PbI_2 leads to a better crystallinity and a reduction in PbI_2 phase. The significant excess of PbI_2 might actually lead to another, different LD perovskite phase formation. Between the 2 deposition methods, MAI as anti-solvent and as capping, the $MAPbI_3$ phase presence is higher in the case of MAI as anti-solvent. If we look at the peaks at 18°-20°, these peaks may originate from the Ruddlesden-Popper series formed within the films, similar to the ones present in $(BA)_2(MA)Pb_2I_7$, $(BA)_2(MA)_2Pb_3I_{10}$, and $(BA)_2(MA)_3Pb_4I_{10}$, with ICSD collection codes 252315, 252316, and 252317, respectively [127].

The XRD in each sample is measured at different ω, 0.08°, 0.2°, 1°, and 2.5°, where ω is the incident angle between the sample and the X-ray source. We were hoping that we would distinguish the bottom versus top layer diffraction results, however, due to attenuation in both X-ray beam and diffracted signal, it is hard to investigate

and measure the crystal structure in a high degree of certainty. A synchrotron-based GIWAXS method, as being used in Chapter 3, might help distinguish the surface from the bulk layer, but it will be harder to determine the phase(s) in the bottom layer.

5.3.4 Optical properties

The absorptance comparison of both 0.673, 1.345 M PbI_2 and 10 mM PTEAI, with 0.617 M MAI as anti-solvent and capping layer is shown in Figure 5-6. Both the 10 mM PTEAI with 0.673 and 1.345 M of PbI_2 films are yellow, consistent with the absorptance drop at 520 nm. For MAI-capped and MAI as anti-solvent cases, however, the absorptance drop happens at a longer wavelength, around 800 nm, similar to the bare $MAPbI_3$ and $MAPbI_3$ with PTEAI capping at the top. This, therefore, confirms that the bandgap in these films is unaltered with the deposition of PTEAI capping at the bottom and $MAPbI_3$ absorber at the top.

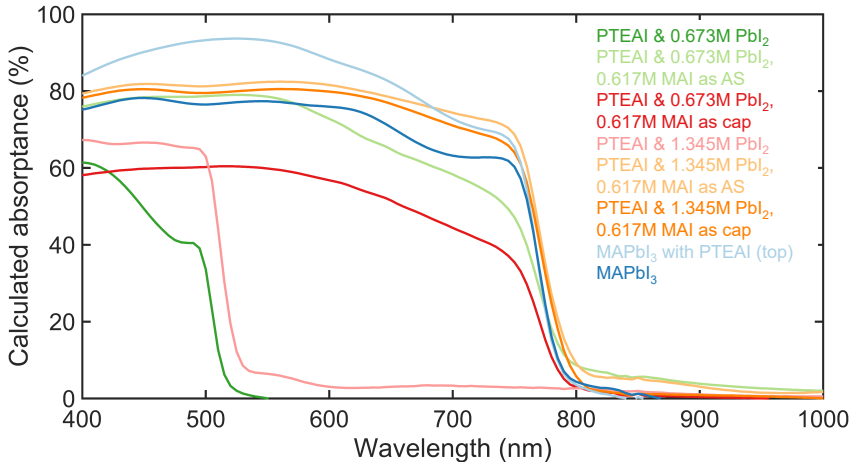

Figure 5-6: The absorptance results for both 0.673 and 1.345 M PbI_2 with 10 mM PTEAI films with MAI as capping and as anti-solvent.

Deposited as cap refers to the capping layer method (#2), while AS refers to the anti-solvent method (#3).

We also observe that for both 0.673 and 1.345 M PbI_2 with 10 mM PTEAI films, and 0.617 M MAI MAI deposited at the top, the absorptances are higher when we deposit the MAI using the anti-solvent method, as supposed to the capping layer

method. In the case of 0.673 M PbI_2 films, we even observe a 20%-difference in absorptances for the wavelengths below 800 nm between the anti-solvent and capping layer method. This, therefore, supports the previous findings that the MAI in PTEAI and PbI_2 films is best deposited using the anti-solvent method.

5.3.5 Degradation test result

The degradation results for both 0.673 and 1.345 M PbI_2 with 10 mM PTEAI films with MAI as capping and as anti-solvent are shown in Figure 5-7. The degradation test was under 85 °C, 80±5% relative humidity, and 0.15-sun.

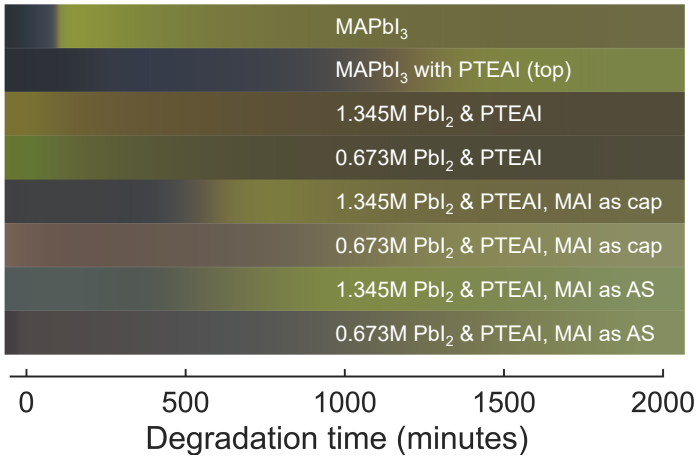

Figure 5-7: The degradation results for both 0.673 and 1.345 M PbI_2 with 10 mM PTEAI films with MAI as capping and as anti-solvent, under high humidity and temperature.

We observe that the initial film colors are different, which is consistent with the UV-Vis results. Without MAI deposition, the fresh films have a yellow color. Looking at the films with MAI deposited as a capping layer, it is not as stable as the films with MAI deposited as anti-solvent. This confirms that depositing MAI as an anti-solvent indeed is better than depositing it as a capping layer. We also observe that a higher PbI_2 excess amount in the film leads to unstable film due to accelerated photodecomposition of PbI_2 into lead and iodine, a phenomenon that has been investigated in the literature [138]. Surprisingly, the stratified film with MAI deposited at the

top and PTEAI and PbI_2 at the bottom still achieves higher stability at half of the precursor concentration, or approximately 0.3 of the thickness of $MAPbI_3$ film. It is also comparable with the stability of $MAPbI_3$ with PTEAI capping layer at the top, even though due to reduced thickness, the starting film color is slightly lighter.

5.4 Conclusion and outlook

The bottom capping layer, where the MAI is deposited on top of the mixture of 0.673 M PbI_2 and 10 mM PTEAI with anti-solvent method, leads to around 5 times improvement in stability compared to the bare $MAPbI_3$. This result is similar to having the PTEAI as a top capping layer of thicker $MAPbI_3$ absorber. This deposition method is, therefore, promising to achieve the bottom capping layer that we need. However, further investigation in their band alignment and ensuring that we indeed get stratified layers, needs to be done.

Based on various characterizations, depositing the MAI using the anti-solvent method provides a better film quality than using the capping layer method. To achieve even better film quality, 3 optimization steps still need to be done: (1) the composition and processing conditions to achieve desired morphology, (2) the solvents in precursor solutions to be able to have a higher concentration, and thus, a thicker film, and (3) the capping layer type to achieve better stability.

Another route to explore is using evaporation method. Even though it is less scalable in comparison to the solution processing method, it is solvent-free, generally a cleaner process, and the film thickness can be controlled more easily [140]. Using subsequent evaporation method, we can technically first deposit the LD perovskite capping layer at the bottom, before co-evaporating the AX and BX_2 precursors. There is currently no published study on this, which might be a sign that this method is actually challenging to execute [140]. Researchers have also observed that the different deposition steps need to be done in separate chambers to avoid cross-contamination, and it is hard to ensure the stoichiometry of co-evaporation method, which might lead to secondary phase formation [140]. Additionally, the methylammonium-based

perovskite has its own set of challenges to be deposited using evaporation method. First, the MA-based perovskite generally has smaller grains when deposited with this method in comparison to solution-based processing [140]. Second, the evaporation of MAI is harder to control due to its high vapor pressure and it is easily deprotonated to methylamine during the deposition [140]. These need to be considered as researchers explore this evaporation method to deposit the bottom capping layer.

Chapter 6

Beyond $MAPbI_3$: improving the stability of cesium-formamidinium-based perovskites

6.1 Mixed *A*-site cations drive high-efficiency devices

Various high-efficiency PSCs depart from using purely $MAPbI_3$ absorbers, and start incorporating mixed-cation, mixed-halide perovskites, such as $(FAPbI_3)_{0.95}(MAPbBr_3)_{0.05}$ [59], $Cs_{0.17}FA_{0.83}PbI_3$ [110], or $Cs_{0.05}FA_{0.85}MA_{0.10}Pb(I_{0.97}Br_{0.03})_3$ [158], with optimum capping layer and stable HTL material. Some of these devices have reached around 24%, with bandgaps between 1.5 and 1.6 eV, making them attractive alternatives to the perovskites based only on MA.

Even the MA-free perovskites still have a stability issue, albeit due to different reasons. In MA-based perovskites, the environmental humidity level plays a significant role. However, the intrinsic phase instability of $CsPbI_3$ and $FAPbI_3$ is due to thermodynamic instability, as mentioned in Section 1.4.4. The desired α phase of $CsPbI_3$ and $FAPbI_3$ are dark and photovoltaically active, however, they are only sta-

ble at high-temperature [148]. At room temperature, they turn into their respective δ phases, which are yellow, and lead to significantly lower efficiency [148]. Incorporating a small amount of MA has been shown to suppress phase separation of mixed-halide perovskites [131]. Finding a way to improve the phase stability in these mixed-halide compositions is, therefore, a key next step to improve the stability of lead-halide PSCs.

6.2 Shifting from film-level to device-level screening

We previously focused on film-level optimization, trying to answer which capping layer material will improve the stability of certain perovskite absorbers. However, as previously shown in Chapter 4, the answer to this question is not straightforward. Despite the necessary research on understanding each layer's degradation process, the outcome of the degradation test in a full device stack will still be different because of interface effects. Therefore, the co-optimization of all layers within the device is key to maximizing stability.

In this part of the thesis, we test our optimum capping layer in a full device stack to observe the degradation process. We also shift to using a capping layer at the top, between the absorber and the ETL, in a *p–i–n* inverted device, to investigate how the top capping layer might prevent degradation. The devices are tested in different degradation conditions, high and low humidity. Some parts of this thesis, specifically the device fabrication and measurement, are performed in collaboration with the Dauskardt group at Stanford University.

6.2.1 Effects of capping layers in low- and high-humidity environments

We first investigate the films, with their *p–i–n* optimum absorber, $Cs_{0.17}FA_{0.83}PbI_3$, and deposit 10 mM of PTEAI on top. This particular absorber composition does not have excess PbI_2. The combination of $CsPbI_3$ and $FAPbI_3$ in 17% and 83% is

also more stable [131] than methylammonium-based films that have been investigated throughout this thesis. $Cs_{0.17}FA_{0.83}PbI_3$ absorber also has good efficiency, making it one of the best composition alternatives for PSCs [110].

The films are then degraded at high temperature (85 °C), 0.15-sun illumination, and two humidity conditions: low (20±5)% and high (85±5)% relative humidity. The result is shown in Figure 6-1. It shows that in the low-humidity condition, the PTEAI capping layer does not improve the stability, however, in high humidity, the PTEAI capping layer on top of absorber starts to extend the stability of the $Cs_{0.17}FA_{0.83}PbI_3$ film. This means that the capping layer effectively prevents the formation of hydrates, which further leads to the formation of PbI_2. Interestingly, the capped-film in high humidity outperforms the capped-film in low humidity. This warrants a further investigation to understand how the degradation route changes in high humidity, which is supposed to be harsher, versus in low humidity conditions.

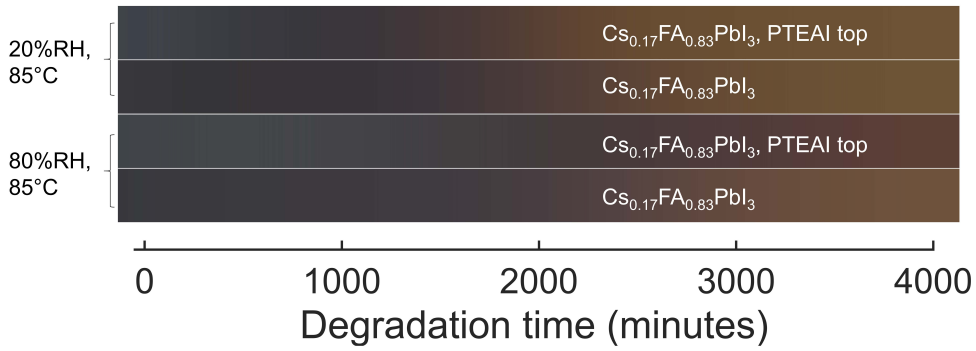

Figure 6-1: The degradation results for low and high humidity and high temperature for $Cs_{0.17}FA_{0.83}PbI_3$ films with PTEAI top capping layers.

Low humidity is (20±5)% RH, and high humidity is (80±5)% RH.

6.2.2 Silver electrode layer-induced degradation

Fabricating a full device stack requires a lot of resources and time, so we need to find a way to degrade as few device layers as possible but get the degradation output that represents the device-level degradation. Device architecture in *p–i–n* devices consists of the following layers, from bottom to top: indium-doped tin oxide (ITO)

glass as the bottom electrode, NiO as the hole transport layer (HTL), $Cs_{0.17}FA_{0.83}PbI_3$ perovskite absorber, PTEAI capping layer, C_{60} and BCP as electron transport layer (ETL), and the silver metal electrode at the top, with established fabrication protocols [110]. Some of the layers' deposition require thermal evaporation, while others only need solution-based processing. Depositing the whole device stack is therefore not as practical as fabricating films for the high-throughput experiment.

To find alternatives, we need to find a degradation route that happens due to layers other than the absorber within the device. We suspect that one important degradation mode presents in devices but not in films related to the metal electrode layer, which is silver. There is reported evidence that iodine anions diffuse through the ETL, and forming silver (I) iodide AgI on the surface [72]. The AgI barrier results in poor charge transport, which affects the efficiency significantly. Incorporating a metal layer on the film is therefore important to mimic the device-level degradation process. We deposit a 30 nm silver layer at the top of the capping layer or the absorber directly, in the case of a control set of samples, to understand how the capping layer at the top might prevent the ion diffusion in the device [72], which is detrimental to device stability.

We flip the samples, with the silver layer touching the hot plate, to still capture the images of films. We degrade them in a low humidity condition (20±5)% RH, at 85 °C, and 0.15-sun illumination level. The result is shown in Figure 6-2, showing the PTEAI capping for $Cs_{0.17}FA_{0.83}PbI_3$ absorber indeed helps to prevent the iodine anions from diffusing and forming AgI and makes the film lasts longer. It also confirms that the capping layer can act as a barrier layer. Note that the degradation timescale is longer than previous chapters with MA-based perovskites because Cs-FA-based perovskites are more stable, and the samples are also flipped during degradation.

6.2.3 Fully encapsulated device degradation

We also degrade the fully encapsulated device, which has all the aforementioned layers, and the butyl encapsulation. This prevents the water molecule from getting in. The samples are degraded under damp heat condition with high temperature and

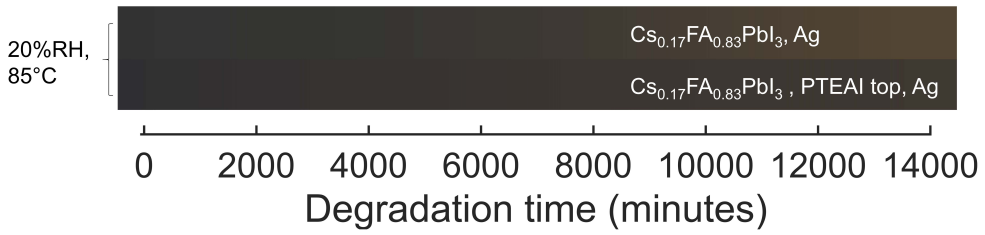

Figure 6-2: The degradation results for low humidity and high temperature for $Cs_{0.17}FA_{0.83}PbI_3$ film with PTEAI top capping and silver layer.

Low humidity is 20±5% RH. The films are flipped (the silver layer is facing down).

humidity (85%RH/85 °C).

The result is shown in Table 6.1. It shows that after 160 minutes, while the device efficiency average with no PTEAI capping layer is reduced to 0.77, the average of devices with PTEAI capping layer is reduced to 0.68 of initial efficiency. The PTEAI-capped film performs worse, which raises a question, why this differs from the previous film-level results. There could be several reasons, and they need to be investigated further. First, other interfacial interactions, such as between ETL and the capping layer, which affect the degradation process significantly could be present. Second, there might be some interactions between butyl and capping layer on the sides, which could also affect the degradation process.

Time (minutes)	Efficiency ratio	
	No PTEAI top capping	PTEAI top capping
160	0.77	0.68
404	0.75	0.60
613	0.72	0.58
763	0.70	0.55

Table 6.1: The efficiency ratio average between aged and fresh encapsulated device under damp heat (85%RH/85 °C) degradation test.

6.3 Conclusion and outlook

We observe that the Cs-FA-based perovskite absorbers generally lead to better stability. Under high humidity, high-temperature conditions, they degrade between 2,000+

(for non-flipped films) to 10,000+ minutes (for flipped films). Compared to MA-based only perovskite absorbers that degrade within hundred minutes, the Cs-FA-based perovskite absorbers are more stable. However, incorporating small MA-based perovskite might be beneficial to further suppress the phase separation in the future.

When we transfer this Cs-FA-based perovskite with PTEAI top capping layer from film-level to the device-level, specifically in *p–i–n* device architecture, we start observing how the absorber-capping pair degrades and interacts with other layers and plays an important role in determining the stability. Under low humidity and high temperature, capping layer may help slow down the iodine anions which diffuse through the ETL and forming AgI with the silver electrode. We also observe that the aging test conditions also affect the degradation processes differently.

Therefore, exploring the mixed perovskite compositions, tailoring them with suitable capping layer, and moving from film- to device-level degradation test are necessary to explore and realize the device-level benefits of capping layers.

Chapter 7

Discussion and Conclusion

7.1 Summary of key results

The contributions of this work are two-fold: the scientific discovery and the data-driven approach.

From the scientific discovery side, 21 capping layer materials are screened for their stability effect on $MAPbI_3$ absorber. A new capping layer, phenyltriethylammonium iodide (PTEAI), is discovered and has a great potential to extend the stability of certain types of perovskite absorber under a specific degradation test condition. PTEAI top capping layer improves the stability of bare $MAPbI_3$ by $\sim$4 times. We also explore 10 new 1D perovskites and PTEAI capping layers with $MAPb(I_xBr_{1-x})_3$ absorbers, totaling 55 different capping-absorber material combinations. One of the 1D capping layers, $2\,MeO-NEA-Cl$, improves the stability of certain $MAPb(I_xBr_{1-x})_3$ compositions similarly or better than PTEAI. Besides, we discover that the capping layer capability in improving the mixed-halide absorber is limited; the intrinsic stability of the absorber still dominates the stability outcome. Lastly, we discover a new deposition method for the capping layer between the hole-transport layer and the absorber in the inverted device architecture: first, we deposit the capping layer material mixed with PbI_2 powder, and second, we deposit the MAI solution as anti-solvent.

From the data-driven approach side, we utilize Shapley value analysis to determine the most impactful molecular properties and processing conditions that lead to better

film stability. We also use the distance metric to compare 4-dimensional data, time and RGB color values, across different samples. Both methods are important as we evaluate increasingly higher-dimensional datasets in the future.

7.2 Future generation of LD capping layer PSCs

The thesis focuses on improving the methylammonium-based perovskite absorber and discusses the device performance results. In the future, the LD capping layer will be tuned based on the conduction and valence bands, especially as we explore a larger perovskite absorber compositional space beyond $MAPbI_3$. This will help avoid band misalignment, which can initiate degradation domains on the interface due to the accumulation of charges and hinder efficient charge-carrier extraction.

It is also important to control the crystal growth orientation of the LD perovskite capping layer in the future. The crystal preferably grows vertically to facilitate a more efficient charge transport without sacrificing the stability it provides. Several methods are already implemented in the case of 2D-3D mixed perovskite absorber, such as by doping the 2D perovskites with certain ions, for example, K^+ [66], or by combining hot casting method with a certain solvent, for instance, DMSO [122].

7.3 Toward PSCs device integration

The capping-absorber pair screening in the Chapter 4 shows an important step towards finding the most stable capping-absorber layer that might improve surface passivation. We synthesize a total of 55 different capping-absorber material combinations. 10 of them are 1D perovskite, which is less explored as capping layers in the literature. In the future, co-optimization of all layers, including the encapsulation material, will be the key to find the PSCs with optimum stability and performance.

Currently, the perovskite capping-absorber pair stability result does not consider the interaction between these layers with both ETL and HTL and the electrodes. We also observe in the Chapter 6 that as we move beyond MA-based perovskite and shift

to the device level, the interaction between the layers becomes more complicated. This creates a problem. Based on what we observe in the capping-absorber pair screening in Chapter 4, the most stable capping layer for one mixed-halide absorber composition is not necessarily the case for another absorber composition. This indicates a high probability that several combinations of PSC layers, which are very different from each other, lead to similar performance or stability. Hence, optimizing one layer at a time may not lead to the most efficient and/or stable device. In the future, we will need to co-optimize all the layers together.

Co-optimizing all the layers, which will reveal the global optimum stability and efficiency, will be possible in the future as computational power increases and high-throughput experiment (HTE) hardware improves. The suitable HTE setup for perovskite fabrication will enable high sample output that, in turn, will generate a large amount of data per time. Since halide perovskites can be fabricated via solution processing, various high-throughput deposition methods, such as drop casting or doctor blading, can be supported. Finally, to match the fast data generation, high computational power will be required to process and analyze the data. This unlocks the possibility to investigate highly dimensional data coming for complex systems, such as PSCs.

7.4 Closing remarks

The progress in PSCs is essential because they are predicted to be less expensive than silicon solar cells, despite their similar efficiencies. This will help lower the LCOE of solar panels and make it a more attractive renewable energy source from an investment standpoint. One of the challenges in bringing PSCs closer to the market is their environmental stability, which has been addressed with different strategies in this thesis. Hopefully, this important contribution will push PSCs closer to commercialization and help curb carbon emissions by enabling a transition to cleaner energy.

Appendix A

Code

The code presented in this thesis is available at MIT Photovoltaics Research Laboratory GitHub repository (`https://github.com/pv-lab`). The specific locations for each part of the thesis is as following:

1. The capping-layer GitHub repository to accompany Chapter 3 project, is available at (`https://github.com/PV-Lab/capping-layer`), which includes the screening of capping layer material for specific absorber, and utilizing random forest regression and SHAP value analysis to interpret the trained models.

2. The GitHub repository for dissimilarity matrix will be available on PV Lab GitHub page to accompany Chapter 4 project after the publication submission. This code focuses on utilizing dissimilarity matrix for comparing a large, multi-dimensional dataset, and to spot the differences and similarities right away using distance metric, such as cosine, Euclidean, or Manhattan.

Bibliography

[1] International Energy Agency. *World Energy Outlook 2020*. OECD Publishing, 2020.

[2] Naomi S Altman. An introduction to kernel and nearest-neighbor nonparametric regression. *The American Statistician*, 46(3):175–185, 1992.

[3] Lahoucine Atourki, Erika Vega, Bernabé Marí, Miguel Mollar, Hassan Ait Ahsaine, Khalid Bouabid, and Ahmed Ihlal. Role of the chemical substitution on the structural and luminescence properties of the mixed halide perovskite thin $MAPbI_{3-x}Br_x$ ($0 \leq x \leq 1$) films. *Applied Surface Science*, 371:112–117, 2016.

[4] Alex J Barker, Aditya Sadhanala, Felix Deschler, Marina Gandini, Satyaprasad P Senanayak, Phoebe M Pearce, Edoardo Mosconi, Andrew J Pearson, Yue Wu, Ajay Ram Srimath Kandada, et al. Defect-assisted photoinduced halide segregation in mixed-halide perovskite thin films. *ACS Energy Letters*, 2(6):1416–1424, 2017.

[5] Christopher J Bartel, Christopher Sutton, Bryan R Goldsmith, Runhai Ouyang, Charles B Musgrave, Luca M Ghiringhelli, and Matthias Scheffler. New tolerance factor to predict the stability of perovskite oxides and halides. *Science Advances*, 5(2):eaav0693, 2019.

[6] Lindsay Bassman, Pankaj Rajak, Rajiv K Kalia, Aiichiro Nakano, Fei Sha, Jifeng Sun, David J Singh, Muratahan Aykol, Patrick Huck, Kristin Persson, et al. Active learning for accelerated design of layered materials. *npj Computational Materials*, 4(1):1–9, 2018.

[7] Rebecca A Belisle, Kevin A Bush, Luca Bertoluzzi, Aryeh Gold-Parker, Michael F Toney, and Michael D McGehee. Impact of surfaces on photoinduced halide segregation in mixed-halide perovskites. *ACS Energy Letters*, 3(11):2694–2700, 2018.

[8] Issa Ibrahim Berchin, Isabela Blasi Valduga, Jéssica Garcia, José Baltazar Salgueirinho Osório de Andrade, et al. Climate change and forced migrations: An effort towards recognizing climate refugees. *Geoforum*, 84:147–150, 2017.

[9] Connor G Bischak, Craig L Hetherington, Hao Wu, Shaul Aloni, D Frank Ogletree, David T Limmer, and Naomi S Ginsberg. Origin of reversible photoinduced phase separation in hybrid perovskites. *Nano Letters*, 17(2):1028–1033, 2017.

[10] Connor G Bischak, Andrew B Wong, Elbert Lin, David T Limmer, Peidong Yang, and Naomi S Ginsberg. Tunable polaron distortions control the extent of halide demixing in lead halide perovskites. *The Journal of Physical Chemistry Letters*, 9(14):3998–4005, 2018.

[11] Pablo P Boix, Shweta Agarwala, Teck Ming Koh, Nripan Mathews, and Subodh G Mhaisalkar. Perovskite solar cells: beyond methylammonium lead iodide. *The Journal of Physical Chemistry Letters*, 6(5):898–907, 2015.

[12] Riley E. Brandt, Vladan Stevanović, David S. Ginley, and Tonio Buonassisi. Identifying defect-tolerant semiconductors with high minority carrier lifetimes: Beyond hybrid lead halide perovskites. *MRS Communications*, 5(2):265–275, 2015.

[13] Michael C Brennan, Sergiu Draguta, Prashant V Kamat, and Masaru Kuno. Light-induced anion phase segregation in mixed halide perovskites. *ACS Energy Letters*, 3(1):204–213, 2017.

[14] Michael C Brennan, Anthony Ruth, Prashant V Kamat, and Masaru Kuno. Photoinduced anion segregation in mixed halide perovskites. *Trends in Chemistry*, 2(4):282–301, 2020.

[15] Federico Brivio, Clovis Caetano, and Aron Walsh. Thermodynamic origin of photoinstability in the $CH_3NH_3Pb(I_{1-x}Br_x)_3$ hybrid halide perovskite alloy. *The Journal of Physical Chemistry Letters*, 7(6):1083–1087, 2016.

[16] Edward J Brook. Tiny bubbles tell all. *Science*, 310(5752):1285–1287, 2005.

[17] Daniel Bryant, Nicholas Aristidou, Sebastian Pont, Irene Sanchez-Molina, Thana Chotchunangatchaval, Scot Wheeler, James R Durrant, and Saif A Haque. Light and oxygen induced degradation limits the operational stability of methylammonium lead triiodide perovskite solar cells. *Energy & Environmental Science*, 9(5):1655–1660, 2016.

[18] Tongle Bu, Lan Wu, Xueping Liu, Xiaokun Yang, Peng Zhou, Xinxin Yu, Tianshi Qin, Jiangjian Shi, Song Wang, Saisai Li, et al. Synergic interface optimization with green solvent engineering in mixed perovskite solar cells. *Advanced Energy Materials*, 7(20):1700576, 2017.

[19] Xiangnan Bu, Robert JE Westbrook, Luis Lanzetta, Dong Ding, Thana Chotchuangchutchaval, Nicholas Aristidou, and Saif A Haque. Surface passivation of perovskite films via iodide salt coatings for enhanced stability of organic lead halide perovskite solar cells. *Solar RRL*, 3(2):1800282, 2019.

[20] A Cabana and C Sandorfy. The infrared spectra of solid methylammonium halides. *Spectrochimica Acta*, 18(6):843–861, 1962.

[21] Frankfurt School-UNEP Centre/BNEF. Global trends in renewable energy investment 2020. Technical report, Frankfurt School-UNEP Centre/BNEF, Frankfurt, 2020.

[22] Chih-Chung Chang and Chih-Jen Lin. LIBSVM: a library for support vector machines. *ACM Transactions on Intelligent Systems and Technology (TIST)*, 2(3):1–27, 2011.

[23] Nathan L Chang, Anita Wing Yi Ho-Baillie, Paul A Basore, Trevor L Young, Rhett Evans, and Renate J Egan. A manufacturing cost estimation method with uncertainty analysis and its application to perovskite on glass photovoltaic modules. *Progress in Photovoltaics: Research and Applications*, 25(5):390–405, 2017.

[24] Peng Chen, Yang Bai, Songcan Wang, Miaoqiang Lyu, Jung-Ho Yun, and Lianzhou Wang. In situ growth of 2D perovskite capping layer for stable and efficient perovskite solar cells. *Advanced Functional Materials*, 28(17):1706923, 2018.

[25] Yani Chen, Yong Sun, Jiajun Peng, Junhui Tang, Kaibo Zheng, and Ziqi Liang. 2D Ruddlesden-Popper perovskites for optoelectronics. *Advanced Materials*, 30(2):1703487, Jan 2018.

[26] Kyung Taek Cho, Yi Zhang, Simonetta Orlandi, Marco Cavazzini, Iwan Zimmermann, Andreas Lesch, Nouar Tabet, Gianluca Pozzi, Giulia Grancini, and Mohammad Khaja Nazeeruddin. Water-repellent low-dimensional fluorous perovskite as interfacial coating for 20% efficient solar cells. *Nano Letters*, 18(9):5467–5474, 2018.

[27] Juan-Pablo Correa-Baena, Miguel Anaya, Gabriel Lozano, Wolfgang Tress, Konrad Domanski, Michael Saliba, Taisuke Matsui, Tor Jesper Jacobsson, Mauricio E Calvo, Antonio Abate, et al. Unbroken perovskite: Interplay of morphology, electro-optical properties, and ionic movement. *Advanced Materials*, 28(25):5031–5037, 2016.

[28] Peter M Cox, Richard A Betts, Chris D Jones, Steven A Spall, and Ian J Totterdell. Acceleration of global warming due to carbon-cycle feedbacks in a coupled climate model. *Nature*, 408(6809):184–187, 2000.

[29] Felix Creutzig, Peter Agoston, Jan Christoph Goldschmidt, Gunnar Luderer, Gregory Nemet, and Robert C Pietzcker. The underestimated potential of solar energy to mitigate climate change. *Nature Energy*, 2(9):17140, 2017.

[30] M DeCastro, M Gómez-Gesteira, I Alvarez, and JLG Gesteira. Present warming within the context of cooling–warming cycles observed since 1854 in the Bay of Biscay. *Continental Shelf Research*, 29(8):1053–1059, 2009.

[31] Ayon Dey. Machine learning algorithms: A review. *International Journal of Computer Science and Information Technologies*, 7(3):1174–1179, 2016.

[32] Hua Dong, Jun Xi, Lijian Zuo, Jingrui Li, Yingguo Yang, Dongdong Wang, Yue Yu, Lin Ma, Chenxin Ran, Weiyin Gao, et al. Conjugated molecules "bridge": Functional ligand toward highly efficient and long-term stable perovskite solar cell. *Advanced Functional Materials*, 29(17):1808119, 2019.

[33] Sergiu Draguta, Onise Sharia, Seog Joon Yoon, Michael C Brennan, Yurii V Morozov, Joseph S Manser, Prashant V Kamat, William F Schneider, and Masaru Kuno. Rationalizing the light-induced phase separation of mixed halide organic–inorganic perovskites. *Nature Communications*, 8(1):1–8, 2017.

[34] Hong-Hua Fang, Jie Yang, Shuxia Tao, Sampson Adjokatse, Machteld E Kamminga, Jianting Ye, Graeme R Blake, Jacky Even, and Maria Antonietta Loi. Unravelling light-induced degradation of layered perovskite crystals and design of efficient encapsulation for improved photostability. *Advanced Functional Materials*, 28(21):1800305, 2018.

[35] Xiaoxia Feng, Ruihao Chen, Zi-Ang Nan, Xudong Lv, Ruiqian Meng, Jing Cao, and Yu Tang. Perfection of perovskite grain boundary passivation by euporphyrin complex for overall-stable perovskite solar cells. *Advanced Science*, 6(5):1802040, 2019.

[36] Peter I Frazier and Jialei Wang. Bayesian optimization for materials design. In *Information Science for Materials Discovery and Design*, pages 45–75. Springer, 2016.

[37] Pierre Friedlingstein, Matthew W Jones, Michael O'sullivan, Robbie M Andrew, Judith Hauck, Glen P Peters, Wouter Peters, Julia Pongratz, Stephen Sitch, Corinne Le Quéré, et al. Global carbon budget 2019. *Earth System Science Data*, 11(4):1783–1838, 2019.

[38] Jerome H Friedman. Greedy function approximation: A gradient boosting machine. *Annals of Statistics*, pages 1189–1232, 2001.

[39] Qingxia Fu, Shuqin Xiao, Xianglan Tang, Yiwang Chen, and Ting Hu. Amphiphilic fullerenes employed to improve the quality of perovskite films and the stability of perovskite solar cells. *ACS Applied Materials & Interfaces*, 11(27):24782–24788, 2019.

[40] Alex M Ganose, Christopher N Savory, and David O Scanlon. Beyond methylammonium lead iodide: prospects for the emergent field of ns^2 containing solar absorbers. *Chemical Communications*, 53(1):20–44, 2017.

[41] Peng Gao, Abd Rashid Bin Mohd Yusoff, and Mohammad Khaja Nazeeruddin. Dimensionality engineering of hybrid halide perovskite light absorbers. *Nature Communications*, 9(1):5028, Dec 2018.

[42] Saba Gharibzadeh, Bahram Abdollahi Nejand, Marius Jakoby, Tobias Abzieher, Dirk Hauschild, Somayeh Moghadamzadeh, Jonas A Schwenzer, Philipp Brenner, Raphael Schmager, Amir Abbas Haghighirad, et al. Record open-circuit voltage wide-bandgap perovskite solar cells utilizing 2D/3D perovskite heterostructure. *Advanced Energy Materials*, 9(21):1803699, 2019.

[43] G. Grancini, C. Roldán-Carmona, I. Zimmermann, E. Mosconi, X. Lee, D. Martineau, S. Narbey, F. Oswald, F. De Angelis, M. Graetzel, and Mohammad Khaja Nazeeruddin. One-Year stable perovskite solar cells by 2D/3D interface engineering. *Nature Communications*, 8:15684, Jun 2017.

[44] Giulia Grancini and Mohammad Khaja Nazeeruddin. Dimensional tailoring of hybrid perovskites for photovoltaics. *Nature Reviews Materials*, 4(1):4–22, Jan 2019.

[45] Pesi Mwitumwa Hangoma, Insoo Shin, Hyun-Seock Yang, Danbi Kim, Yun Kyung Jung, Bo Ram Lee, Joo Hyun Kim, Kwang Ho Kim, and Sung Heum Park. 2D perovskite seeding layer for efficient air-processable and stable planar perovskite solar cells. *Advanced Functional Materials*, 30(34):2003081, 2020.

[46] Noor Titan Putri Hartono. Interplay of optoelectronic properties and solar cell performance in multidimensional perovskites. Master's thesis, Massachusetts Institute of Technology, 2018.

[47] Noor Titan Putri Hartono, Shijing Sun, María C. Gélvez-Rueda, Polly J Pierone, Matthew P. Erodici, Jason Yoo, Fengxia Wei, Moungi Bawendi, Ferdinand C. Grozema, Meng Ju Sher, Tonio Buonassisi, and Juan Pablo Correa-Baena. The effect of structural dimensionality on carrier mobility in lead-halide perovskites. *Journal of Materials Chemistry A*, 7(41):23949–23957, 2019.

[48] Noor Titan Putri Hartono, Janak Thapa, Armi Tiihonen, Felipe Oviedo, Clio Batali, Jason J. Yoo, Zhe Liu, Ruipeng Li, David Fuertes Marrón, Moungi G. Bawendi, Tonio Buonassisi, and Shijing Sun. How machine learning can help select capping layers to suppress perovskite degradation. *Nature Communications*, 11(1):1–9, 2020.

[49] Kate Higgins, Sai Mani Valleti, Maxim Ziatdinov, Sergei Kalinin, and Mahshid Ahmadi. Chemical robotics enabled exploration of stability and photoluminescent behavior in multicomponent hybrid perovskites via machine learning. *ChemRxiv*, 2020.

[50] Tin Kam Ho. The random subspace method for constructing decision forests. *IEEE Transactions on Pattern Analysis and Machine Intelligence*, 20(8):832–844, 1998.

[51] Eric T Hoke, Daniel J Slotcavage, Emma R Dohner, Andrea R Bowring, Hemamala I Karunadasa, and Michael D McGehee. Reversible photo-induced trap

formation in mixed-halide hybrid perovskites for photovoltaics. *Chemical Science*, 6(1):613–617, 2015.

[52] John M Howard, Elizabeth M Tennyson, Bernardo RA Neves, and Marina S Leite. Machine learning for perovskites' reap-rest-recovery cycle. *Joule*, 3(2):325–337, 2019.

[53] Junjie Hu, Chenxi Wang, Qianhong Li, Rongjian Sa, and Peng Gao. Accelerated design of photovoltaic Ruddlesden–Popper perovskite $Ca_6Sn_4S_{14-x}O_x$ using machine learning. *APL Materials*, 8(11):111109, 2020.

[54] Miao Hu, Cheng Bi, Yongbo Yuan, Yang Bai, and Jinsong Huang. Stabilized wide bandgap $MAPbBr_xI_{3-x}$ perovskite by enhanced grain size and improved crystallinity. *Advanced Science*, 3(6):1500301, 2016.

[55] Yanqiang Hu, Ting Qiu, Fan Bai, Wei Ruan, and Shufang Zhang. Highly efficient and stable solar cells with 2D $MA_3Bi_2I_9$/3D $MAPbI_3$ heterostructured perovskites. *Advanced Energy Materials*, 8(19):1703620, 2018.

[56] Xin Huang, Qiuhong Cui, Wentao Bi, Ling Li, Pengcheng Jia, Yanbing Hou, Yufeng Hu, Zhidong Lou, and Feng Teng. Two-dimensional additive diethylammonium iodide promoting crystal growth for efficient and stable perovskite solar cells. *RSC Advances*, 9(14):7984–7991, 2019.

[57] Lior Iagher and Lioz Etgar. Effect of cs on the stability and photovoltaic performance of 2D/3D perovskite-based solar cells. *ACS Energy Letters*, 3(2):366–372, 2018.

[58] Jino Im, Seongwon Lee, Tae-Wook Ko, Hyun Woo Kim, YunKyong Hyon, and Hyunju Chang. Identifying Pb-free perovskites for solar cells by machine learning. *npj Computational Materials*, 5(1):1–8, 2019.

[59] Min Ju Jeong, Kyung Mun Yeom, Se Jin Kim, Eui Hyuk Jung, and Jun Hong Noh. Spontaneous interface engineering for dopant-free poly (3-hexylthiophene) perovskite solar cells with efficiency over 24%. *Energy & Environmental Science*, 2021.

[60] Eui Hyuk Jung, Nam Joong Jeon, Eun Young Park, Chan Su Moon, Tae Joo Shin, Tae-Youl Yang, Jun Hong Noh, and Jangwon Seo. Efficient, stable and scalable perovskite solar cells using poly (3-hexylthiophene). *Nature*, 567(7749):511–515, 2019.

[61] Ryo Kanada, Atsushi Tokuhisa, Koji Tsuda, Yasushi Okuno, and Kei Terayama. Exploring successful parameter region for coarse-grained simulation of biomolecules by Bayesian optimization and active learning. *Biomolecules*, 10(3):482, 2020.

[62] Sunghwan Kim, Jie Chen, Tiejun Cheng, Asta Gindulyte, Jia He, Siqian He, Qingliang Li, Benjamin A Shoemaker, Paul A Thiessen, Bo Yu, et al. PubChem 2019 update: Improved access to chemical data. *Nucleic Acids Research*, 47(D1):D1102–D1109, 2019.

[63] DP Kingman and J Ba. Adam: A method for stochastic optimization. conference paper. In *3rd International Conference for Learning Representations*, 2015.

[64] Jeffrey Kirman, Andrew Johnston, Douglas A Kuntz, Mikhail Askerka, Yuan Gao, Petar Todorović, Dongxin Ma, Gilbert G Privé, and Edward H Sargent. Machine-learning-accelerated perovskite crystallization. *Matter*, 2020.

[65] Alexander J Knight, Adam D Wright, Jay B Patel, David P McMeekin, Henry J Snaith, Michael B Johnston, and Laura M Herz. Electronic traps and phase segregation in lead mixed-halide perovskite. *ACS Energy Letters*, 4(1):75–84, 2018.

[66] Liang Kuai, Junnan Li, Yajuan Li, Yusheng Wang, Pandeng Li, Yuanshuai Qin, Tao Song, Yingguo Yang, Zhuoying Chen, Xingyu Gao, et al. Revealing crystallization dynamics and the compositional control mechanism of 2D perovskite film growth by in situ synchrotron-based gixrd. *ACS Energy Letters*, 5(1):8–16, 2019.

[67] Maria-Grazia La-Placa, Lidon Gil-Escrig, Dengyang Guo, Francisco Palazon, Tom J Savenije, Michele Sessolo, and Henk J Bolink. Vacuum-deposited 2D/3D perovskite heterojunctions. *ACS Energy Letters*, 4(12):2893–2901, 2019.

[68] National Renewable Energy Lab. Best research-cell efficiency chart, Sep 2020.

[69] Alfirna Rizqi Lahitani, Adhistya Erna Permanasari, and Noor Akhmad Setiawan. Cosine similarity to determine similarity measure: Study case in online essay assessment. In *2016 4th International Conference on Cyber and IT Service Management*, pages 1–6. IEEE, 2016.

[70] Niraj N Lal, Yasmina Dkhissi, Wei Li, Qicheng Hou, Yi-Bing Cheng, and Udo Bach. Perovskite tandem solar cells. *Advanced Energy Materials*, 7(18):1602761, 2017.

[71] Baoli Li and Liping Han. Distance weighted cosine similarity measure for text classification. In *International Conference on Intelligent Data Engineering and Automated Learning*, pages 611–618. Springer, 2013.

[72] Jiangwei Li, Qingshun Dong, Nan Li, and Liduo Wang. Direct evidence of ion diffusion for the silver-electrode-induced thermal degradation of inverted perovskite solar cells. *Advanced Energy Materials*, 7(14):1602922, 2017.

[73] Pengwei Li, Yiqiang Zhang, Chao Liang, Guichuan Xing, Xiaolong Liu, Fengyu Li, Xiaotao Liu, Xiaotian Hu, Guosheng Shao, and Yanlin Song. Phase pure 2D perovskite for high-performance 2D-3D heterostructured perovskite solar cells. *Advanced Materials*, 30(52):1805323, 2018.

[74] Wei Li, Ryan Jacobs, and Dane Morgan. Predicting the thermodynamic stability of perovskite oxides using machine learning models. *Computational Materials Science*, 150:454–463, 2018.

[75] Wenzhe Li, Jiandong Fan, Jiangwei Li, Yaohua Mai, and Liduo Wang. Controllable grain morphology of perovskite absorber film by molecular self-assembly toward efficient solar cell exceeding 17%. *Journal of the American Chemical Society*, 137(32):10399–10405, 2015.

[76] Zhenzhen Li, Xiaolong Liu, Jia Xu, Shujie Yang, Hang Zhao, Hui Huang, Shengzhong Liu, and Jianxi Yao. 2D-3D $Cs_2PbI_2Cl_2-CsPbI_{2.5}Br_{0.5}$ mixed-dimensional films for all-inorganic perovskite solar cells with enhanced efficiency and stability. *The Journal of Physical Chemistry Letters*, 2020.

[77] Rebecca Lindsey. Climate change: Global sea level | noaa climate.gov. https://www.climate.gov/news-features/understanding-climate/climate-change-global-sea-level, August 2020. (Accessed on 01/06/2021).

[78] Fangzhou Liu, Qi Dong, Man Kwong Wong, Aleksandra B Djurišić, Annie Ng, Zhiwei Ren, Qian Shen, Charles Surya, Wai Kin Chan, Jian Wang, et al. Is excess PbI_2 beneficial for perovskite solar cell performance? *Advanced Energy Materials*, 6(7):1502206, 2016.

[79] Shuaihua Lu, Qionghua Zhou, Yixin Ouyang, Yilv Guo, Qiang Li, and Jinlan Wang. Accelerated discovery of stable lead-free hybrid organic-inorganic perovskites via machine learning. *Nature Communications*, 9(1):1–8, 2018.

[80] Scott M Lundberg and Su-In Lee. A unified approach to interpreting model predictions. In *Advances in Neural Information Processing Systems*, pages 4765–4774, 2017.

[81] Wei Luo, Cuncun Wu, Duo Wang, Yuqing Zhang, Zehao Zhang, Xin Qi, Ning Zhu, Xuan Guo, Bo Qu, Lixin Xiao, et al. Efficient and stable perovskite solar cell with high open-circuit voltage by dimensional interface modification. *ACS Applied Materials & Interfaces*, 11(9):9149–9155, 2019.

[82] Yanqi Luo, Parisa Khoram, Sarah Brittman, Zhuoying Zhu, Barry Lai, Shyue Ping Ong, Erik C Garnett, and David P Fenning. Direct observation of halide migration and its effect on the photoluminescence of methylammonium lead bromide perovskite single crystals. *Advanced Materials*, 29(43):1703451, 2017.

[83] Chaoyan Ma, Chongqian Leng, Yixiong Ji, Xingzhan Wei, Kuan Sun, Linlong Tang, Jun Yang, Wei Luo, Chaolong Li, Yunsheng Deng, et al. 2D/3D perovskite hybrids as moisture-tolerant and efficient light absorbers for solar cells. *Nanoscale*, 8(43):18309–18314, 2016.

[84] Sawanta S Mali and Chang Kook Hong. p–i–n/n–i–p type planar hybrid structure of highly efficient perovskite solar cells towards improved air stability: Synthetic strategies and the role of p-type hole transport layer (htl) and n-type electron transport layer (etl) metal oxides. *Nanoscale*, 8(20):10528–10540, 2016.

[85] Ian Mathews, Sai Nithin Reddy Kantareddy, Shijing Sun, Mariya Layurova, Janak Thapa, Juan-Pablo Correa-Baena, Rahul Bhattacharyya, Tonio Buonassisi, Sanjay Sarma, and Ian Marius Peters. Self-powered sensors enabled by wide-bandgap perovskite indoor photovoltaic cells. *Advanced Functional Materials*, 29(42):1904072, 2019.

[86] Paolo Menesatti, Claudio Angelini, Federico Pallottino, Francesca Antonucci, Jacopo Aguzzi, and Corrado Costa. RGB color calibration for quantitative image analysis: The "3D Thin-Plate Spline" warping approach. *Sensors*, 12(6):7063–7079, 2012.

[87] Edoardo Mosconi, Anna Amat, Md K Nazeeruddin, Michael Grätzel, and Filippo De Angelis. First-principles modeling of mixed halide organometal perovskites for photovoltaic applications. *The Journal of Physical Chemistry C*, 117(27):13902–13913, 2013.

[88] Edoardo Mosconi, Jon M Azpiroz, and Filippo De Angelis. Ab initio molecular dynamics simulations of methylammonium lead iodide perovskite degradation by water. *Chemistry of Materials*, 27(13):4885–4892, 2015.

[89] Christian Müller, Tobias Glaser, Marcel Plogmeyer, Michael Sendner, Sebastian Döring, Artem A Bakulin, Carlo Brzuska, Roland Scheer, Maxim S Pshenichnikov, Wolfgang Kowalsky, Annemarie Pucci, and Robert Lovrinčić. Water infiltration in methylammonium lead iodide perovskite: Fast and inconspicuous. *Chemistry of Materials*, 27(22):7835–7841, 2015.

[90] Gregory F Nemet, Eric O'Shaughnessy, Ryan Wiser, Naïm Darghouth, Galen Barbose, Ken Gillingham, and Varun Rai. Characteristics of low-priced solar PV systems in the us. *Applied Energy*, 187:501–513, 2017.

[91] Hieu V Nguyen and Li Bai. Cosine similarity metric learning for face verification. In *Asian Conference on Computer Vision*, pages 709–720. Springer, 2010.

[92] Wendy J Nimens, Sarah J Lefave, Laura Flannery, Jonathan Ogle, Detlef-M Smilgies, Matthew T Kieber-Emmons, and Luisa Whittaker-Brooks. Understanding hydrogen bonding interactions in crosslinked methylammonium lead iodide crystals: Towards reducing moisture and light degradation pathways. *Angewandte Chemie International Edition*, 58(39):13912–13921, 2019.

[93] Guangda Niu, Xudong Guo, and Liduo Wang. Review of recent progress in chemical stability of perovskite solar cells. *Journal of Materials Chemistry A*, 3(17):8970–8980, Apr 2015.

[94] Tianqi Niu, Jing Lu, Xuguang Jia, Zhuo Xu, Ming-Chun Tang, Dounya Barrit, Ningyi Yuan, Jianning Ding, Xu Zhang, Yuanyuan Fan, et al. Interfacial engineering at the 2D/3D heterojunction for high-performance perovskite solar cells. *Nano Letters*, 19(10):7181–7190, 2019.

[95] Khuong P Ong, Teck Wee Goh, Qiang Xu, and Alfred Huan. Structural evolution in methylammonium lead iodide $CH_3NH_3PbI_3$. *The Journal of Physical Chemistry A*, 119(44):11033–11038, 2015.

[96] Yixin Ouyang, Yajuan Li, Pengchen Zhu, Qiang Li, Yuan Gao, Jianyu Tong, Li Shi, Qionghua Zhou, Chongyi Ling, Qian Chen, et al. Photo-oxidative degradation of methylammonium lead iodide perovskite: mechanism and protection. *Journal of Materials Chemistry A*, 7(5):2275–2282, 2019.

[97] Felipe Oviedo, Zekun Ren, Shijing Sun, Charles Settens, Zhe Liu, Noor Titan Putri Hartono, Savitha Ramasamy, Brian L DeCost, Siyu IP Tian, Giuseppe Romano, et al. Fast and interpretable classification of small X-ray diffraction datasets using data augmentation and deep neural networks. *npj Computational Materials*, 5(1):1–9, 2019.

[98] B Palosz. The structure of PbI_2 polytypes 2H and 4H: A study of the 2H-4H transition. *Journal of Physics: Condensed Matter*, 2(24):5285, 1990.

[99] Heesoo Park, Raghvendra Mall, Fahhad H Alharbi, Stefano Sanvito, Nouar Tabet, Halima Bensmail, and Fedwa El-Mellouhi. Exploring new approaches towards the formability of mixed-ion perovskites by dft and machine learning. *Physical Chemistry Chemical Physics*, 21(3):1078–1088, 2019.

[100] Nam-Gyu Park. Perovskite solar cells: An emerging photovoltaic technology. *Materials Today*, 18(2):65–72, 2015.

[101] Fabian Pedregosa, Gaël Varoquaux, Alexandre Gramfort, Vincent Michel, Bertrand Thirion, Olivier Grisel, Mathieu Blondel, Peter Prettenhofer, Ron Weiss, Vincent Dubourg, et al. Scikit-learn: Machine learning in Python. *the Journal of Machine Learning Research*, 12:2825–2830, 2011.

[102] Chao Peng, Jianfu Chen, Haifeng Wang, and P Hu. First-principles insight into the degradation mechanism of $CH_3NH_3PbI_3$ perovskite: Light-induced defect formation and water dissociation. *The Journal of Physical Chemistry C*, 122(48):27340–27349, 2018.

[103] Jean-Robert Petit, Jean Jouzel, Dominique Raynaud, Narcisse I Barkov, J-M Barnola, Isabelle Basile, Michael Bender, Jérôme Chappellaz, M Davis, Gilles Delaygue, et al. Climate and atmospheric history of the past 420,000 years from the Vostok ice core, Antarctica. *Nature*, 399(6735):429–436, 1999.

[104] Ghanshyam Pilania, Prasanna V Balachandran, Chiho Kim, and Turab Lookman. Finding new perovskite halides via machine learning. *Frontiers in Materials*, 3:19, 2016.

[105] Ghanshyam Pilania, Arun Mannodi-Kanakkithodi, BP Uberuaga, Rampi Ramprasad, JE Gubernatis, and Turab Lookman. Machine learning bandgaps of double perovskites. *Scientific Reports*, 6:19375, 2016.

[106] Adam Podlaha, Michal Lörinc, Gaurav Srivastava, Steve Bowen, and Brian Kerschner. Weather, climate & catastrophe insight - 2020 annual report. Technical report, Aon, 2021.

[107] Jeremy R Poindexter, Robert LZ Hoye, Lea Nienhaus, Rachel C Kurchin, Ashley E Morishige, Erin E Looney, Anna Osherov, Juan-Pablo Correa-Baena, Barry Lai, Vladimir Bulović, et al. High tolerance to iron contamination in lead halide perovskite solar cells. *ACS Nano*, 11(7):7101–7109, 2017.

[108] VS Prasatha, Haneen Arafat Abu Alfeilate, AB Hassanate, Omar Lasassmehe, Ahmad S Tarawnehf, Mahmoud Bashir Alhasanatg, and Hamzeh S Eyal Salmane. Effects of distance measure choice on knn classifier performance-a review. *arXiv preprint arXiv:1708.04321*, 2017.

[109] Longbin Qiu, Sisi He, Luis K Ono, Shengzhong Liu, and Yabing Qi. Scalable fabrication of metal halide perovskite solar cells and modules. *ACS Energy Letters*, 4(9):2147–2167, 2019.

[110] Nicholas Rolston, William J Scheideler, Austin C Flick, Justin P Chen, Hannah Elmaraghi, Andrew Sleugh, Oliver Zhao, Michael Woodhouse, and Reinhold H Dauskardt. Rapid open-air fabrication of perovskite solar modules. *Joule*, 4(12):2675–2692, 2020.

[111] Anthony Ruth, Michael C Brennan, Sergiu Draguta, Yurii V Morozov, Maksym Zhukovskyi, Boldizsar Janko, Peter Zapol, and Masaru Kuno. Vacancy-mediated anion photosegregation kinetics in mixed halide hybrid perovskites: coupled kinetic Monte Carlo and optical measurements. *ACS Energy Letters*, 3(10):2321–2328, 2018.

[112] Wissam A Saidi, Waseem Shadid, and Ivano E Castelli. Machine-learning structural and electronic properties of metal halide perovskites using a hierarchical convolutional neural network. *npj Computational Materials*, 6(1):1–7, 2020.

[113] Michael Saliba, Juan Pablo Correa-Baena, Christian M. Wolff, Martin Stolterfoht, Nga Phung, Steve Albrecht, Dieter Neher, and Antonio Abate. How to Make over 20% Efficient Perovskite Solar Cells in Regular (n–i–p) and Inverted (p–i–n) Architectures. *Chemistry of Materials*, 30(13):4193–4201, Jul 2018.

[114] Johannes Schlipf, Yinghong Hu, Shambhavi Pratap, Lorenz Bießmann, Nuri Hohn, Lionel Porcar, Thomas Bein, Pablo Docampo, and Peter Mülller-Buschbaum. Shedding light on the moisture stability of 3D/2D hybrid perovskite heterojunction thin films. *ACS Applied Energy Materials*, 2(2):1011–1018, 2019.

[115] Seong Sik Shin, Juan Pablo Correa Baena, Rachel C Kurchin, Alex Polizzotti, Jason Jungwan Yoo, Sarah Wieghold, Moungi G Bawendi, and Tonio Buonassisi. Solvent-engineering method to deposit compact bismuth-based thin films: Mechanism and application to photovoltaics. *Chemistry of Materials*, 30(2):336–343, 2018.

[116] Masaki Shirayama, Masato Kato, Tetsuhiko Miyadera, Takeshi Sugita, Takemasa Fujiseki, Shota Hara, Hideyuki Kadowaki, Daisuke Murata, Masayuki Chikamatsu, and Hiroyuki Fujiwara. Degradation mechanism of $CH_3NH_3PbI_3$ perovskite materials upon exposure to humid air. *Journal of Applied Physics*, 119(11):115501, 2016.

[117] Amanpreet Singh, Narina Thakur, and Aakanksha Sharma. A review of supervised machine learning algorithms. In *2016 3rd International Conference on Computing for Sustainable Global Development (INDIACom)*, pages 1310–1315. Ieee, 2016.

[118] Ganesh Sivaraman, Anand Narayanan Krishnamoorthy, Matthias Baur, Christian Holm, Marius Stan, Gábor Csányi, Chris Benmore, and Álvaro Vázquez-Mayagoitia. Machine-learned interatomic potentials by active learning: amorphous and liquid hafnium dioxide. *npj Computational Materials*, 6(1):1–8, 2020.

[119] Emanuele Smecca, Youhei Numata, Ioannis Deretzis, Giovanna Pellegrino, Simona Boninelli, Tsutomu Miyasaka, Antonino La Magna, and Alessandra Alberti. Stability of solution-processed $MAPbI_3$ and $FAPbI_3$ layers. *Physical Chemistry Chemical Physics*, 18(19):13413–13422, 2016.

[120] Ian C. Smith, Eric T. Hoke, Diego Solis-Ibarra, Michael D. McGehee, and Hemamala I. Karunadasa. A Layered Hybrid Perovskite Solar-Cell Absorber with Enhanced Moisture Stability. *Angewandte Chemie International Edition*, 53(42):11232–11235, Oct 2014.

[121] Ian C Smith, Eric T Hoke, Diego Solis-Ibarra, Michael D McGehee, and Hemamala I Karunadasa. A layered hybrid perovskite solar-cell absorber with enhanced moisture stability. *Angewandte Chemie*, 126(42):11414–11417, 2014.

[122] Chan Myae Myae Soe, Wanyi Nie, Constantinos C Stoumpos, Hsinhan Tsai, Jean-Christophe Blancon, Fangze Liu, Jacky Even, Tobin J Marks, Aditya D Mohite, and Mercouri G Kanatzidis. Understanding film formation morphology and orientation in high member 2D Ruddlesden–Popper perovskites for high-efficiency solar cells. *Advanced Energy Materials*, 8(1):1700979, 2018.

[123] Zhaoning Song, Chad L McElvany, Adam B Phillips, Ilke Celik, Patrick W Krantz, Suneth C Watthage, Geethika K Liyanage, Defne Apul, and Michael J Heben. A technoeconomic analysis of perovskite solar module manufacturing with low-cost materials and techniques. *Energy & Environmental Science*, 10(6):1297–1305, 2017.

[124] Zhaoning Song, Niraj Shrestha, Suneth C Watthage, Geethika K Liyanage, Zahrah S Almutawah, Ramez H Ahangharnejhad, Adam B Phillips, Randy J Ellingson, and Michael J Heben. Impact of moisture on photoexcited charge carrier dynamics in methylammonium lead halide perovskites. *The Journal of Physical Chemistry Letters*, 9(21):6312–6320, 2018.

[125] Jared C Stanley, Felix Mayr, and Alessio Gagliardi. Machine learning stability and bandgaps of lead-free perovskites for photovoltaics. *Advanced Theory and Simulations*, 3(1):1900178, 2020.

[126] Teague Sterling and John J Irwin. ZINC 15–ligand discovery for everyone. *Journal of Chemical Information and Modeling*, 55(11):2324–2337, 2015.

[127] Constantinos C. Stoumpos, Duyen H. Cao, Daniel J. Clark, Joshua Young, James M. Rondinelli, Joon I. Jang, Joseph T. Hupp, and Mercouri G. Kanatzidis. Ruddlesden–Popper Hybrid Lead Iodide Perovskite 2D Homologous Semiconductors. *Chemistry of Materials*, 28(8):2852–2867, Apr 2016.

[128] Constantinos C Stoumpos, Christos D Malliakas, and Mercouri G Kanatzidis. Semiconducting tin and lead iodide perovskites with organic cations: Phase transitions, high mobilities, and near-infrared photoluminescent properties. *Inorganic Chemistry*, 52(15):9019–9038, 2013.

[129] Qing Sun, Paul Fassl, David Becker-Koch, Alexandra Bausch, Boris Rivkin, Sai Bai, Paul E Hopkinson, Henry J Snaith, and Yana Vaynzof. Role of microstructure in oxygen induced photodegradation of methylammonium lead triiodide perovskite films. *Advanced Energy Materials*, 7(20):1700977, 2017.

[130] Shijing Sun, Noor TP Hartono, Zekun D Ren, Felipe Oviedo, Antonio M Buscemi, Mariya Layurova, De Xin Chen, Tofunmi Ogunfunmi, Janak Thapa, Savitha Ramasamy, et al. Accelerated development of perovskite-inspired materials via high-throughput synthesis and machine-learning diagnosis. *Joule*, 3(6):1437–1451, 2019.

[131] Shijing Sun, Armi Tiihonen, Felipe Oviedo, Zhe Liu, Janak Thapa, Yicheng Zhao, Noor Titan P Hartono, Anuj Goyal, Thomas Heumueller, Clio Batali, et al. A data fusion approach to optimize compositional stability of halide perovskites. *Matter*, 2021.

[132] Xiaofeng Tang, Marco Brandl, Benjamin May, Ievgen Levchuk, Yi Hou, Moses Richter, Haiwei Chen, Shi Chen, Simon Kahmann, Andres Osvet, et al. Photoinduced degradation of methylammonium lead triiodide perovskite semiconductors. *Journal of Materials Chemistry A*, 4(41):15896–15903, 2016.

[133] J Tauc and A Menth. States in the gap. *Journal of Non-Crystalline Solids*, 8:569–585, 1972.

[134] Sam Teale, Andrew H Proppe, Eui Hyuk Jung, Andrew Johnston, Darshan H Parmar, Bin Chen, Yi Hou, Shana O Kelley, and Edward H Sargent. Dimensional mixing increases the efficiency of 2D/3D perovskite solar cells. *The Journal of Physical Chemistry Letters*, 11(13):5115–5119, 2020.

[135] Armi Tiihonen, Kati Miettunen, Janne Halme, Sakari Lepikko, Aapo Poskela, and Peter D Lund. Critical analysis on the quality of stability studies of perovskite and dye solar cells. *Energy & Environmental Science*, 11(4):730–738, 2018.

[136] Armi Tiihonen, Felipe Oviedo, Shreyaa Raghavan, and Zhe Liu. SPProC: Sequential learning with physical probabilistic constraints. `https://github.com/PV-Lab/SPProC`, 2020.

[137] Vahe Tshitoyan, John Dagdelen, Leigh Weston, Alexander Dunn, Ziqin Rong, Olga Kononova, Kristin A Persson, Gerbrand Ceder, and Anubhav Jain. Unsupervised word embeddings capture latent knowledge from materials science literature. *Nature*, 571(7763):95–98, 2019.

[138] Ganbaatar Tumen-Ulzii, Chuanjiang Qin, Dino Klotz, Matthew R Leyden, Pangpang Wang, Morgan Auffray, Takashi Fujihara, Toshinori Matsushima, Jin-Wook Lee, Sung-Joon Lee, et al. Detrimental effect of unreacted PbI_2 on the long-term stability of perovskite solar cells. *Advanced Materials*, 32(16):1905035, 2020.

[139] UNFCCC. The paris agreement | unfccc. `https://unfccc.int/process-and-meetings/the-paris-agreement/the-paris-agreement`. (Accessed on 01/06/2021).

[140] Yana Vaynzof. The future of perovskite photovoltaics—thermal evaporation or solution processing? *Advanced Energy Materials*, 10(48):2003073, 2020.

[141] Rui Wang, Jingjing Xue, Lei Meng, Jin-Wook Lee, Zipeng Zhao, Pengyu Sun, Le Cai, Tianyi Huang, Zhengxu Wang, Zhao-Kui Wang, et al. Caffeine improves the performance and thermal stability of perovskite solar cells. *Joule*, 3(6):1464–1477, 2019.

[142] Xi Wang, Yichuan Ling, Xiujun Lian, Yan Xin, Kamal B Dhungana, Fernando Perez-Orive, Javon Knox, Zhizhong Chen, Yan Zhou, Drake Beery, et al. Suppressed phase separation of mixed-halide perovskites confined in endotaxial matrices. *Nature communications*, 10(1):1–7, 2019.

[143] Zhiping Wang, Qianqian Lin, Francis P. Chmiel, Nobuya Sakai, Laura M. Herz, and Henry J. Snaith. Efficient ambient-air-stable solar cells with 2D–3D heterostructured butylammonium-caesium-formamidinium lead halide perovskites. *Nature Energy*, 2(9):17135, Aug 2017.

[144] Bryan R Wygant, Alexandre Z Ye, Andrei Dolocan, Quyen Vu, David M Abbot, and C Buddie Mullins. Probing the degradation chemistry and enhanced stability of 2D organolead halide perovskites. *Journal of the American Chemical Society*, 141(45):18170–18181, 2019.

[145] Peipei Xia, Li Zhang, and Fanzhang Li. Learning similarity with cosine similarity ensemble. *Information Sciences*, 307:39–52, 2015.

[146] Jixian Xu, Caleb C Boyd, J Yu Zhengshan, Axel F Palmstrom, Daniel J Witter, Bryon W Larson, Ryan M France, Jérémie Werner, Steven P Harvey, Eli J Wolf, et al. Triple-halide wide–band gap perovskites with suppressed phase segregation for efficient tandems. *Science*, 367(6482):1097–1104, 2020.

[147] Disheng Yao, Chunmei Zhang, Shengli Zhang, Yang Yang, Aijun Du, Eric Waclawik, Xiaochen Yu, Gregory J Wilson, and Hongxia Wang. 2D-3D mixed organic–inorganic perovskite layers for solar cells with enhanced efficiency and stability induced by n-propylammonium iodide additives. *ACS applied materials & interfaces*, 11(33):29753–29764, 2019.

[148] Chenyi Yi, Jingshan Luo, Simone Meloni, Ariadni Boziki, Negar Ashari-Astani, Carole Grätzel, Shaik M Zakeeruddin, Ursula Röthlisberger, and Michael Grätzel. Entropic stabilization of mixed *A*-cation ABX_3 metal halide perovskites for high performance perovskite solar cells. *Energy & Environmental Science*, 9(2):656–662, 2016.

[149] Jason J Yoo, Sarah Wieghold, Melany C Sponseller, Matthew R Chua, Sophie N Bertram, Noor Titan Putri Hartono, Jason S Tresback, Eric C Hansen, Juan-Pablo Correa-Baena, Vladimir Bulović, et al. An interface stabilized perovskite solar cell with high stabilized efficiency and low voltage loss. *Energy & Environmental Science*, 12(7):2192–2199, 2019.

[150] Seog Joon Yoon, Sergiu Draguta, Joseph S Manser, Onise Sharia, William F Schneider, Masaru Kuno, and Prashant V Kamat. Tracking iodide and bromide ion segregation in mixed halide lead perovskites during photoirradiation. *ACS Energy Letters*, 1(1):290–296, 2016.

[151] Shanshan Yu, Hongli Liu, Shirong Wang, Hongwei Zhu, Xiaofei Dong, and Xianggao Li. Hydrazinium cation mixed $FAPbI_3$-based perovskite with 1D/3D hybrid dimension structure for efficient and stable solar cells. *Chemical Engineering Journal*, page 125724, 2020.

[152] Jing Zhang, Zhelu Hu, Like Huang, Guoqiang Yue, Jinwang Liu, Xingwei Lu, Ziyang Hu, Minghui Shang, Liyuan Han, and Yuejin Zhu. Bifunctional alkyl chain barriers for efficient perovskite solar cells. *Chemical Communications*, 51(32):7047–7050, 2015.

[153] Jing Zhang, Wei Zhang, Hui-Ming Cheng, and S Ravi P Silva. Critical review of recent progress of flexible perovskite solar cells. *Materials Today*, 2020.

[154] Lei Zhang, Mu He, and Shaofeng Shao. Machine learning for halide perovskite materials. *Nano Energy*, page 105380, 2020.

[155] Tiankai Zhang, Mingzhu Long, Minchao Qin, Xinhui Lu, Si Chen, Fangyan Xie, Li Gong, Jian Chen, Ming Chu, Qian Miao, et al. Stable and efficient 3D-2D perovskite-perovskite planar heterojunction solar cell without organic hole transport layer. *Joule*, 2(12):2706–2721, 2018.

[156] Ying Zhang, Xingfeng He, Zhiqian Chen, Qiang Bai, Adelaide M Nolan, Charles A Roberts, Debasish Banerjee, Tomoya Matsunaga, Yifei Mo, and Chen Ling. Unsupervised discovery of solid-state lithium ion conductors. *Nature Communications*, 10(1):1–7, 2019.

[157] Guoqing Zhou, Weibin Chu, and Oleg V Prezhdo. Structure deformation controls charge losses in $MAPbI_3$: Unsupervised machine learning of nonadiabatic molecular dynamics. *ACS Energy Letters*, 2020.

[158] Hongwei Zhu, Yameng Ren, Linfeng Pan, Olivier Ouellette, Felix T Eickemeyer, Yinghui Wu, Xianggao Li, Shirong Wang, Hongli Liu, Xiaofei Dong, et al. Synergistic effect of fluorinated passivator and hole transport dopant enables stable perovskite solar cells with an efficiency near 24%. *Journal of the American Chemical Society*, 143(8):3231–3237, 2021.

[159] Zhuan Zhu, Viktor G Hadjiev, Yaoguang Rong, Rui Guo, Bo Cao, Zhongjia Tang, Fan Qin, Yang Li, Yanan Wang, Fang Hao, et al. Interaction of organic cation with water molecule in perovskite mapbi3: from dynamic orientational disorder to hydrogen bonding. *Chemistry of Materials*, 28(20):7385–7393, 2016.

[160] Minhua Zou, Xuefeng Xia, Yihua Jiang, Jiayi Peng, Zhenrong Jia, Xiaofeng Wang, and Fan Li. Strengthened perovskite/fullerene interface enhances efficiency and stability of inverted planar perovskite solar cells via a tetrafluoroterephthalic acid interlayer. *ACS Applied Materials & Interfaces*, 11(36):33515–33524, 2019.